

Spectral element elastic wave modelling of
Distributed Acoustic Sensing data for the
analysis of limited broadside sensitivity, in a
surface seismics configuration.

Kari-Ann Marijnissen

Master Thesis

Supervised by: Arie Verdel, Bob Paap and Hanneke Paulssen

2 May 2020

1 Summary

Distributed acoustic sensing (DAS) uses fibre optic cables to measure or monitor strain in the subsurface. With DAS being a relatively new technique it gained recently more interest for geophysical studies. The main advantages of DAS are; its high spatial resolution which is between 1-10 m, its successful use in high-temperature conditions and the low costs compared to the traditional geophones used. Eventually DAS can be used for monitoring geothermal projects and CO₂-sequestration projects (Wang et al., 2018).

With distributed acoustic sensing the strain or strain rate is measured, based on the Rayleigh scattering principle. Pulses of laser signals are sent through the fibre and the interrogator measures the back-scattered light of these pulses. The time of the laser signal and it's back-scattered component are measured and converted to strain, using the speed of light and the refractive index of the fibre (Jousset et al., 2018).

One of the challenges that DAS faces is measuring the P-waves that enter the fibre with a large angle, this is called limited broadside sensitivity. When the fibre is orientated parallel to the surface, the fibre can be insensitive to P-waves travelling vertically. Kuvshinov (2016) suggest a correction factor for this limited broadside sensitivity, which will be tested in this thesis.

With the advantages and challenges of DAS, the focus of this thesis will be on limited broad side sensitivity and the main question of this master thesis is as follows: *Can reflection information from Distributed Acoustic sensing be improved for broadside P-waves, in a surface seismics configuration?*

The approach for this new technique, is to first model DAS data with the spectral element solver SPECFEM. SPECFEM is an open-source spectral elemental modelling program, which can be used to model wave propagation (particle velocity). The aim is to translate the synthetic particle velocity data to DAS (strain) data, in order to be able to understand DAS data completely and be able to compare it to real DAS data. From the synthetic particle velocity it will be researched if broadside waves can be captured. Which is one step towards achieving synthetic DAS data.

In order to research the limited broadside sensitivity issue, the steps that need to be taken are: filtering out the surface waves, selecting the peak amplitude of the P-wave reflection and applying the correction factor for broadside sensitivity $\cos^2(\theta)/\sin(\theta)$ (θ being the angle between the incoming and the horizontal fibre.), obtained from two point ray tracing. By applying this factor the synthetic DAS data is simulated. Then it can be tested if the reversed correction factor $\sin(\theta)/\cos^2(\theta)$ can correct the simulated DAS data for the limited broadside sensitivity, so that it can be interpreted.

Based on the results it can be concluded that SPECFEM can be used successfully for modelling DAS configurations. The CREWES toolbox from MATLAB is a sufficient tool box for ray tracing and achieving travel time and horizontal slowness. By applying a slope filter, to extract the surface waves, it became

clear that a receiver spacing of 0.5 m is preferred for the model considered here. Furthermore with the use of the correction factor for broadside sensitivity, DAS data can successfully be simulated and the reversed correction factor can be used to correct for limited broadside sensitivity in DAS data.

The limited broadside sensitivity is only one step in modelling DAS data and achieving synthetic DAS data. For further research it is desirable to improve the isolation of the P-wave reflections from the subsurface interface of interest, by designing a more advanced amplitude picker. To get a more realistic model, noise should be added to the reflection data followed by stacking the reflection data. SPECFEM3D instead of SPECFEM2D, is recommended to be used for further modelling, because of a more realistic 3D geometrical spreading of the source. For modelling DAS data the next step would be to convert the particle velocity to strain and research other parameters to eventually be able to compare it to real DAS data. But it is shown that DAS looks like a promising technique, where the outcomes of the considered model shows the correction factor for broadside sensitivity can improve the data for relatively small source-receiver offsets ($x=-250,+250$ m).

Contents

1	Summary	2
2	Introduction	6
3	Background	8
3.1	Distributed Acoustic Sensing	8
3.2	Limited Broadside sensitivity	9
3.3	Brief overview on recent DAS research	11
3.4	SPECFEM	14
4	Method	17
5	Results	20
5.1	SPECFEM models	20
5.2	Two-point ray tracing	25
5.3	Surface Waves	29
5.3.1	Filter applied to the two-layer model	29
5.3.2	Filter applied to the three-layer model	32
5.3.3	Filter applied to the three-layer model: particle velocity	32
5.3.4	Second filter applied to the three-layer model: particle velocity	33
5.4	Determining of θ , correction factor and reversed correction factor	37
5.5	Limited broadside sensitivity	39
5.5.1	Picking peak amplitudes: two-layer model	39
5.5.2	Simulation of DAS data and correction for limited broadside sensitivity: two-layer model	45
5.5.3	Picking peak amplitudes: three-layer model	49
5.5.4	Simulation of DAS data and correction for limited broadside sensitivity: three-layer model	54
5.6	Suggestion for conversion of particle velocity to strain	57
6	Discussion	60
6.1	SPECFEM wave propagation and the model building	60
6.2	Two point ray tracing	60
6.3	Surface waves	61
6.4	Limited broadside sensitivity	62
7	Conclusion	64
8	Acknowledgements	65
9	Appendix A: Validation tests	68
9.1	Testing Parameters	68
9.2	Influence of free surface	71

9.3	From an acoustic medium to an elastic medium and testing different sources	75
9.3.1	Elastic case: comparison of elastic force response and moment tensor response, source at 200 m depth.	80
9.3.2	Elastic case: source at and 1 m below the surface	82
9.4	Building the model	87
10	Appendix B: Explanation of the codes used.	95
11	Appendix C: Explanation $\cos^2(\theta)$	97

2 Introduction

Distributed acoustic sensing (DAS) is a technology that measures strain in the subsurface, with the use of fibre optics cables. Recently DAS gained more interest in geophysical studies because of its high spatial resolution which is between 1-10 m, successful use in high-temperature and high pressure conditions and the low costs compared to the traditional geophones used. The range of applications of DAS is wide and because of the flexibility of the fibre optic cables many configurations of the cables can be used, and both Vertical Seismic Profiling (VSP) and surface seismic are possible. The quality of DAS data depends on different parameters that need to be tested. Eventually DAS can be applied to for example monitor geothermal projects and CO₂-sequestration (Wang et al., 2018).

With distributed acoustic sensing the strain or strain rate in the subsurface is measured, based on the Rayleigh scattering principle. Pulses of laser signals are sent through the fibre and the interrogator measures the back-scatter light of these pulses. The time of the laser signal and it's back-scattered component are measured and converted to strain, using the speed of light and the refractive index of the fibre (Jousset et al., 2018).

DAS faces some challenges before it can fully be applied. One of these challenges is to account for the variation of cable sensitivity as a function of the angle of incidence of elastic waves, called broadside sensitivity. Limited broadside sensitivity is an issue for VSP as well as surface seismics. But when the fibre is orientated parallel to the surface, the fibre can be insensitive to P-waves travelling vertically. P-waves generate strain that is parallel to the direction of the wave propagation. Kuvshinov (2016) suggests a correction factor for this limited broadside sensitivity, which will be tested in this research. The surface seismics configuration is most applicable to DAS, due to fibre optic cables already being present parallel to the subsurface. Therefore, here we consider the role of broadside sensitivity specifically for the surface seismic application of DAS. The other problem for DAS is that it measures strain, but conventional geophones measure particle velocity. An important step is how to translate particle velocity to strain in order to compare both to each other. Other parameters influencing the DAS data is for example gauge length or the signal to noise ratio (S/N).

With the interest in DAS, but the challenges it faces the main question of this master thesis is as follows: *Can reflection information from Distributed Acoustic sensing be improved for broadside P-waves, in a surface seismics configuration?*

The approach for this new technique DAS is to first model DAS data with the spectral element solver SPECFEM. SPECFEM is an open-source spectral elemental modelling program, which can be used to model wave propagation (particle velocity). The aim is to translate the synthetic particle velocity data to DAS (strain) data, in order to be able to reach a good understanding of DAS data and be able to compare it to real DAS data. This thesis will focus on if

the synthetic particle velocity can capture broadside waves. Which is one step to achieving realistic synthetic DAS data.

3 Background

In this chapter background information will be given which is useful in understanding the steps that are taken in the rest of the thesis. First the technique distributed acoustic sensing (DAS) will be explained more briefly. Followed by an explanation of broadside sensitivity. Then a summary of recent DAS research will be stated and last an explanation of the spectral element program SPECFEM.

3.1 Distributed Acoustic Sensing

Distributed acoustic sensing, further referred to as DAS, is a technology that measures strain(-rate) with the use of fibre optic cables. A schematic layout of DAS can be found in figure 1. For the measurements of DAS data a fibre-optic cable is needed together with the interrogator and the data processing technology. The fibre is buried horizontally into the subsurface or put vertically into a well (other configurations are possible too). Laser pulses are sent from the interrogator into the fibre. Suppose, a seismic wave propagates through the subsurface and the wave stretches and compresses the layers in the subsurface. Then the fibre-optic cables responds to the movements or volume changes in the subsurface, by stretching and compressing as well. The movements in the subsurface will change the path length of the fibre and therefore also change the travel time of the pulses send out by the interrogator. Based on the Rayleigh back-scattering principle the pulses reflect when encountering small inhomogeneities in the cable. The pulses that are scattered back are measured again by the interrogator and the differences in travel time are translated to strain for the subsurface (Jousset et al., 2018).

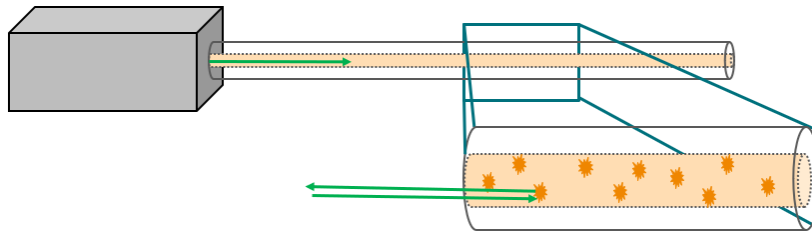


Figure 1: Schematic lay out of DAS. With the interrogator being the grey box. The interrogator sends out the laser pulses through the fibre. Zooming in to the fibre the laser pulses reflect at the inhomogeneities in the fibre based on the Rayleigh scattering principle.

DAS measures acoustic disturbances in an optical fibre, which is based on Rayleigh scattering. Rayleigh scattering is the interaction between inhomogeneities in a fibre and the pulses sent through the fibre. The inhomogeneities

are impurities in the fibre and are present throughout the fibre, ordered randomly. The laser pulse is being scattered at these inhomogeneities and part of the laser pulse is transmitted back to the interrogator (figure 1), which also contains the source of the pulses. The back scattered light can be analysed to provide information about the location of the scattering points and the strain on the fibre. The back-scattering pulses become a function of the acoustic strain on the fibre.

The fibre is sensitive to axial strain and radial strain. Axial strain is affecting the total length of the fibre and therefore changing the path length. Radial strain is changing the refractive index of the fibre (Lumens, 2014). The travel time of the pulse sent out and the travel time of back-scattered light arriving back at the interrogator are measured. Using the speed of light and the refractive index these travel times can be converted into distance values, which can be translated to where in the cable the strain changes. This physical principle is called optical time domain reflectometry (OTDR) and the application of OTDR to ground motion is called distributed acoustic sensing (Jousset et al., 2018).

3.2 Limited Broadside sensitivity

As was already been pointed out limited broadside sensitivity is one of the crucial factors in understanding DAS. In figure 2 a fibre is displayed, where axial strain is the change in path length and indicated by the green arrows and radial strain is indicated by the yellow arrows and is the change of the refractive index of the fibre. Due to the fibre being long but very thin the fibre can capture mostly the axial strain but can not capture the radial strain. In figure 2 two P-waves are indicated, where the left wave enters the fibre with a larger angle θ , this P-wave acts more on the radial strain of the fibre and is therefore harder to capture. The right wave is entering the fibre with a smaller angle and is more acting on the axial strain of the fibre and can therefore be better captured by the fibre. Limited broadside sensitivity, implies that the fibre is limited in measuring P-waves that enter the fibre with a large (broadside) angle.

From the literature is suggested that the amplitude response of the DAS fibre decreases when the angle between the seismic wave and the fibre increases. The response decreases roughly with a factor equal to $\cos^2(\theta)$ for VSP (Kuvshinov, 2016), which is also in agreement with figure 5. But in these papers VSP is researched, where the fibre is located vertically into a well. For this thesis we look at surface seismics, where the fibre is put in a trench parallel to the subsurface. In figure 3 the angle θ is defined by being the angle between the horizontal oriented fibre and the P-wave. In figure 4 a schematic lay-out for VSP and surface seismics are displayed. For both the surface seismics configuration and the VSP configuration the point force is acting vertically downward and for both the incidence angle is the angle between the P-wave and the fibre. But for surface seismics the fibre is oriented horizontally and for VSP the fibre

is oriented vertically, which gives a different relation between the fibre and incidence angle. Therefore for surface seismics is suggested to use $\cos^2(\theta)/\sin(\theta)$ as correction factor to simulate what the DAS fibre would measure for the model; simulate the horizontal component. Furthermore the reversed correction factor $\sin(\theta)/\cos^2(\theta)$ is then suggested to use for the correction of the limited broadside sensitivity; simulate the vertical component from DAS data.

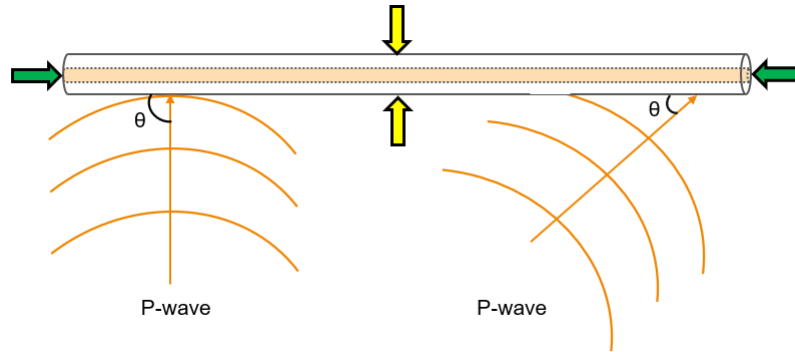


Figure 2: Fibre where the axial strain is indicated with the green arrows and the radial strain in indicated by the yellow arrows. Below two P-waves are entering the fibre with angle θ . The left P-wave enters the fibre with a larger incidence angle, which is acting on the radial strain. The right angle with a smaller incidence angle is more acting on the axial strain. The fibre can hardly capture the waves that enter the fibre with a large angle, due to limited broadside sensitivity.

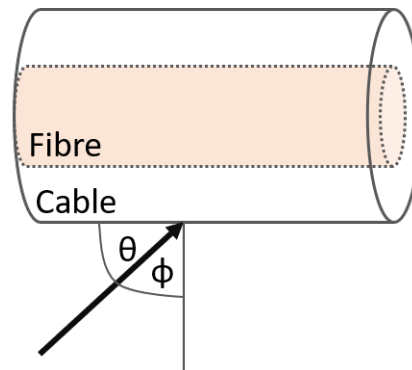


Figure 3: Shown is the difference between the angle (θ) with the horizontal and thus fibre and the angle ϕ with the vertical and the vertical force.

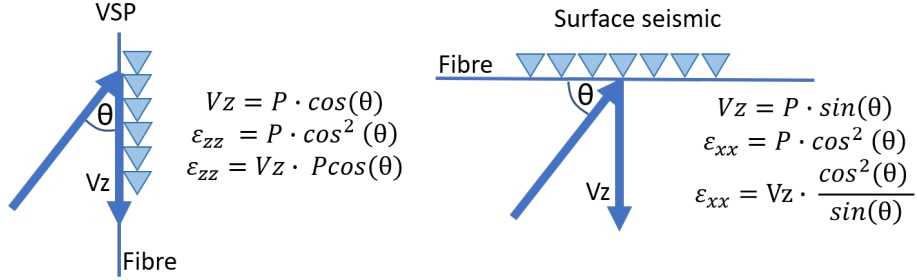


Figure 4: The angle of incidence for VSP and surface seismics and the difference in correction factor for both the situations. Since the fibre is vertically for VSP and horizontally for surface seismics, but the vertical force is facing downwards for both. The correction factor for VSP and surface seismics also changes, due to a different orientation of the incidence angle θ .

3.3 Brief overview on recent DAS research

With distributed acoustic sensing being a relatively new technique, it recently gained a lot of interest for seismic acquisition (Correa et al., 2017), (Daley et al., 2016). Already quite some research shows promising results for the applications of DAS. Although more research still needs to be done, due to the challenges that DAS faces. Below is a summary of recent research which is applicable to this thesis.

Correa et al. (2017) analyse the signal to noise ratio for DAS used in vertical seismic profiling (VSP), since DAS often has a high level of noise compared to conventional methods. The research shows how DAS behaves for different offsets and incidence angles, to better understand how DAS works. The DAS VSP data set from the CO2CRC Otway project, a CO2 geo-sequestration demonstration project, is compared to conventional geophone data. The survey shows that DAS has the potential to provide data sets that are comparable or even better than conventional geophone data.

Correa et al. (2017) propose an approach on how to convert DAS data to particle velocity, in order to compare both data sets. Suggested is to use a filter which translates the DAS strain data to particle velocity based on describing the displacement as a plane wave and integrating the data along the cable length. Furthermore when looking at the signal to noise ratio the up going and down going waves are well imaged, despite the high level of random noise. To increase the S/N the DAS data can be stacked in order to add more signal and decrease the noise. Another subject that has been brought up in Correa et al. (2017) is the directional sensitivity of DAS measurements, the direction of the particle displacement has effect on the DAS system and data. The directional sensitivity, high noise levels and lack of complete understanding is a hinder for broad application of DAS, but still DAS can already be used for imaging and

monitoring in certain configurations. With the advantage that DAS data might provide more detailed information due to higher spatial sampling.

In the research from Wang et al. (2018), DAS is compared to geophone measurements during an earthquake in Brady Hot Springs, Nevada. The DAS cable was oriented in a zigzag pattern in a trench below the surface, with co-located geophone stations. With the DAS- and geophone data, the signal to noise ratio is compared to test the relationship between them. Furthermore Wang et al. (2018) suggest that time integration is needed to convert from strain rate to strain, which also reduces the optical noise. The broadside effect for DAS is addressed, which Wang et al. (2018) measure. Which means that the strain rate, which is measured in the direction of the cable, will decrease in amplitude along the cable with a $\cos^2(\theta)$ factor (where θ is the angle between the fibre and the particle motion). To make this comparison they divide the DAS data by $\cos^2(\theta)$ and the geophone data by $\cos(\theta)$, since the geophone data is particle velocity and is linearly proportional to $\cos(\theta)$ and DAS data is measured in strain, which is linear proportional to $\cos^2(\theta)$ (further explanation can be found in Appendix C). They conclude that DAS and geophone recordings of the considered earthquake are similar. From which can be stated that the DAS- and geophone data appear very similar. Besides the recording of different physical variables for DAS and geophones, they are coupled differently and have different response functions. DAS-cable segments are used to convert strain to particle velocity in the f-k domain. Factors that influence the quality of DAS data are the optical noise, signal to noise ratio, near-surface heterogeneity and coupling of ground motion with the cable. Wang et al. (2018) concludes that in general the ground motion measured by DAS and geophones showed the same result and there is a high potential of DAS for contributing to earthquake analysis.

As mentioned before, limited broadside sensitivity is one of the key factors in understanding the DAS data, which is discussed thoroughly in Kuvshinov (2016). They suggest to counteract limited broadside sensitivity by helically winding the fibres in the cable. When the fibres are helically wound, the waves enter the fibre at different angles and limited broadside sensitivity should not be a problem anymore, but the helically wound fibre brings also challenges with it for the interpretation, compared to a straight fibre. And for surface seismics, fibres are put in a trench parallel to the surface, the fibre could be helically wound in the trench. However, there are also examples of where the fibres are already present as a straight fibre in the subsurface and not wounded helically. Therefore the configuration where the fibre is straight and oriented parallel to the subsurface deserves more research when it comes to the effect of limited broadside sensitivity.

Due to the rigidity of the silica glass from which a fibre is made of, a straight fibre is not sensitive to normally incident P-waves. One mostly deals with reflected body waves in surface seismics, that propagate nearly vertical and are therefore hardly measured by horizontal cables. To improve the limited broadside sensitivity a correction factor should be used. For VSP, most of the

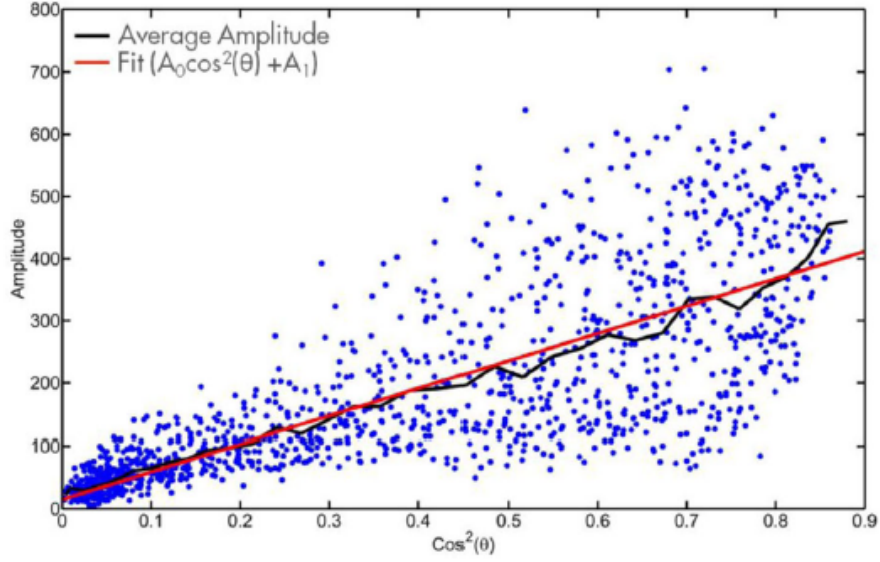


Figure 5: Raw DAS amplitudes (blue dots) plotted against the $\cos^2(\theta)$, θ is the angle of incidence for the first arrivals of a field trial. The red trend shows the $\cos^2(\theta)$ and the black line shows the average DAS amplitude. Figure achieved from figure 15, Mateeva et al. (2014)

reflected waves arrive close to parallel to the cable for small offsets, so limited broadside sensitivity doesn't have to be taken into consideration.

The strain in the cable is caused by seismic waves. Reflected P-waves, which are for this thesis the waves of interest, generate strain that is parallel to direction of wave propagation. The angle θ is the angle of incidence of the reflected p-wave with respect to the fibre. The DAS cable is put in a trench and parallel to the subsurface (e_{xx}). The projection of only non-zero radial strain component (e_{xx}^ω) along the cable is equal to $e_{||}^\omega = e_{xx}^\omega \cos^2\theta$. In most situations the cable is coupled to the surrounding medium, so that the axial strain in the cable ($e_{||}^c$) is equal to the axial strain in the impinging wave $e_{||}^\omega$ (Kuvshinov, 2016). The signal is proportional to $\cos^2(\theta)$. As has been suggested in field trials that limited broadside sensitivity causes the amplitude to decrease with a $\cos^2(\theta)$ factor and with an increasing angle (θ) (Mateeva et al., 2014). This is in agreement with figure 5, which shows the same trend for the DAS amplitudes and $\cos^2(\theta)$. The next question that is how this $\cos^2(\theta)$ exactly arises. DAS measures strain and strain is a tensor, with the projection of a tensor element $\cos^2(\theta)$ is achieved. This can be explained by the projection of a vector on a line being equal to $\cos(\theta)$. The projection of a tensor element on an vector is also equal to $\cos(\theta)$ which gives that the DAS signal along the fibre is proportional to $\cos^2\theta$. In appendix C is further explained how $\cos^2(\theta)$ arises.

3.4 SPECIFEM

The SPECIFEM package is an open source software package based up on the spectral element method (SEM), developed by Dimitri Komatitsch and Jean-Pierre Vilotte (Komatitsch and Vilotte, 1998). SPECIFEM2D (further referred to as SPECIFEM), is the 2D version used to perform 2D simulations of seismic wave propagation. SEM is a combination of a finite element method and spectral method. The spectral-element solver makes use of a mesher, which can be generated internal inside the program or external outside the program. For DAS modelling there has been made use of the internal mesher. Furthermore, the code is very well suited for parallel implementation (Komatitsch and Vilotte, 2018). There is also the SPECIFEM3D version but for this research SPECIFEM2D was adequate. SPECIFEM relies on the continuous Galerkin technique, which is a class of methods to convert an operator problem to a discrete problem (Tromp et al., 2008).

Other computational methods exist that can be used as alternative to spectral element method to spectral elemental methods (SEM) are finite difference, finite elements or spectral methods, each having their advantages. The finite difference method is widely used, but difficulties arise when it's accounting for surface topography and when anisotropy is taken into account. Spectral methods are restricted to smooth variations. Finite element methods have been successfully used, but these three techniques come with high computational costs. The spectral element method combines the flexibility of the finite element method and the accuracy of the spectral method. The spectral element method had already been used in computational fluid dynamics, but gained interest for wave propagation modelling too. In the spectral element method free-surface topography can be incorporated and the program can accurately propagate surface waves and body waves (Komatitsch and Tromp, 1999).

The spectral element method starts at the equation of motion and uses this in the weak-form (an integrated form). With the equation of motion the displacement field and therefore the propagation of seismic waves within a certain volume is determined. In this study we focus on a model-volume, which contains a stress-free surface and absorbing boundaries on the other edges. So seismic waves are reflected by the free surface and absorbed by the other three edges. In the weak form an integral of the equation of motion is used and just like in finite element methods this is the basis of the spectral element method. The weak form starts with the strong form, which is the displacement field of an earthquake described by the momentum equation (equation 1). In the momentum equation ρ is the density, s the displacement field, T the stress tensor and f a point force.

$$\rho \partial_t^2 s = \nabla \cdot T + f \tag{1}$$

The stress tensor T is linearly related to the displacement gradient (∇s) by Hooke's law, with the fourth-order elastic tensor c . Which can be written as:

$$T = c : \nabla s \quad (2)$$

The momentum equation must be solved with a stress-free boundary conditions, which represents the earth's surface:

$$T \cdot \hat{n} = 0 \quad (3)$$

Besides the stress free boundary at the surface, absorbing boundary conditions are implemented. Here the approximation is made by relating traction, which is the stress tensor times a unit vector pointing outward, $(T \cdot \hat{n})$ to velocity (v) .

$$T \cdot \hat{n} = \rho [v_n(\hat{\mathbf{n}} \cdot \partial_t s)\hat{\mathbf{n}} + v_1(\hat{\mathbf{t}}_1 \cdot \partial_t s)\hat{\mathbf{t}}_1 + v_2(\hat{\mathbf{t}}_2 \cdot \partial_t s)\hat{\mathbf{t}}_2] \quad (4)$$

With these equations in mind the weak form (an integrated form) can be constructed by dotting the momentum equation (equation 1) with a test vector w . Then it is integrated by parts over the model volume Ω , see symbol annotation in komatitschs and Tromp (19991). The stress free boundary condition is used (equation 3) and the absorbing boundary conditions in terms of traction (equation 4). Which gives the following equation for the weak form of the equation of motion (equation 5). Where M is the moment tensor and $S(t)$ is the source time function.

One of the features of the weak form is that it is actually equal to the strong form, because it holds for any test vector. Further the weak form naturally satisfies the stress-free surface. One of the down sides of this approach however is the additional computer memory needed.

$$\begin{aligned} & \int_{\Omega} \rho \mathbf{w} \cdot \partial_t^2 s d^3x = \\ & - \int_{\Omega} \nabla \mathbf{w} : \mathbf{T} d^3x + \mathbf{M} : \nabla \mathbf{w}(\mathbf{x}_s) S(t) \\ & + \int_{\Gamma} \rho [v_n(\hat{\mathbf{n}} \cdot \partial_t s)\hat{\mathbf{n}} + v_1(\hat{\mathbf{t}}_1 \cdot \partial_t s)\hat{\mathbf{t}}_1 + v_2(\hat{\mathbf{t}}_2 \cdot \partial_t s)\hat{\mathbf{t}}_2] \cdot \mathbf{w} d^2x \end{aligned} \quad (5)$$

SPECFEM can use a Cartesian coordinates system with x on the horizontal axis and z on the vertical axis with zero at the bottom of the model and the z -vector pointing positive upward (this might be counter intuitive, since many models hold the z -vector negative downward and zero at the free surface).

The model volume is defined by a mesh, which consists of non-overlapping elements. Opposed to FEM, SEM is restricted to hexahedral volume elements. The volume then consists of boundary elements and volume elements. The elements are described by shape functions. These shape functions are products of Lagrange polynomials of degrees 1 or 2 (low degree), which are used for polynomial interpolation between the nodes that build up the individual elements.

To solve the weak form of the equation of motion an integration over the volume and absorbing boundary is divided into smaller integrals over the surface and volume elements. To define the displacement fields on the elements, high degrees of Lagrange polynomials are used. Control points in the Lagrange polynomials are chosen to be Gauss-Lobatto-Legendre points (Komatitsch and Tromp, 1999). So on each individual element, functions are sampled at the Gauss-Lobatto-Legendre points of integration. There is a difference between the local mesh of one element and the global mesh of the whole volume. The determination of mapping between the grid points of the local mesh and the global mesh is called the assembly phase. All the elements that share a global grid point need to be summed up before the system can evolve over time. An advantage of SEM is that the mass matrix is diagonal, so the system can easily evolve in time. SEM is capable of handling heterogeneous media well, since the density can vary over grid points within an individual element. (Komatitsch and Tromp, 1999).

To run the SPECFEM code different input files are required. A separate input file exists for defining the source, the sets of receivers and the interfaces in the model. The fourth input file is the parameter file in which one can change the different settings, elements and parameters. After running the code the output files consist of images of the wave propagation, wave field for each time step and the amplitude for each time step in the x- and z-direction. One can choose which output SPECFEM generates: pressure, displacement or particle velocity etc. At the start of this thesis validation tests were done for SPECFEM in order to test several parameters and different source representations. The results from these tests can be found in Appendix A.

4 Method

The bigger picture is to model synthetic DAS data in order to compare it to conventional geophone data and real DAS data. The method for simulating synthetic DAS data, starts with a SPEC-FEM model, which is presented in figure 6; with a workflow diagram. The orange box in figure 6 indicates the part where the focus for this thesis is on, from which the workflow can be found in figure 7.

First, SPEC-FEM a spectral elemental solver is used to obtain synthetic particle velocity data through wave propagation modelling. Several validation tests are carried out to research how several parameters are implemented in SPEC-FEM: Tests are performed to understand the transfer from an acoustic to an elastic model, how different sources can be used (sources available in SPEC-FEM are an elastic force, acoustic pressure and a moment tensor). Furthermore the influence of the free surface and different configurations of the receivers are tested. The results of these validation tests can be found in Appendix A. After the validation test SPEC-FEM is used to compute a model for DAS configuration from which synthetic shot data can be achieved.

Parallel to SPEC-FEM, the MATLAB toolbox CREWES is used (Margrave, 2000). With the two point ray tracing code the travel time and horizontal slowness is computed for a given velocity model. With the output the incidence angle (θ) can be calculated which is needed for correction factor and reversed correction factor.

After these two steps the processing of the synthetic shot panels from SPEC-FEM can be started. Seismic Unix has been used to filter out the surface waves (Cohen and Stockwell). The shot panels are transferred to a .sgy file, in seismic unix the .sgy file can then be transferred to a .su file. The surface waves are filtered out since they have an amplitude of one to two orders of magnitude bigger than the P-wave reflections of our interest. Due to the clear slope of the surface waves in the offset (x), time (t) domain (offset being the distance between source and receiver), the slopes can be filtered out with the use of *sudipfilt*. With this filter a range of slopes is selected that is set to zero in order to filter out the slope of the surface waves. Selecting this range of slopes happens for this situation in a trapezium, so four slope-values are selected, the first and the last slope-value are set to 1 and the middle slope-values are set to zero. The filter interpolates between the values of the selected slopes and filters out the surface waves. The middle values of the slopes are chosen such that they surround the main slope of the surface wave, which can be calculated with $\delta t / \delta x = slope$. Slope values are chosen that prevent from aliasing but also doesn't filter away too much reflection information of the panel. After filtering the .su file is transferred back to a .sgy file in order to plot the shot panels again in MATLAB.

After the surface waves are removed the next step is selecting the P-wave reflec-

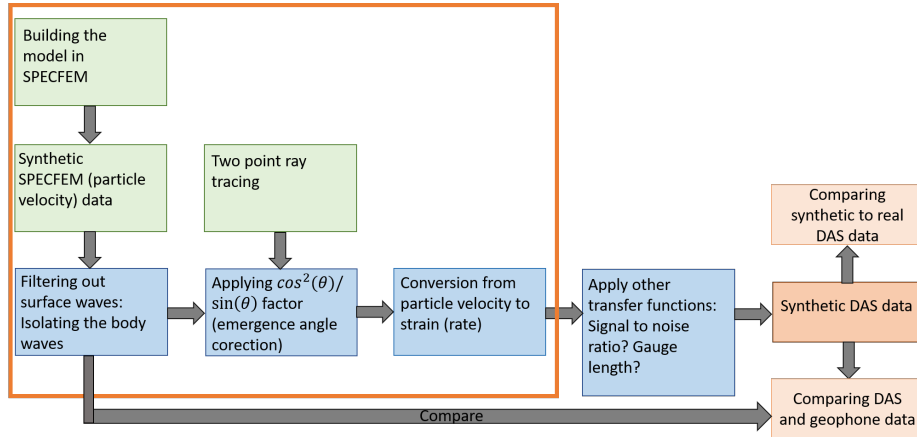


Figure 6: Workflow for simulating DAS data starting from synthetic SPECSEM geophone data in particle velocity to synthetic DAS data, which is strain. The orange box surrounds the workflow for this thesis.

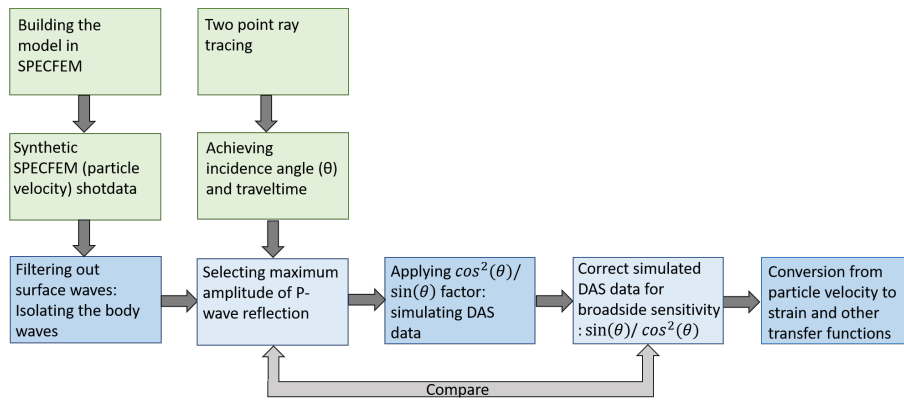


Figure 7: Workflow of this thesis. Starting with SPECSEM at the left top. Parallel to SPECSEM the two-point ray tracing is computed. And at the left bottom the processing of the synthetic shot panels is started. Eventually the shot panel for which is corrected for limited broadside sensitivity is compared to the originally picked reflection amplitudes.

tion in order to simulate what the DAS fibre would measure and correct for the broadside waves (figure 7). Selecting the P-wave reflection is done by designing an amplitude picker in MATLAB that will search for the peak amplitude for a given search window.

From the two point ray tracing, the horizontal slowness as output is used to calculate the incidence angle: the $\sin(\theta)$ can be determined with $p = \sin(\phi)/v$. With (ϕ) being the angle with the vertical, the angle θ ($\theta = \pi/2 - \phi$) is the angle with the horizontal and thus the angle with the fibre can be determined with this relation. Using the relationship $\cos^2(\theta) + \sin^2(\theta) = 1$, the $\cos^2(\theta)/\sin(\theta)$ factor and the reversed factor $\sin(\theta)/\cos^2(\theta)$ can be determined and are applied later to the synthetic particle velocity.

When the peak amplitude is selected the correction factor can be applied to simulate the data that the DAS fibre would measure ($\cos^2(\theta)/\sin(\theta)$). Next the amplitudes measured by the DAS fibre are corrected by the reversed correction factor ($\sin(\theta)/\cos^2(\theta)$), to correct for the broadside waves. The last step is to compare the amplitudes including the correction for the broadside waves to the originally picked peak amplitudes of the P-wave reflection. In appendix C the workflow of the scripts is displayed (figure 94) and explained in more detail.

5 Results

In this chapter the results are stated for the different steps indicated in the workflow (figure 7). First the building of the model in SPECFEM is stated. Then the results of the ray tracing are shown followed by the filtering in Seismic Unix, first for the two-layer model and then the three-layer model. Then from the output of the two-point ray tracing the incidence angle θ , correction factor and reversed correction factor are calculated. Next the correction factor is applied to achieve simulated DAS data and the inversed correction factor is used to correct for the limited broadside sensitivity in the simulated DAS data, which is first done for the two-layer model and then for the three-layer model. Finally some suggestions are proposed for the conversion of particle velocity for strain based on literature.

5.1 SPECFEM models

After the validation tests (Appendix A) the research is continued with a two-layer model with one reflector at 200 m depth and a three-layer model with a second reflection at 20 m and 200 m depth. The top layer has low velocities and acts as a weathering layer. The source used for both models is a point source acting vertically downward, the function type is a Ricker wavelet, with a source frequency of 40 Hz. The P-wave reflection at the reflector at 200 m depth is the wave of interest. The rest of the steps are first done for the more simplistic two-layer model and then with the less simplistic three-layer model. In figure 8 the schematic lay-out of the two-layer model can be found and in figure 9 a time snapshot. For the three-layer model the schematic lay-out can be viewed in figure 11 and a time snapshot in figure 12. Further more is the shot panel for the three-layer model also plotted in figure 13 for the z-direction and the two-layer model for the z-direction is plotted in figure 10. Looking at the shot panels, the surface waves appear with a very large amplitude, due to panel scaling the surface waves suppress the information of the other waves. Therefore it is decided to remove surface waves with a filter. The P-wave reflections of interest is the P-wave that reflects at 200 m, both for the two-layer model as the three-layer model.

On top of the shot panel (figure 10 and 13) the theoretical arrival times are plotted. The equations of the theoretical arrival times are stated in equation (6)- (11). The theoretical arrival times will be plotted for the direct P-wave, direct S-wave and the reflected P-wave and S-wave according to the equations that can be viewed below. V_{p1} (m/s) and V_{s1} (m/s) are the velocities of the top layer, z_1 (m) is the length of the top layer and x (m) the length of the x-axis. In figure 14 a spectral plot of the frequency versus power can be viewed, this is the spectral plot for trace number 2000 (in the middle of the shot panel) in the three layer model.

$$\text{Arrival time direct P-wave} = \sqrt{x^2}/V_{p1} \quad (6)$$

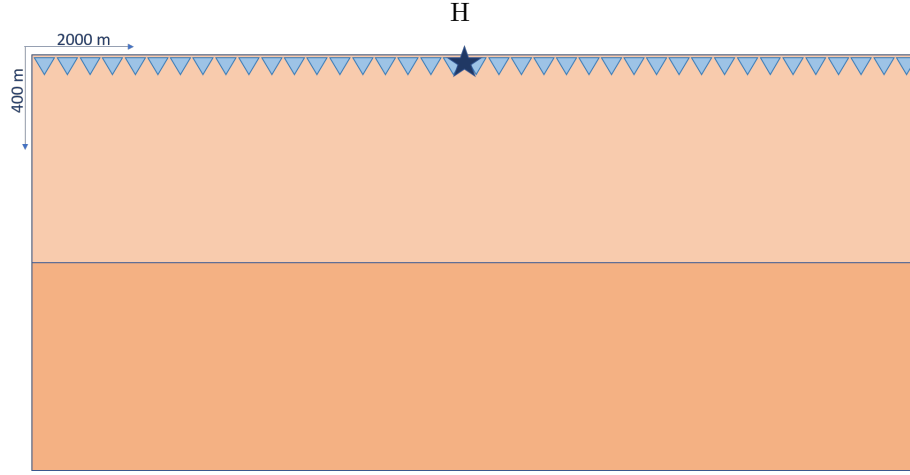


Figure 8: Geometry of the model where one reflector is built-in at 200 m depth: two layer model. For the top layer $V_p=2000$ m/s and $V_s=1176$ m/s, for the bottom layer $V_p=4000$ m/s and $V_s=2353$ m/s. Source and receivers are located 1 m below the free surface (buried in a trench).

$$\text{Arrival time direct S-wave} = \sqrt{x^2}/V_{s_1} \quad (7)$$

$$\text{Two-way vertical P-wave travel time : } tp_0 = \frac{2 * z_1}{V_{p_1}} \quad (8)$$

$$\text{Two-way vertical S-wave travel time : } ts_0 = \frac{2 * z_1}{V_{s_1}} \quad (9)$$

$$\text{Arrival time reflected P-wave} = \sqrt{tp_0^2 + \frac{x^2}{V_{p_1}^2}} \quad (10)$$

$$\text{Arrival time reflected S-wave} = \sqrt{ts_0^2 + \frac{x^2}{V_{s_1}^2}} \quad (11)$$



Figure 9: Snapshot of the model with one reflector at $t=3600$ msec: two layer model, particle velocity.

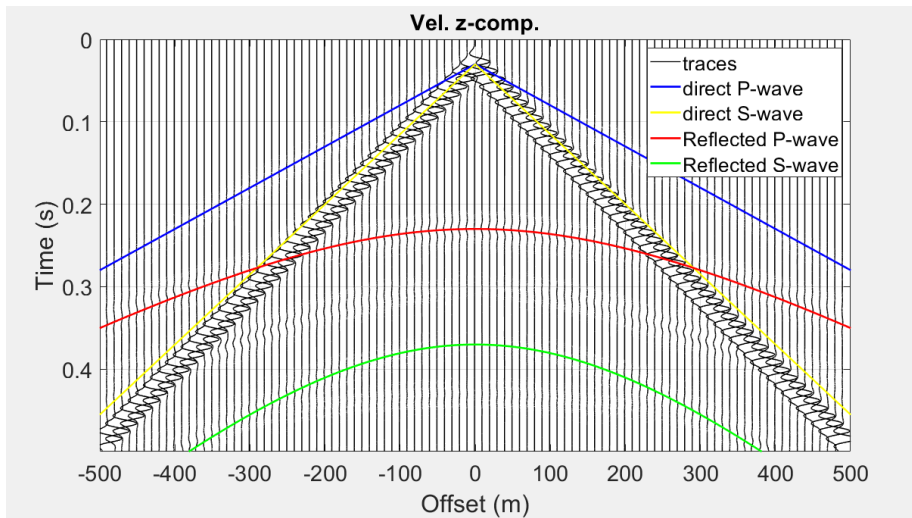


Figure 10: Panel for particle velocity in the z -direction, with one reflector the medium at $z=200$ m, two layer model. Traces are scaled to the maximum of each trace and every 10 traces one trace is plotted and $sc=20$ (scaling factor, amplitude * sc -value). On top of the traces the expected arrival times are plotted for the direct P- wave and S-wave and reflected P-wave and S-wave.

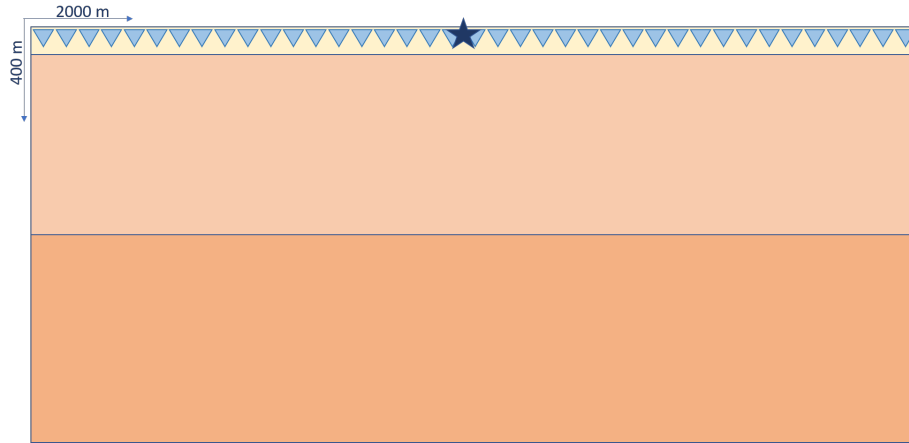


Figure 11: Geometry of the model in which a shallow reflector is built-in at a depth of 20 m; to create a weathering layer: three layer model. For the top layer $V_p=750$ m/s and $V_s=441$ m/s, for the middle layer $V_p=2000$ m/s and $V_s=1176$ and for the bottom layer $V_p=4000$ m/s and $V_s=2353$ m/s. Source and receivers are located 1 m below the free surface (buried in a trench).

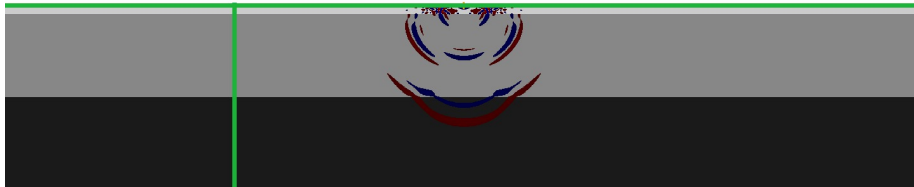


Figure 12: Snapshot of the model with two reflectors at $t=3200$ msec: three layer model, particle velocity.

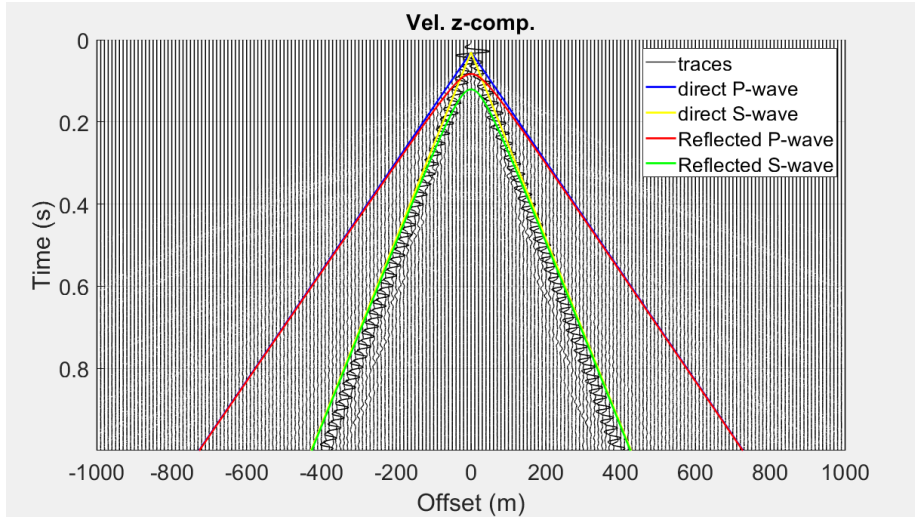


Figure 13: Shot panel for the velocity in the z-direction with a reflector at 20 m and 200 m: three layer model. Plotted is one trace every 20 traces and $sc=20$ and panel scaling.

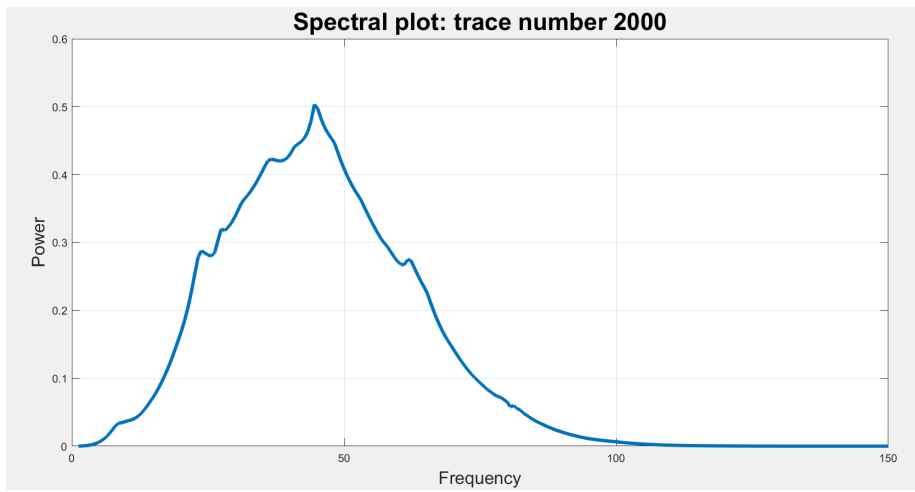


Figure 14: Spectral plot of trace number 2000 of the three layer model. Frequency versus power.

5.2 Two-point ray tracing

As is explained in (Margrave, 2000) the CREWES toolbox can be used for a number of seismic modelling facilities, for this thesis the tool for two-point ray tracing is used. With two point ray tracing, rays are traced between the beginning point (source) and the end point (receiver) for a given velocity model. Two point ray tracing routines are available for P-P and P-S reflections. The $v(z)$ ray tracing is used here, which solves the ray tracing differential equation on a 2D grid. The $v(z)$ ray tracing facility is a fast ray tracer that determines the travel time and horizontal slowness for an isotropic horizontally layered medium.

Ray tracing for a horizontally layered media, with constant velocity in each layer can be determined with analytical expressions (Margrave, 2000). The expression for the travel time for one layer is given in equation 12, together with the horizontal distance travelled stated in equation 13, which is through a numerical implementation of the integral equations for travel time and depth known from elementary seismology. Where t is the travel time calculated, x the distance calculated, $v(z)$ the velocity in the vertical direction, and p the horizontal slowness. These expressions can be implemented for several layers (N); these expression can be seen in equations 14 and 15, where z is the specific layer and N the number of layers. These equations are the basis for two-point ray tracing. For the ray tracing an iterative procedure is used, to trace the rays from the starting point to the end point. The procedure can be repeated until the ray is found within the user-specified 'capture radius' of the receiver accuracy parameters. With the MATLAB function '*traceray - pp*' the iterative procedure is used to find the ray from the source to the receiver via a reflector. In the function several different horizontal layers with different velocities can be implemented including the reflector at a certain depth, although the velocities need to be homogeneous throughout the horizontal layer.

$$t(p) = \int_{z_1}^{z_2} \frac{1}{v(z)\sqrt{1-p^2v^2(z)}} dz \quad (12)$$

$$x(p) = \int_{z_1}^{z_2} \frac{pv(z)}{\sqrt{1-p^2v^2(z)}} dz \quad (13)$$

$$t(p) = \sum_{k=1}^N \frac{\Delta z_k}{v_k \sqrt{1-p^2v_k^2(z)}} \quad (14)$$

$$x(p) = \sum_{k=1}^N \frac{pv_k \Delta z_k}{\sqrt{1-p^2v_k^2(z)}} \quad (15)$$

Since the *pp - raytracing* allows to implement one single reflector the *pp - raytracing* is run separately for a reflection at 20 m, 200 m and 400 m. Because some rays will already reflect at 200 m or 20 m depth. In this way three

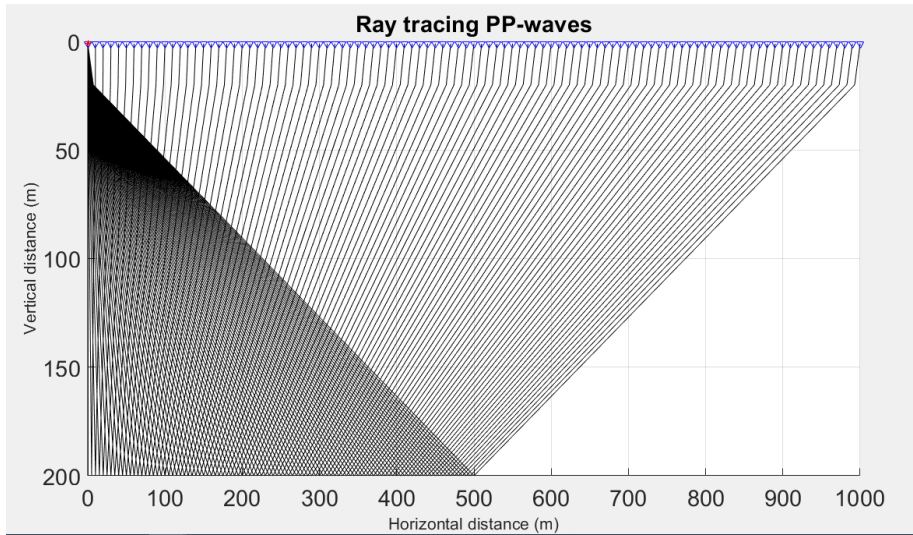


Figure 15: Two point ray tracing for P-wave reflection with the use of toolbox CREWES, reflector at 200 m. Plotted is a receiver every 20 meter.

scenarios are constructed, also for further calculations. With the code of the ray tracing the results can be plotted, which shows the ray from the source to the receiver with a reflector. The ray tracing results for PP reflections can be seen in figures 15 and 16. Not all rays are plotted for these figures since the individual rays wouldn't be clearly visible anymore. The plot with a reflector at 20 m is not plotted here, since the layer is very thin the plot gave a block where no rays could be distinguished.

With the output from the ray tracing for the P-wave reflection, the horizontal slowness and travel time can be plotted. For the ray tracing, only positive values for the x-axis can be used. To get the horizontal slowness and travel times for the whole panel, the output data is flipped and duplicated. The plots of the output data can be found in figures 17 and 18 for the three different scenarios where the reflector is located at a depth of 20 m, 200 m and 400 m.

Besides the horizontal slowness the other output from the ray tracer is travel time. The travel time from CREWES can be compared to the theoretical travel times that were calculated earlier. The plot of the numerical travel times from CREWES and the theoretical travel times can be seen in figure 19. It can be stated that the arrival time from the reflector at 20 m depth for the ray tracing and analytical P-wave reflection time come quite close, which means that the equation for the theoretical arrival times can be easily used, for this reflector. Furthermore it can be seen that for a reflector at 20 m the direct wave and the reflected P-wave come quite close because of the short distance.

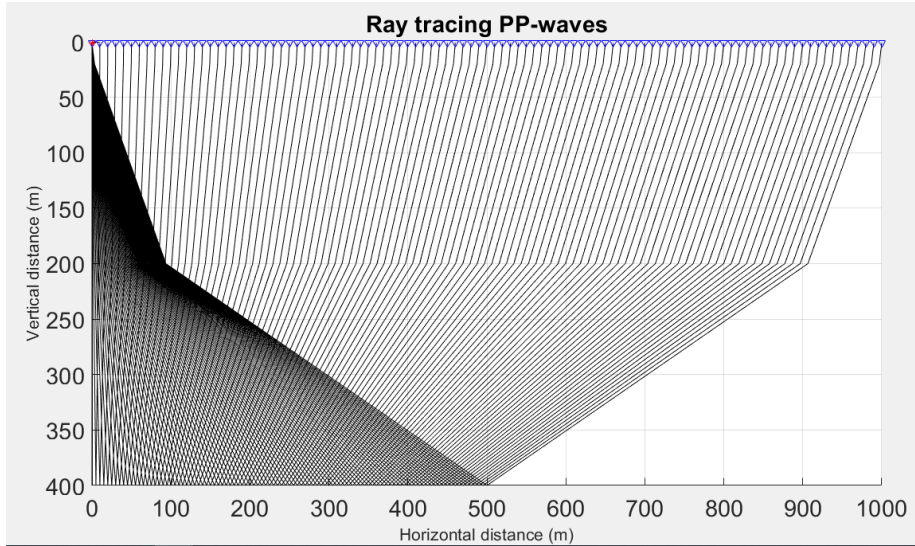


Figure 16: two point ray tracing for P-wave reflection with the use of toolbox CREWES; reflector at 400 m. Plotted is a receiver every 20 meter.

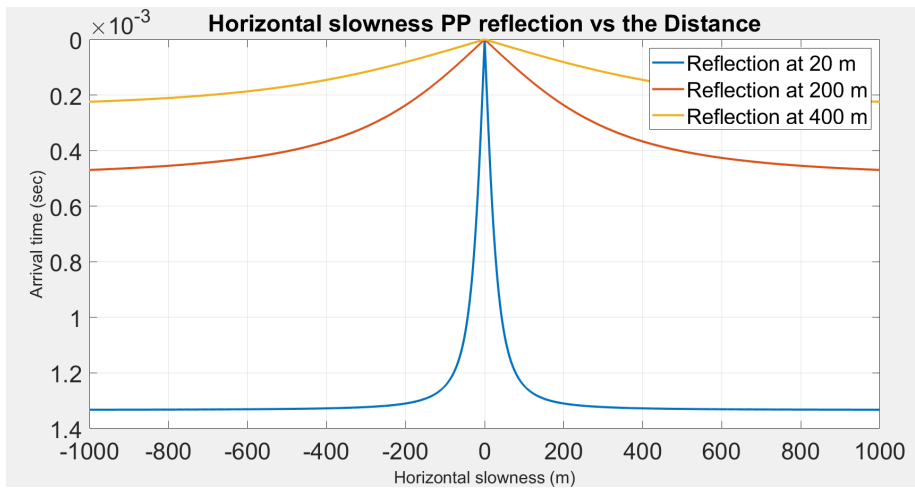


Figure 17: Plot of the horizontal slowness produced from pp-ray tracing versus the offset for the three different scenarios.

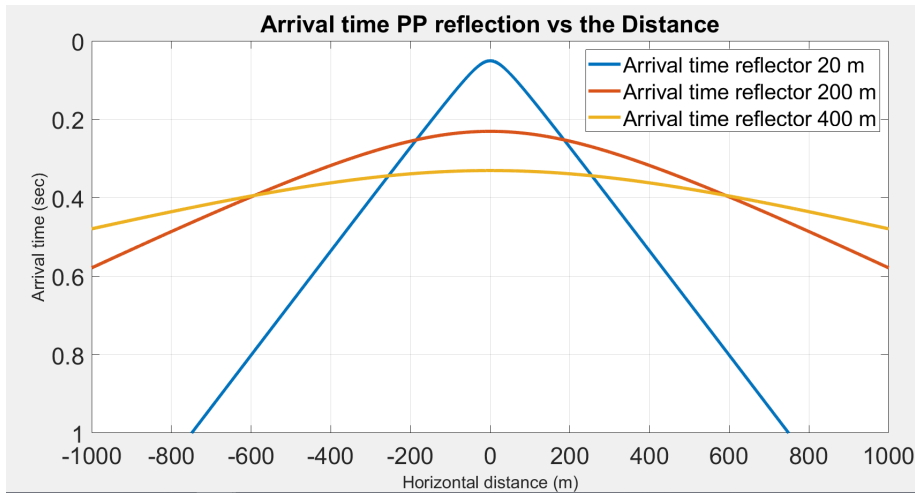


Figure 18: Plot of the arrival times calculated from the pp – raytracing for the three different scenarios.

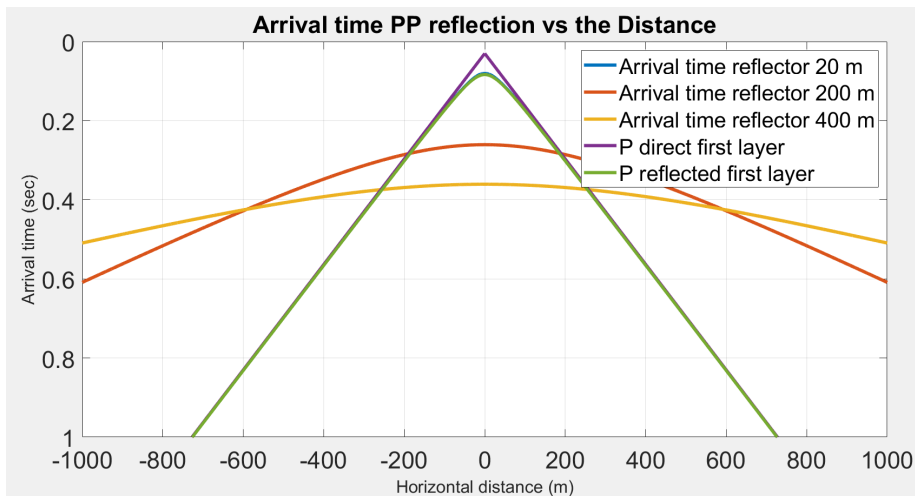


Figure 19: Plot of the ray arrival times, from the pp – raytracing and equations for arrival time stated earlier.

5.3 Surface Waves

The surface waves in the shotpanels, are mainly Rayleigh waves, generated in a surface-seismic survey. The surface waves are suppressing the other waves in the panels, due to the large amplitude of of the surface wave. The P-wave reflections, which are the waves of our interest, are also suppressed by the surface waves. Therefore a filter is designed to filter out the surfaces waves. This is done with the use of Seismic Unix, which is explained in more detail in appendix C.

5.3.1 Filter applied to the two-layer model

The filter in Seismic Unix is first applied to the two-layer model with a receiver spacing of 1 m. Results of the applied filter can be viewed in figure 20. In 20a is the panel shown before filtering plotted in Seismic Unix. In 20b and 20c the panels are shown when the filter is applied. Due to the filter used, spatial aliasing occurs. The spatial aliasing can be seen in the plots, by flipping and periodically repeating the slopes that are selected by the filter. The panels plotted in Seismic Unix, are scaled to a perc-value, this means that the percentage given is clipped (plot is blown up and dynamics range decreases).

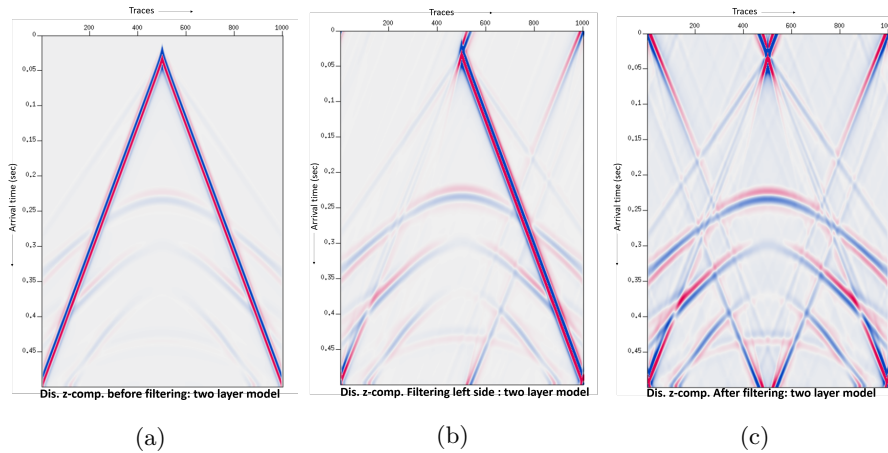


Figure 20: Filter applied to the two layer model for the z-component of the displacement. figure 20a shows the panel before filtering, in figure 20b the filter is applied to the left slope, aliasing occurs. Filter used: slopes=-0.0015,-0.00095,-0.00090,-0.00080 amps=1.,0.,0.,1. perc=99. In figure 20c the filter is applied to both sides, aliasing occurs. Filter is: slopes=-0.0015,-0.00095,-0.00090,-0.0008,0.0008,0.00090,0.00095,0.0015 amps=1.,0.,0.,1.,1.,0.,0.,1.

Since aliasing occurs quite severely with the receiver spacing of 1 m, the two-layer model is run again with a receiver spacing of 0.5 meter. In this way the data will be sampled more precisely, and hopefully it will prevent the data from aliasing when the filter is applied. The results from the filter can be viewed in

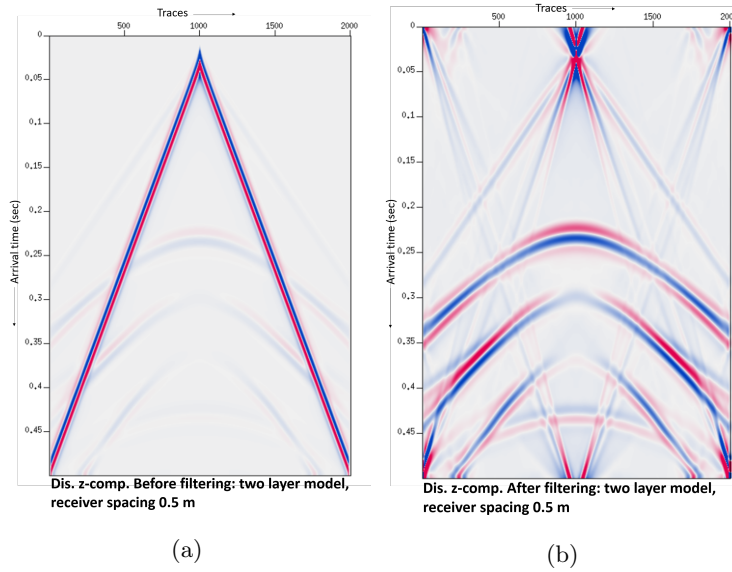


Figure 21: The two layer model for the z-component of the displacement plotted with Seismic Unix, before filtering. Receiver spacing is 0.5 m figure 21a. The two layer model for the z-component of the displacement, after removal of the surface waves figure 21b. Receiver spacing is 0.5 m. Filter used: slopes=-0.00070,-0.00050,-0.00040,-0.00020 amps=1.,0.,0.,1 perc=99.5

figure 21 where 21a shows the panel before filtering and 21b shows the result after filtering.

In figure 22 two examples of different filters are shown; 22a shows a filter where also aliasing occurs and 22b shows a filter where too much information of the panel is filtered away. Based on these plots it can be stated that a smaller receiver spacing results in more data points on the x-axis, which gives a smaller slope value when calculating $\delta t/\delta x$. With a smaller slope a more precise and accurate filter can be designed. The best filter is where no aliasing occurs, but also where not too much information is filtered out. The result of this filter is shown in figure 21b for this model. Looking at these plots the plot-scaling needs to be kept in mind. The plot will always be scaled to the maximum value of the plot. When a plot is shown where the filter is only applied to one side, the filtered and unfiltered part can be compared to each other. When looking at the filtered plot, the filter is already applied and information is taken out. Therefore the plot is scaled to a new (smaller) maximum. So, for comparing the plot before filtering and after filtering it should be kept in mind that different scaling maxima are used.

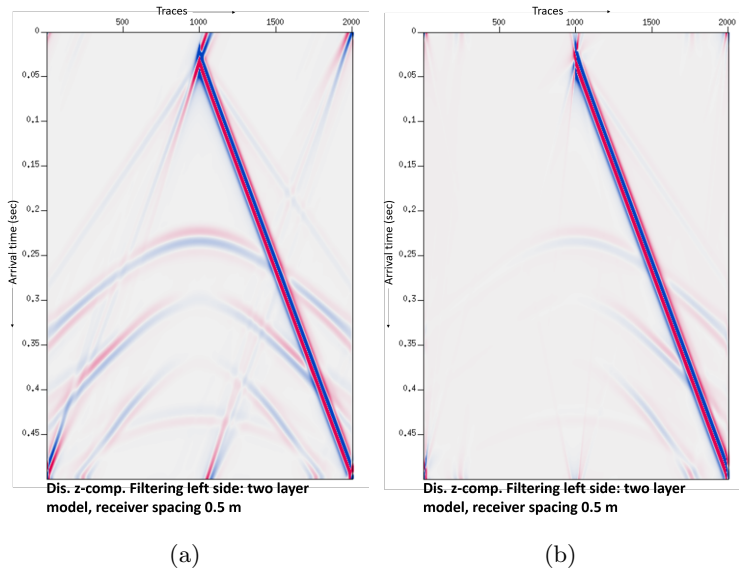


Figure 22: The two layer model for the z-component of the displacement plotted with Seismic Unix, after filtering. Receiver spacing is 0.5 m. Aliasing occurs in figure 22a. Filter used: slopes=-0.00058,-0.00048,-0.00043,-0.00033 amps=1.,0.,0.,1. perc=99. In figure 22b the two layer model for the z-component of the displacement plotted with Seismic Unix, after filtering. Receiver spacing is 0.5 m. Too much information is filtered away. Filter used: slopes=-0.00166,-0.00066,-0.00016,0.00084 amps=1.,0.,0.,1. perc=99.

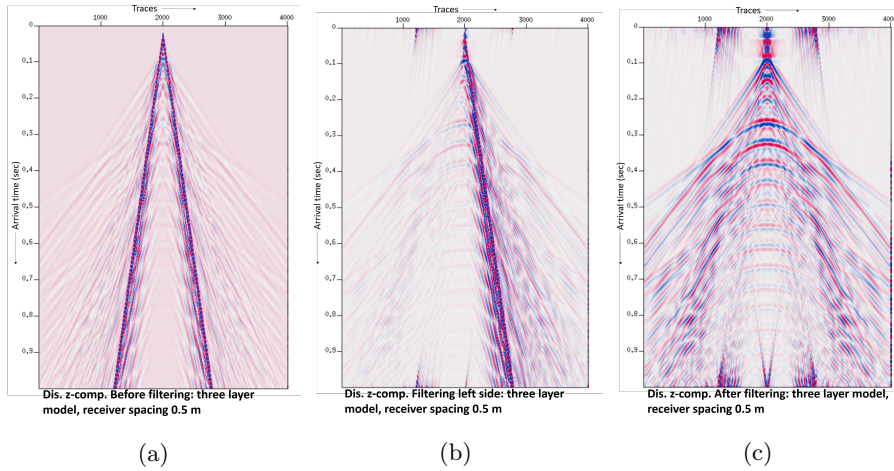


Figure 23: Filtering of the three layer model with a receiver spacing of 0.5 m for the z-component of displacement, figure 23a shows the panel before filtering, figure 23b shows the filter applied to the negative side of the panel. Filter used: slopes= $-0.0019,-0.0013,-0.0005,0.0000$ amps= $1.,0.,0.,1.$ perc=99. figure 23c shows the filter applied to both sides of the panel. Filter used: slopes= $-0.000,0.0005,0.0013,0.0019$ amps= $1.,0.,0.,1.$ perc=99.5

5.3.2 Filter applied to the three-layer model

After testing the filter with the two layer model the next step is to apply the filter to the three layer model for displacement, with an extra reflector at 20 m that acts as the bottom of the weathering layer. From the two layer model it has become clear that a receiver spacing of 0.5 meter is more precise and therefore better, so the receiver spacing of 0.5 m is also used for the three layer model. Figure 23a shows the panel before filtering. What stands out from this plot, is the presence of strong surface waves due to the weathering layer. The different waves interact with each other; surface waves are visible but not as clear as in the two layer model. The result from the filter applied to the left side of the panel, can be seen in figure 23b. Here the difference between the filtered and unfiltered part becomes clearly visible. The result of the filter applied on both sides can be seen in figure 23c; note that the plot is scaled to the maximum of the plot, so when the surface waves are filtered out the weaker information from the panel before appears much strong after application of the filter. After application of the filter the P-wave reflections become better visible.

5.3.3 Filter applied to the three-layer model: particle velocity

The next step is to filter the shot panel from the z-component of particle velocity of the three layer model. The result can be seen in figure 24. Figure 24a shows the panel before filter, in figure 24b where the filter is applied to the left-side of

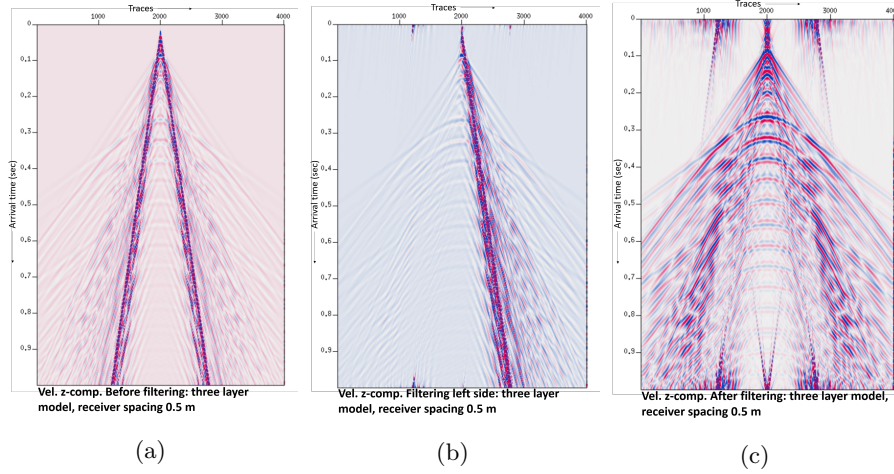


Figure 24: Filtering of the shot panel, z-component of particle velocity for the three layer model. Figure 24a shows the panel before filtering. Figure 24b shows the panel after the filter was applied to the left-hand side. Filter used: slopes= $-0.0025, -0.0013, -0.0005, 0.0007$ amps= $1., 0., 0., 1.$ perc= 99 . In figure 24c the filter was applied to both sides. Filter used: slopes= $-0.0007, 0.0005, 0.0013, 0.0025$ amps= $1., 0., 0., 1.$ perc= 99.5 .

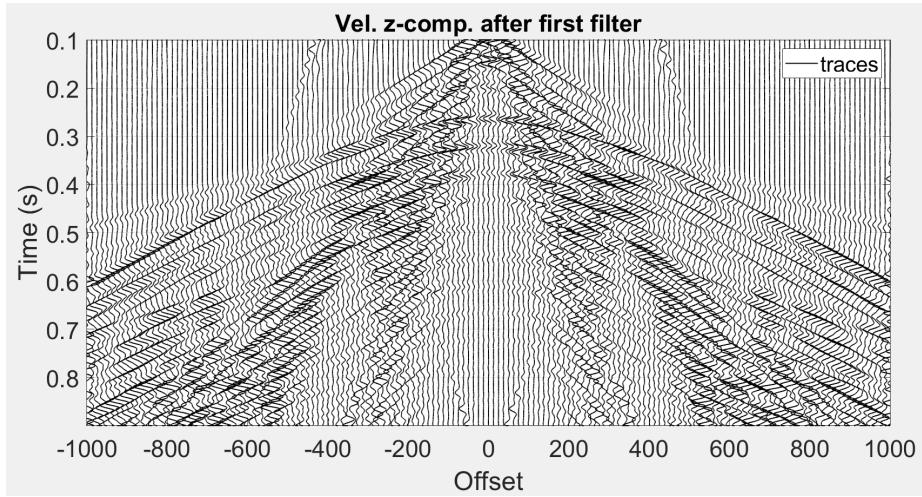
the panel and figure 24c shows the filter applied to the whole panel.

After filtering the shot panels are plotted again in MATLAB to see the results of applying the filter, which can be viewed in figure 25a. On top of the shot panel the theoretical times are plotted, which were explained earlier (figure 25b). From here it can be stated that the surface waves seem to be filtered out, but the direct P-wave and the P-wave reflected a 20 m seem to be almost identical, therefore the direct wave at the top layer is also filtered out with a second filter, to get the P-wave reflection at 200 m depth more clear.

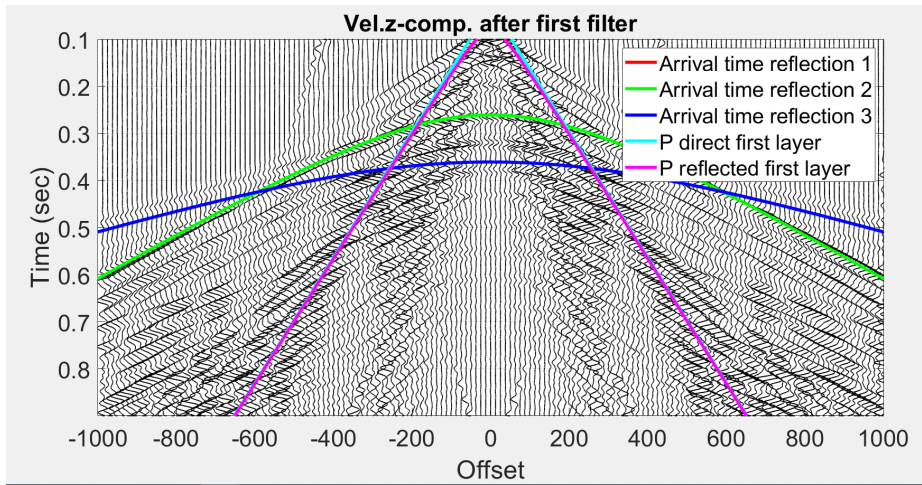
Since it is inevitable to get aliasing in the three layer model, due to the very low weathering-layer velocity, the panels still shows aliasing after application of the filter. Therefore it is chosen to only plot from $t=0.1=0.9$ msec, since this the time interval of interest. In this way most of the aliasing is not plotted anymore and the data can be better scaled to its maximum, and the reflection becomes better visible (figure 25).

5.3.4 Second filter applied to the three-layer model: particle velocity

As has been explained in the previous section, a second filter is designed to filter out the direct wave of the top layer from the panel. This is done so that the reflection at 200 m depth becomes more clear. The results of this filter can be seen in figure 26. Figure 26a shows the panel before application of the second filter which is the same as the result of the first filter (figure 24c). In figure



(a)



(b)

Figure 25: Panel of the three layer model after application of the first filter in figure 25a. In figure 25b the same panel is plotted together with the expected arrival times. For both figures $sc=20$ and one in every 25 traces is plotted.

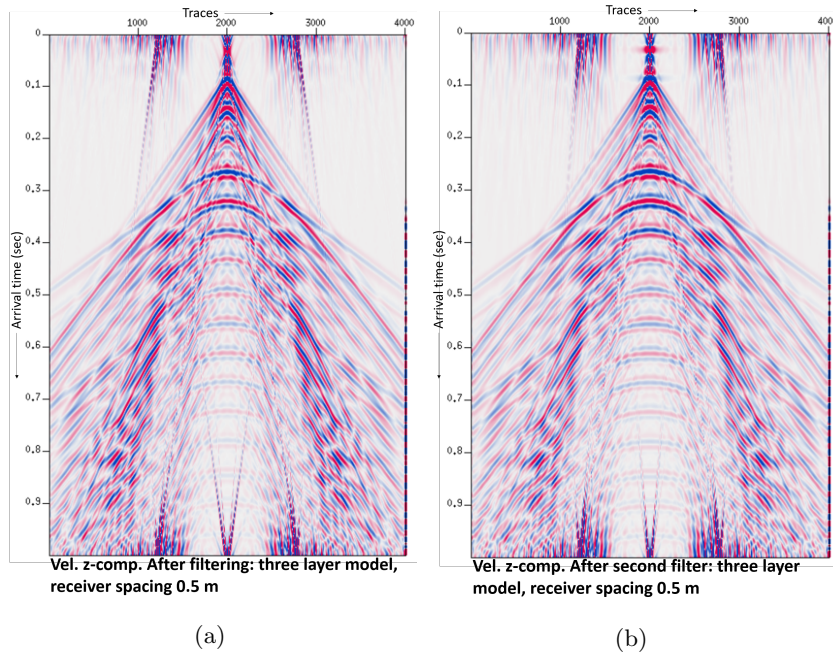
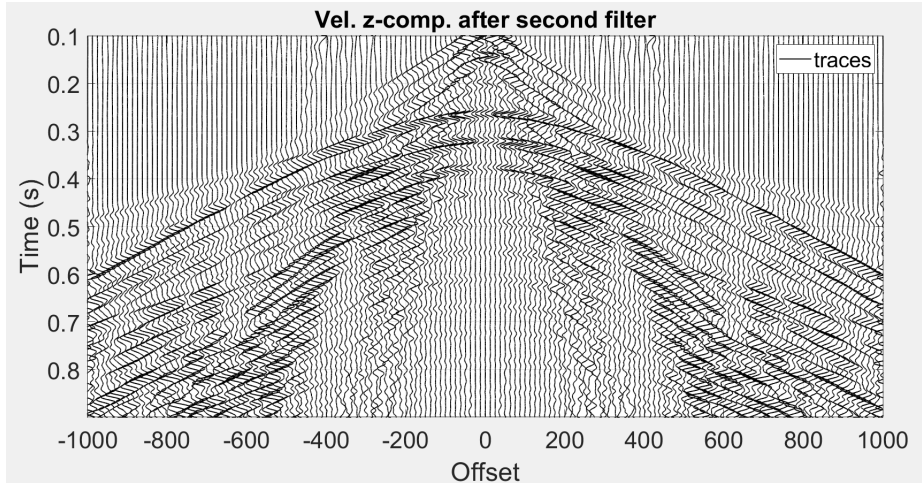
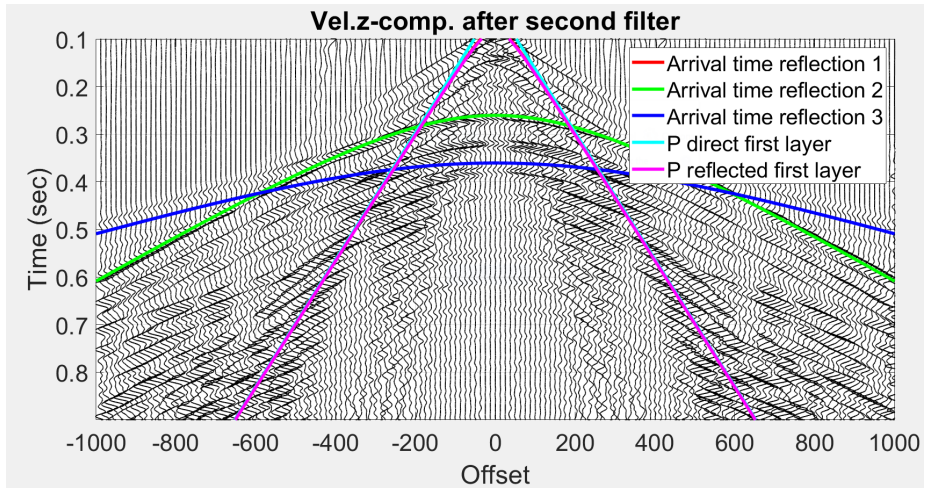


Figure 26: Second filter is applied to the shot panel of the three layer model for the z-component of particle velocity, which is done to filter out the direct wave. Figure 26a shows the panel before application of the second filter and the result after the first filter (identical to in figure 24c). Figure 26b shows the result of the filter is applied to both sides. Filter used: slopes=-0.0007,0.0005,0.0013,0.0025 amps=1.,0.,0.,1. perc=99.

26b the result of the filter to both sides is shown; although the second filter is smaller and takes away not too much information, the reflections do become better visible after the second filter. The plotting in MATLAB is done again with a time frame from $t=0.1$ -0.9 msec, which can be viewed in figure 27a; the plot with the arrival times on top of it can be viewed in figure 27b. From this plot it can be stated that theoretical arrival time for two reflection events aligns quite well with the reflections seen in the traces. This reflection from the bottom of the second layer, will be later used to study the limited broadside sensitivity.



(a)



(b)

Figure 27: Panel of the three layer model after application of the second filter in figure 27a. In figure 27b the same panel is plotted together with the expected arrival times. For both figures $sc=20$ and one in every 25 traces is plotted.

5.4 Determining of θ , correction factor and reversed correction factor

With the use of the output from the two point ray tracing, the horizontal slowness and the following relation: $\sin(\phi) = p \cdot Vp$, ϕ which is the angle with the vertical can be determined. For the limited broadside sensitivity analysis the angle with the horizontal is needed. Therefore the calculated angle ϕ (angle with the vertical) is transferred to the angle θ (angle with the horizontal). This can be done by subtracting ϕ of 90 degrees or calculating $\cos(\theta) = p \cdot Vp$. In figure 28 the angle θ is plotted against the distance for the three scenarios. The last step is to calculate the correction factor and the reversed correction factor: $\cos^2(\theta)/\sin(\theta)$ and $\sin(\theta)/\cos^2(\theta)$. Knowing the angle θ which can be done with the use of $\sin^2(\theta) + \cos^2(\theta) = 1$. The result of the $\cos^2(\theta)/\sin(\theta)$ versus the distance can be seen in figure 29. It can be seen that the factor increases with distance, $\cos^2(\theta)/\sin(\theta)$ increases faster when the depth of the reflector is smaller. So for the reflector at 20 m depth the $\cos^2(\theta)$ increases quickly. This will be later used for the simulation of what the DAS fibre would measure. In figure 30 the reversed correction factor is plotted, which shows an opposite relation compared to the correction factor: decreasing with offset. The reversed correction factor will be used to correct for the limited broadside sensitivity.

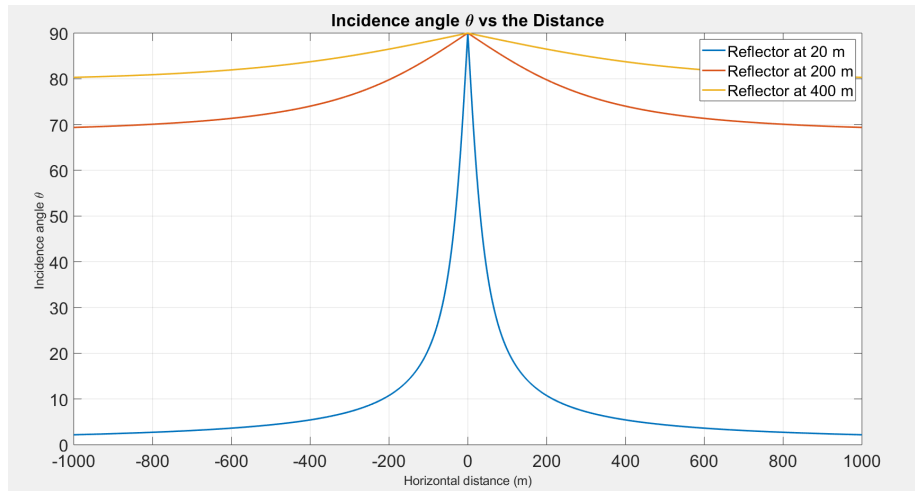


Figure 28: Plot of the theta (angle with the horizontal) versus offset for the three different scenarios.

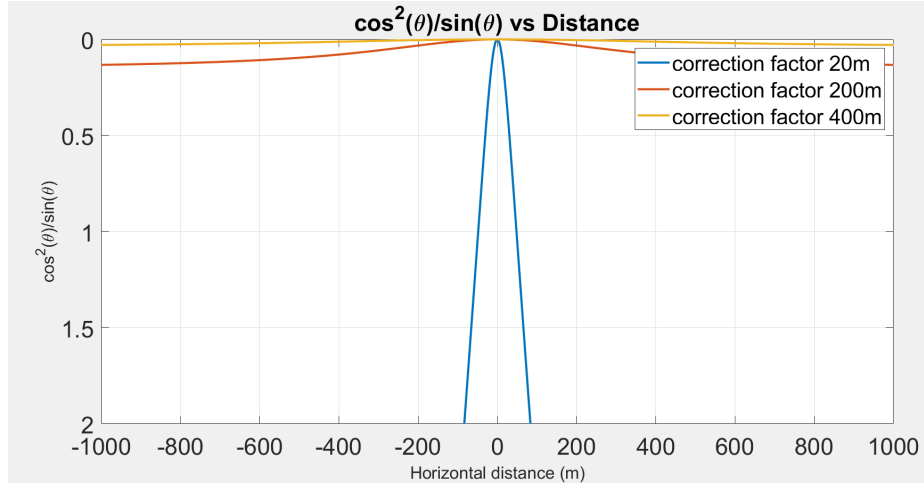


Figure 29: Plot of the $\cos^2(\theta)/\sin(\theta)$ factor versus offset: used to simulate what the DAS fibre would measure. The factor is close to zero at zero offset and increases for further offsets. For the first layer, the increasing goes considerably faster.

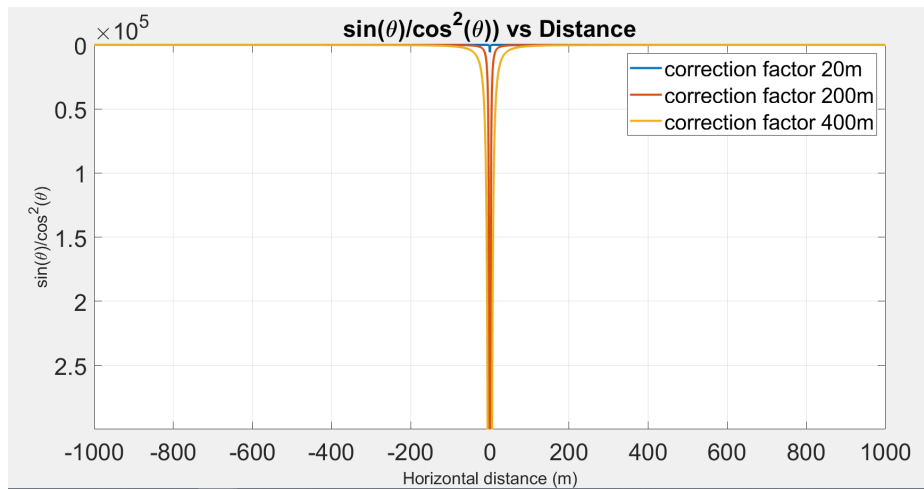


Figure 30: Plot of the $\sin(\theta)/\cos^2(\theta)$ factor versus offset: used to correct for the limited broadside sensitivity. Reversed plot of figure 29. Large values for zero offset and decreases for further offsets.

5.5 Limited broadside sensitivity

After the calculation of the correction and reversed correction factor, the next step is to pick the peak amplitudes of the P-wave reflection in order to select the P-wave reflection and use the correction factor. As has been shown earlier the theoretical arrival time aligns quite well with the peak-amplitude of the reflection. Therefore the ray arrival time can be used as a starting point to search for the peak amplitude (looking at the panels, shows that the peak amplitude of the P-wave reflection needed is negative). By searching and selecting the minimal amplitude an array of the P-wave reflection amplitude is created that can be corrected by the $\cos^2(\theta)/\sin(\theta)$, to simulate what the DAS fibre would measure in the model. This is first done for the two layer model and then it's done for the three layer model.

For selecting the peak amplitude, a code was written that searches for the minimum value within a certain time window with the arrival time from the ray tracing as a starting point. There are several options for how the peak amplitude can be selected correctly; the size of the time window can be variable but also the search window. The time window is the time span in which the peak amplitude can be searched. The search window is how the time window is applied, by either only looking at the arrival time plus the time span, only at the arrival time minus the time span or minus and plus the time span. Two tests were done to check how the minimum value can be best selected. One test was carried out where the time window is changed between 0.015, 0.01 and 0.005 seconds. The second test is done for one time window 0.005 seconds but different search windows, so the arrival time plus 0.005 seconds, the arrival time - 0.005 seconds and the arrival time +/- 0.005 seconds. For both the two layer and three layer model these two tests were done, to see how the peak amplitude can be selected correctly.

5.5.1 Picking peak amplitudes: two-layer model

In figure 31 the panel of the two layer model is plotted together with the arrival times. What comes across from this plot is that the theoretical arrival times don't quite align with the reflection visible in the plot for the further offsets. This happens for the arrival time that is a result from the ray tracing and from the theoretical arrival time, which can be seen in figure 32; it shows that these two arrival times do align with each other and there should be another explanation for the arrival times not aligning with the picked reflection peak from SPECFEM. Looking at the reflection, the phase of the reflection changes with further offsets. One explanation could be that the reflection of the P-wave interacts with the refraction of this P-wave, therefore the reflection doesn't align correctly with the arrival times. With this explanation in mind, it might be better to look only at the smaller offsets when selecting the peak amplitudes for this model, for $x=-500,+500$ m.

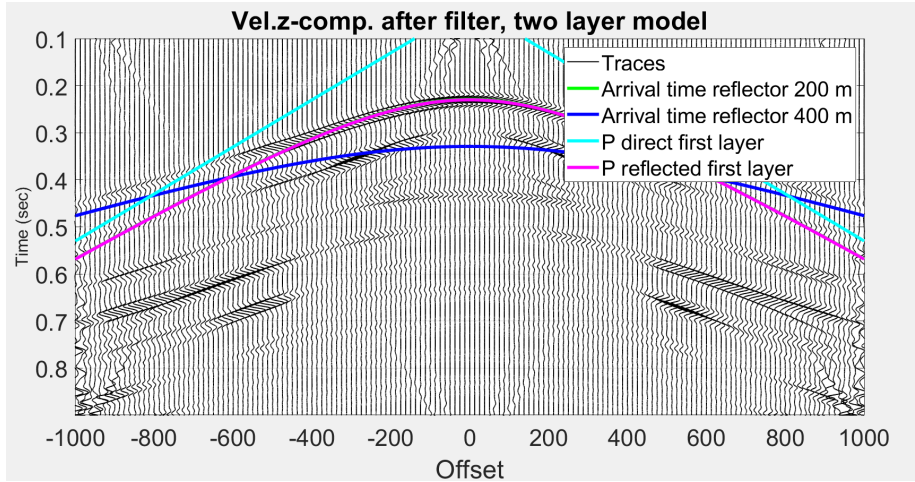


Figure 31: Shot panel for the two layer model after filtering, plotted on top of the traces are theoretical arrival times and arrival times achieved from the ray tracing.

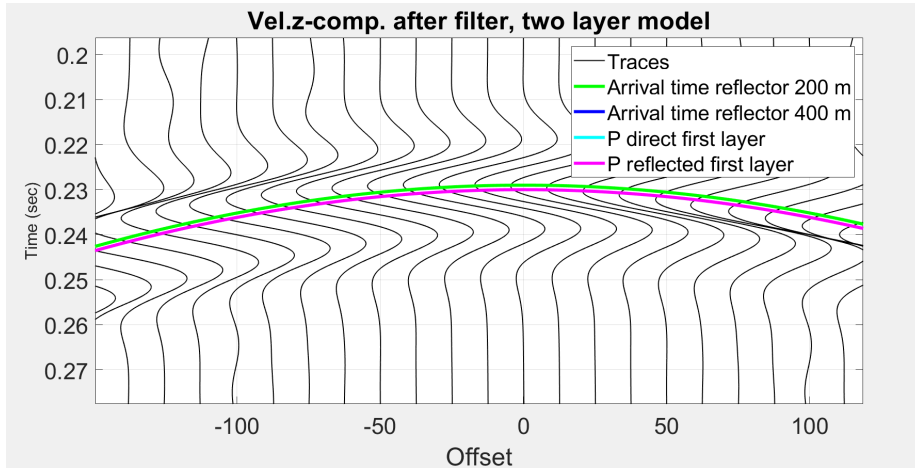


Figure 32: Zoom in on panel of the two layer model after filtering, plotted on top of the traces are theoretical arrival times and arrival times achieved from the ray tracing.

In figure 33 the result of the picked peak amplitudes can be viewed for the different search windows, in the two layer model. In figures 35 and 36 a zoom is made to see better where the amplitude picks are located. For small offsets it can be seen (figure 35) that the picks quite well align with the peak amplitude of the P-reflection. But for the further offsets (figure 36) they start to deviate from the true minimum, which also has to do with the arrival times starting to deviate from the true reflection peak. Looking at the amplitude picks, it looks like the peak amplitude with a search window of 0.005 selects the most correct amplitudes; the best match between the theoretical arrival time and peak amplitude. Therefore the next test is done for 0.005 but with different search windows. The result from this can be viewed in figure 34. From the zoom in plots for small offsets (figure 37) the search window +0.005 selects the amplitudes that align with the visible minima. For further offsets (figure 38) the scatters don't align anymore with the peak amplitudes. Therefore further plots only show the smaller offsets ($x=-500,+500$ m).

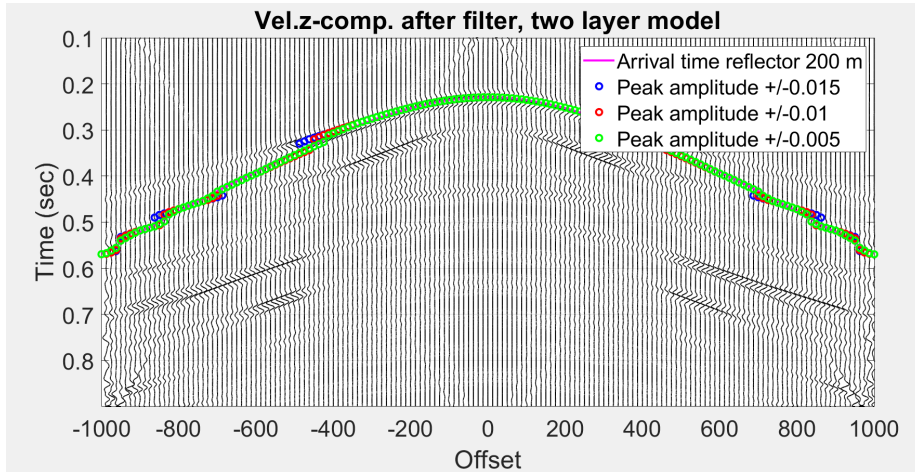


Figure 33: Shot panel for the two layer model after filtering (surface wave and direct wave are removed), on top of the panel are the amplitude picks plotted, searching for the negative peak amplitude for the P-wave reflection (different time windows are used).

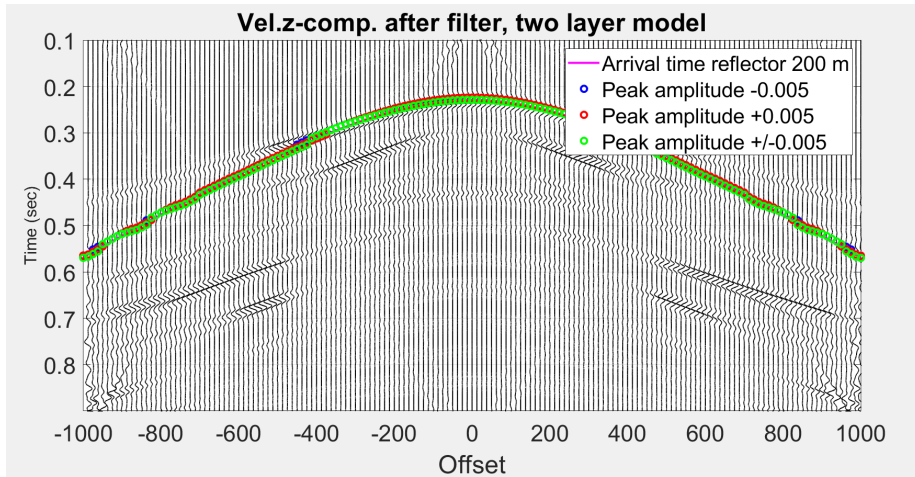


Figure 34: Panel of the two layer model after filtering (surface wave and direct wave are removed), on top of the panel are the amplitude picks plotted, searching for the negative peak amplitude for the P-wave reflection (same time window but different search windows are used).

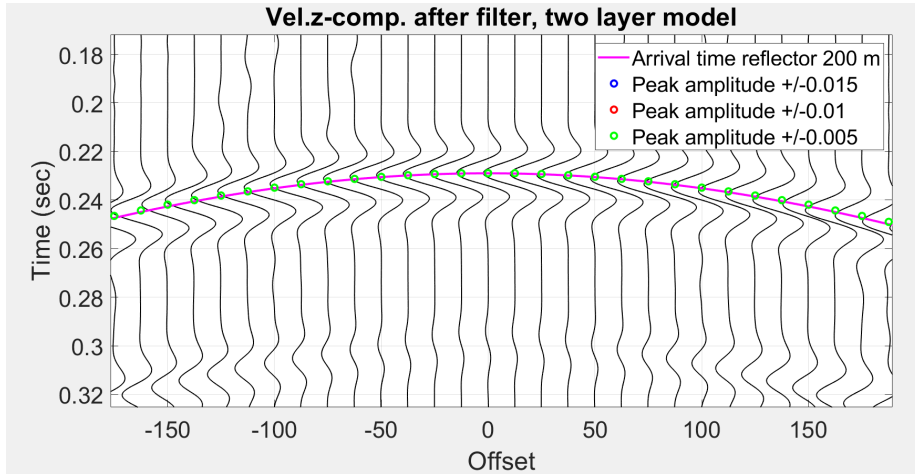


Figure 35: Shot panel detail for the two layer model after filtering (surface wave and direct wave are removed), on top of the panel are the amplitude picks plotted, searching for the negative peak amplitude for the P-wave reflection, different time windows are used. Zoom in on the middle of the panel.

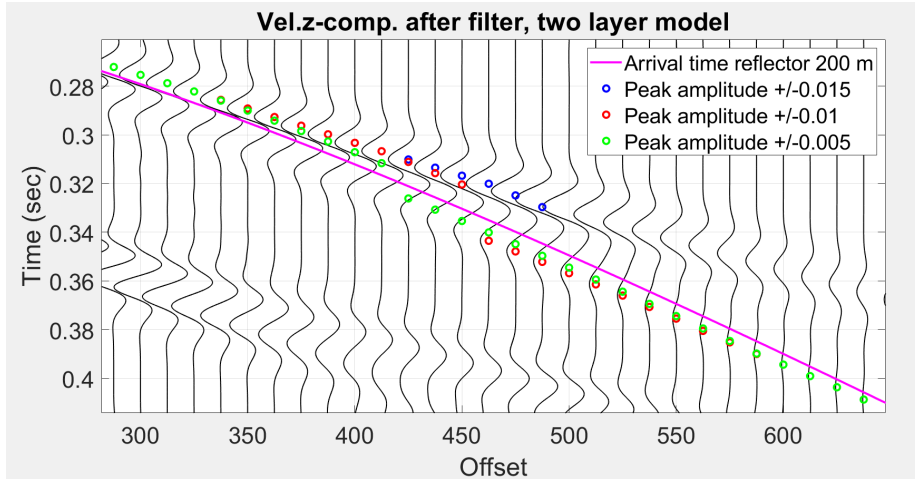


Figure 36: Shot panel detail for the two layer model after filtering (surface wave and direct wave are removed), on top of the panel are the amplitude picks plotted, searching for the negative peak amplitude for the P-wave reflection, different time windows are used. Zoom in on the side of the panel.

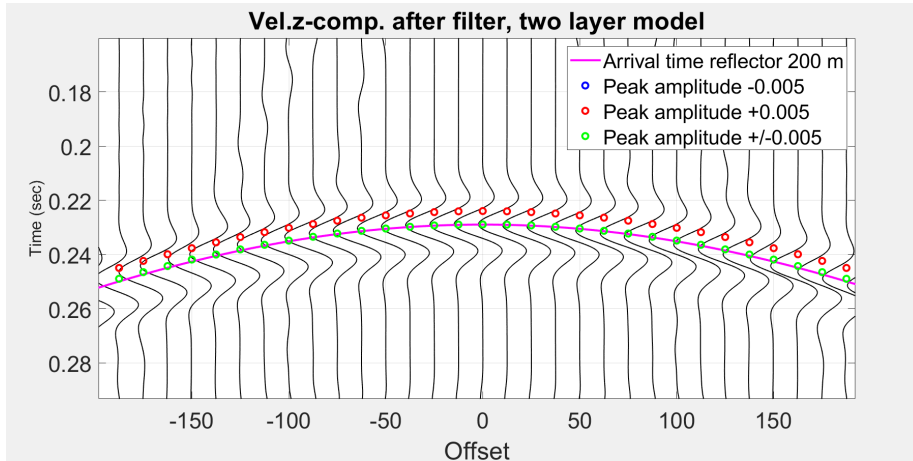


Figure 37: Shot panel detail for the two layer model after filtering (surface wave and direct wave are removed). On top of the panel are the amplitude picks plotted, searching for the negative peak amplitude for the P-wave reflection (same time window but different search windows are used). Zoom in on the middle of the panel.

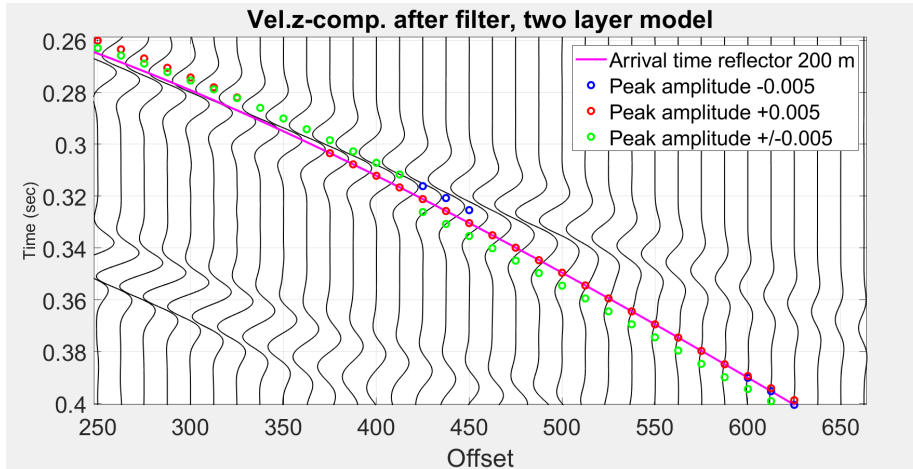


Figure 38: Shot panel detail for the two layer model after filtering (surface wave and direct wave are removed). On top of the panel are the amplitude picks plotted, searching for the negative peak amplitude for the P-wave reflection (same time window but different search windows are used). Zoom in on the side of the panel.

5.5.2 Simulation of DAS data and correction for limited broadside sensitivity: two-layer model

Next, the selected peak amplitudes are plotted against offset for the two different tests, which can be viewed in figure 39 (different time windows) and 40 (different search windows). The selected peak amplitudes decrease with offset, but from offset (-250 m, +250 m) the peak amplitudes are showing 'blobs' and not a linear decrease anymore as you would expect. But for the smaller offsets the amplitudes shows a nice linearly decreasing offset.

The selected amplitude peaks are now corrected with the $\cos^2(\theta)/\sin(\theta)$ factor; with this step is simulated what the DAS fibre would measure for this model. The result from this calculation is plotted against offset in figure 41 and 42. From these plots it can be seen that the simulated DAS data shows a small response for the smaller offset, because the waves enter the fibre with a large angle and due to limited broadside sensitivity the fibre doesn't capture this response well. Overall the amplitude measured by the DAS cable is smaller than the amplitude that the geophone would capture (figure 39 and 40).

The last step shows that the simulated DAS data can be corrected for this limited broadside sensitivity. This is done with the reversed correction factor $\sin(\theta)/\cos^2(\theta)$. With this step the measured amplitude from the DAS fibre is corrected for limited broadside sensitivity, as if the amplitude were measure by geophones (vertical component of the amplitude). The result is plotted against offset in figures 43 and 44. These plots show the exact same plot as in figure 39 and 40. So the factor $\sin(\theta)/\cos^2(\theta)$ is usable to correct for the limited broadside sensitivity in DAS data. And the processing of the two-layer model shows a good result, for simulating DAS data.

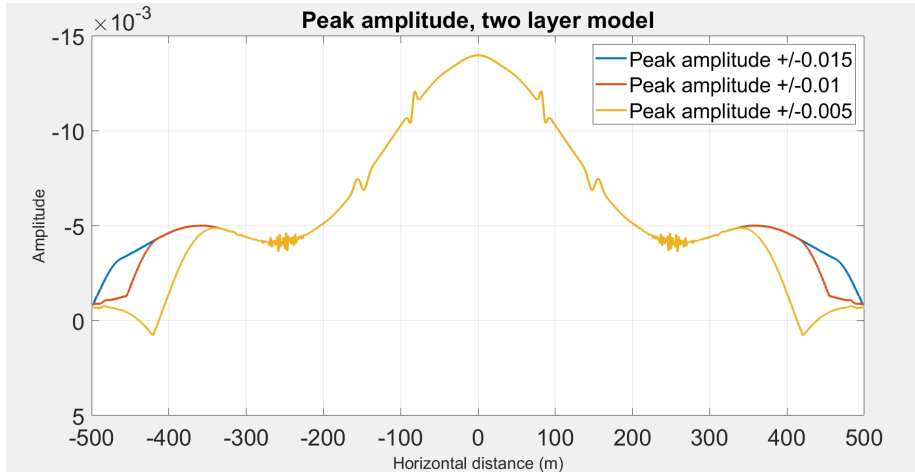


Figure 39: Plot of the negative peak amplitude of the second reflection event for the two layer model plotted against offset for the different time windows. Amplitude decreases with offset. Done for different time windows, 0,015, 0.01 and 0.005 seconds.

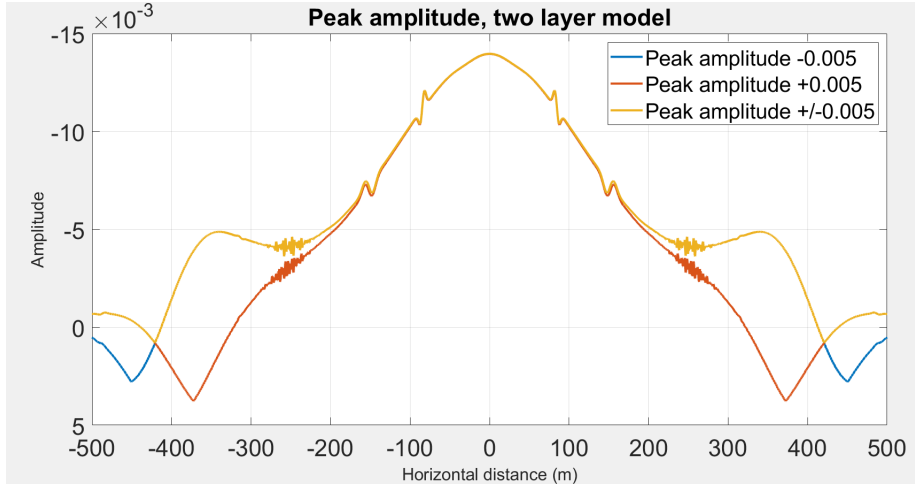


Figure 40: Plot of the peak amplitude of the second reflection event for the two layer model plotted against offset for the different search windows. Amplitude decreases with offset. Done for different search windows, +0.05, -0.05, and +/-0.05 seconds.

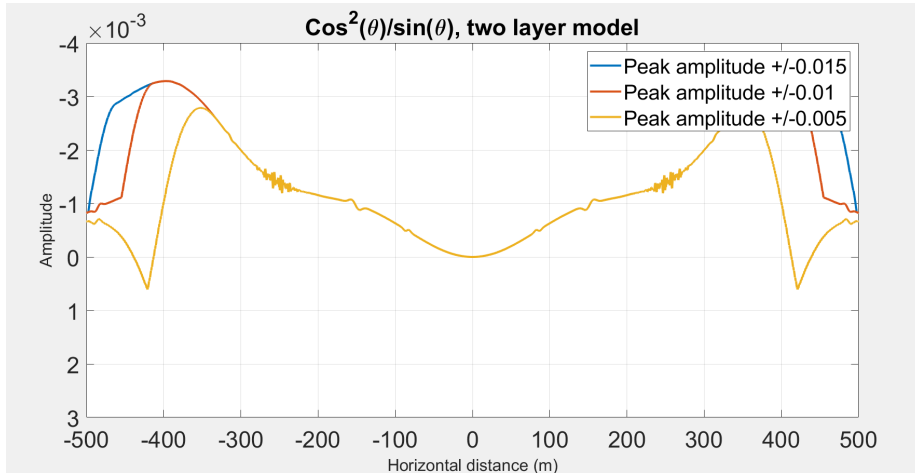


Figure 41: Plot of the negative peak amplitude of the second reflection event for the two layer model times $\cos^2(\theta)/\sin(\theta)$ versus offset, done for different time windows. With this step DAS data is simulated. Done for different time windows, 0,015, 0.01 and 0.005 seconds.

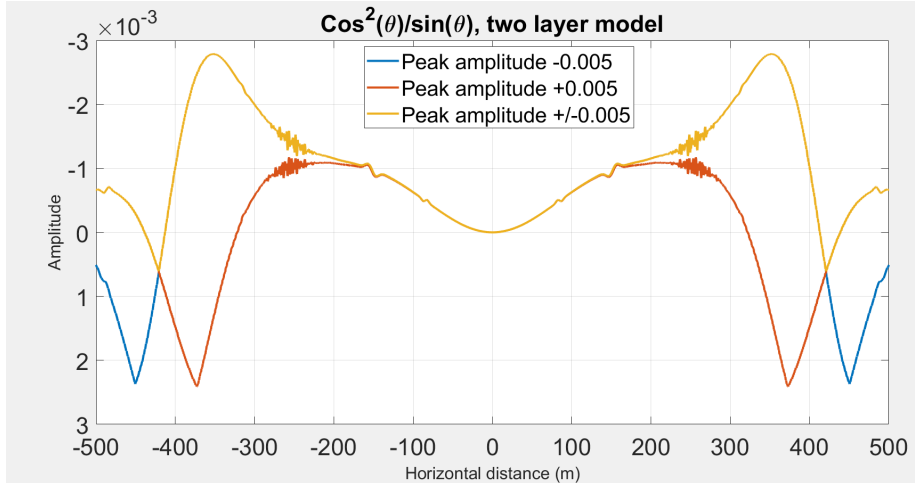


Figure 42: Plot of the negative peak amplitude of the second reflection event for the two layer model times $\cos^2(\theta)/\sin(\theta)$ versus offset, done for different search windows. With this step DAS data is simulated. Done for different search windows, +0.05, -0.05, and +/-0.05 seconds.

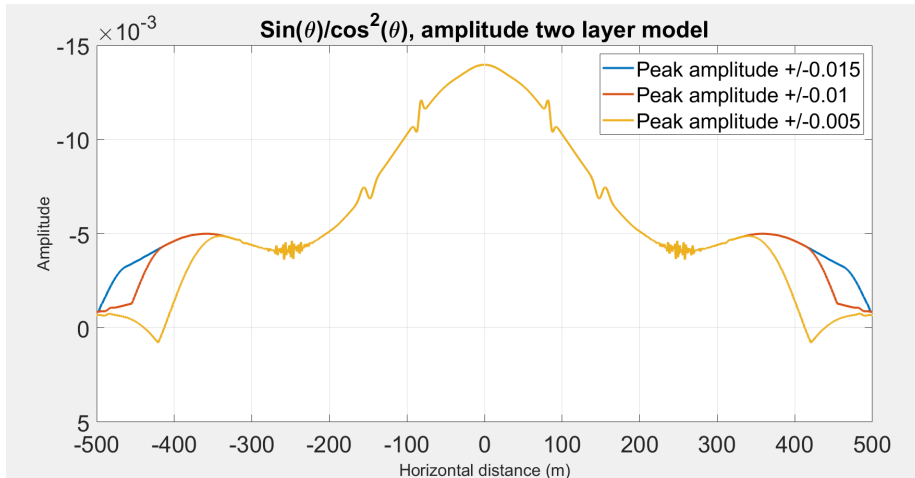


Figure 43: Plot of the simulated DAS data of the two layer model times $\sin(\theta)/\cos^2(\theta)$ versus offset, done for different time windows. In this plot is shown how simulated DAS reaction data can be corrected for the limited broadside sensitivity, such as if vertical geophones were recorded. Done for different time windows, 0,015, 0.01 and 0.005 seconds.

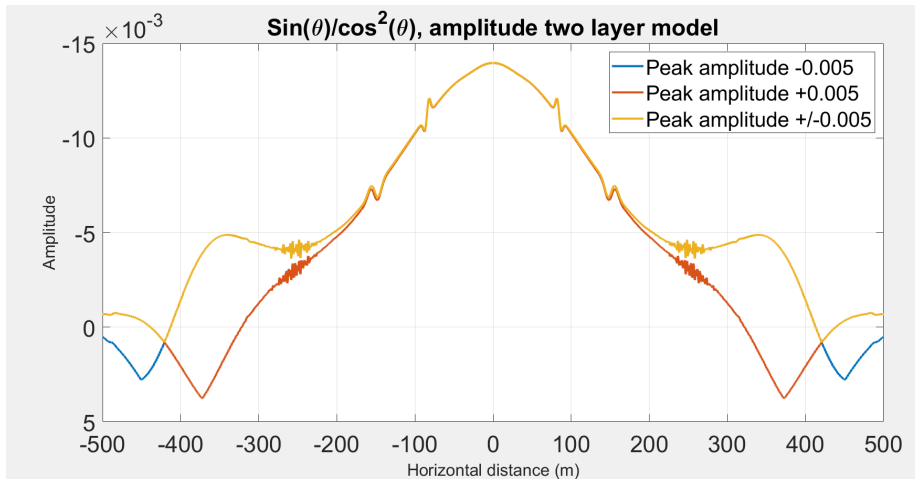


Figure 44: Plot of the simulated DAS data of the two layer model times $\sin(\theta)/\cos^2(\theta)$ versus offset, done for different search windows. In this plot is shown how simulated DAS reaction data can be corrected for the limited broadside sensitivity, such as if vertical geophones were recorded. Done for different search windows, +0.05, -0.05, and +/-0.05 seconds

5.5.3 Picking peak amplitudes: three-layer model

After studying the two layer model, the same steps are taken for the three layer model. In the three layer model the P-wave reflection, from the second layer at 200 m depth, in the panel is less clear than for the two layer model. This is due to increased interference with the remaining energy from the surface waves and interference with the other waves. The same two tests are done for the three layer model: First the test with the three different search windows, from which the result of selecting the peak amplitude can be viewed in figure 45. Zooming in to the smaller offsets (figure 47) shows that, the smaller time window, the scatter point picks are the closest to the true peak amplitude. For larger offsets the amplitude picks deviate more from the true minimum (figure 48). Since 0.005 shows the amplitude picks closest to the peak amplitude, the test for the different search windows is done with the time window of 0.005. The result from this can be viewed in figure 46. Zooming in to smaller offsets (figure 49) the search window of +0.005 shows the best fit to the peak amplitude. For larger offsets (figure 50) they deviate more from the true peak amplitude.

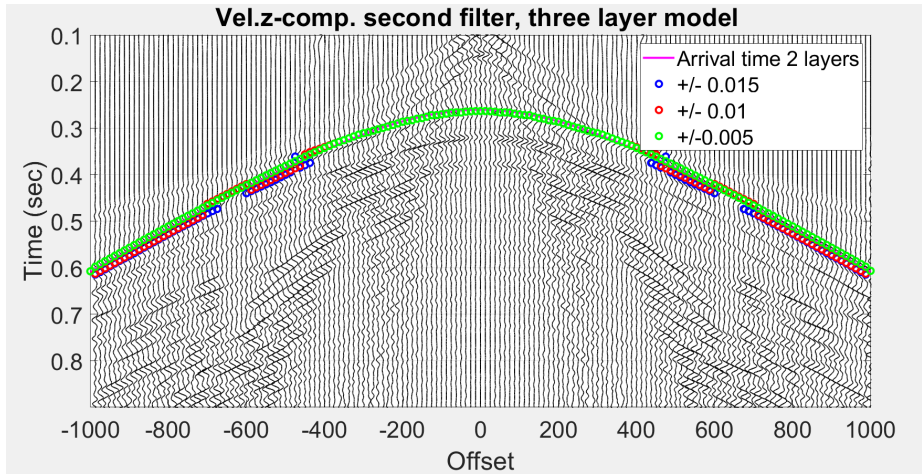


Figure 45: Shot panel for the three layer model after filtering (surface wave and direct wave are removed). On top of the panel are the amplitude picks plotted, after searching for the negative amplitude peak for the P-wave reflection; different time windows are tested.

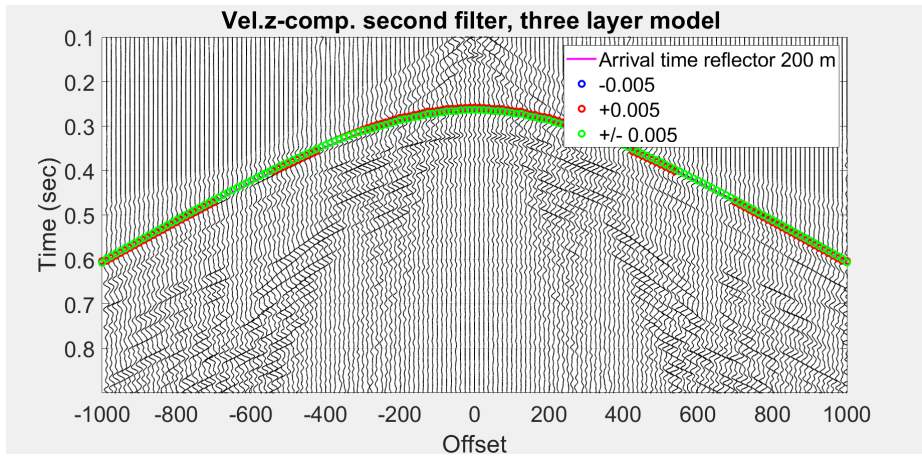


Figure 46: Shot panel for the three layer model after filtering (surface wave and direct wave are removed). On top of the panel are the amplitude picks plotted, after searching for the negative amplitude peak for the P-wave reflection; different search windows are tested.

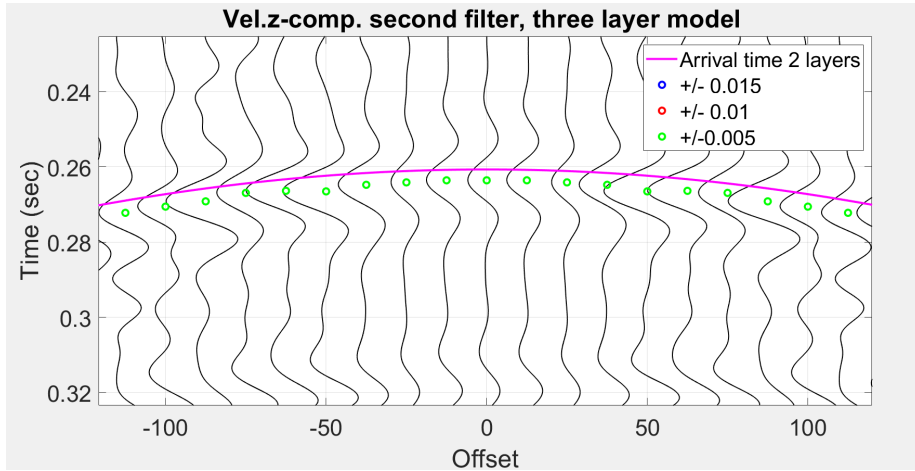


Figure 47: Shot panel for the three layer model after filtering (surface wave and direct wave are removed). On top of the panel are the amplitude picks plotted, after searching for the negative amplitude peak for the P-wave reflection; different time windows are tested. Zoom-in on the middle of the panel.

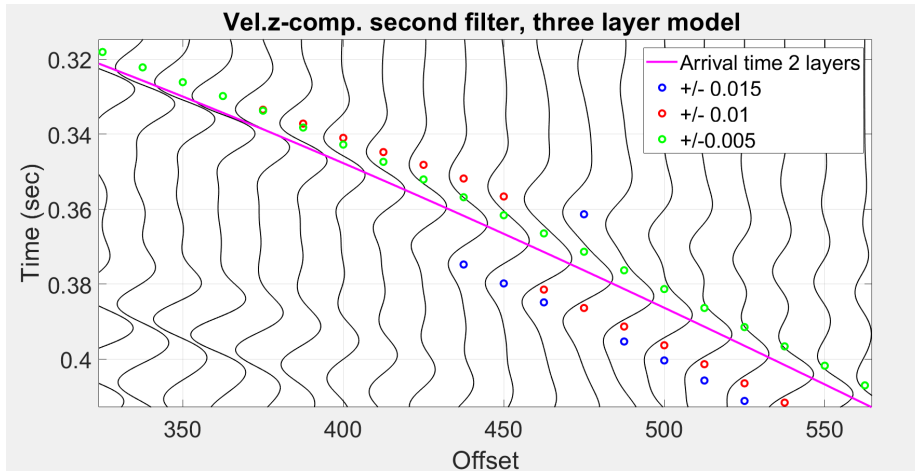


Figure 48: Shot panel for the three layer model after filtering (surface wave and direct wave are removed). On top of the panel are the amplitude picks plotted, after searching for the negative amplitude peak for the P-wave reflection; different time windows are tested. Zoom-in on the side of the panel.

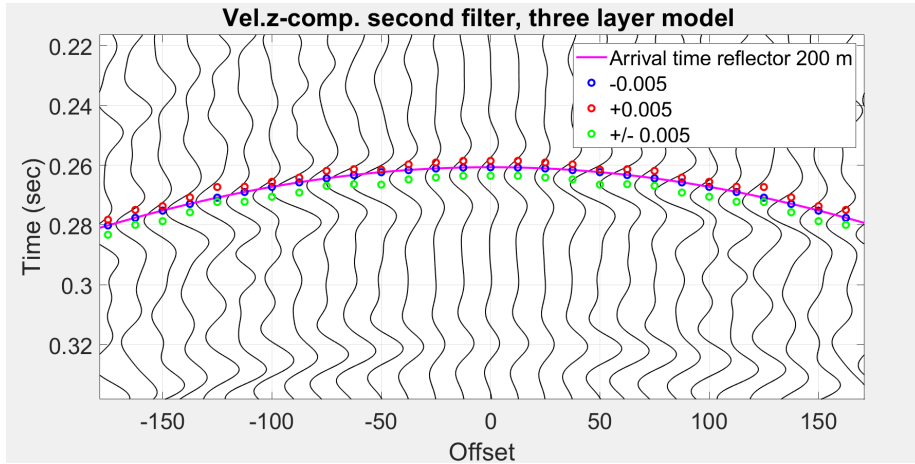


Figure 49: Shot panel for the three layer model after filtering (surface wave and direct wave are removed). On top of the panel are the amplitude picks plotted, after searching for the negative amplitude peak for the P-wave reflection; different search windows are tested. Zoom-in on the middle of the panel.

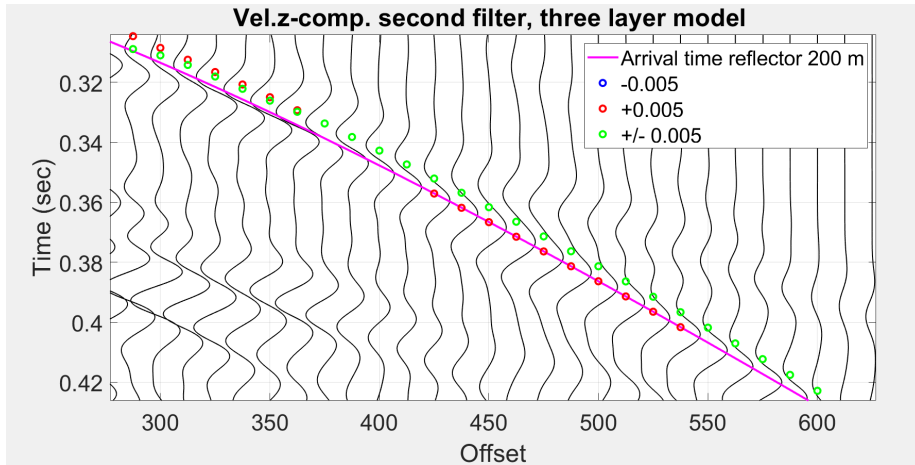


Figure 50: Shot panel for the three layer model after filtering (surface wave and direct wave are removed). On top of the panel are the amplitude picks plotted, after searching for the negative amplitude peak for the P-wave reflection; different search windows are tested. Zoom-in on the side of the panel.

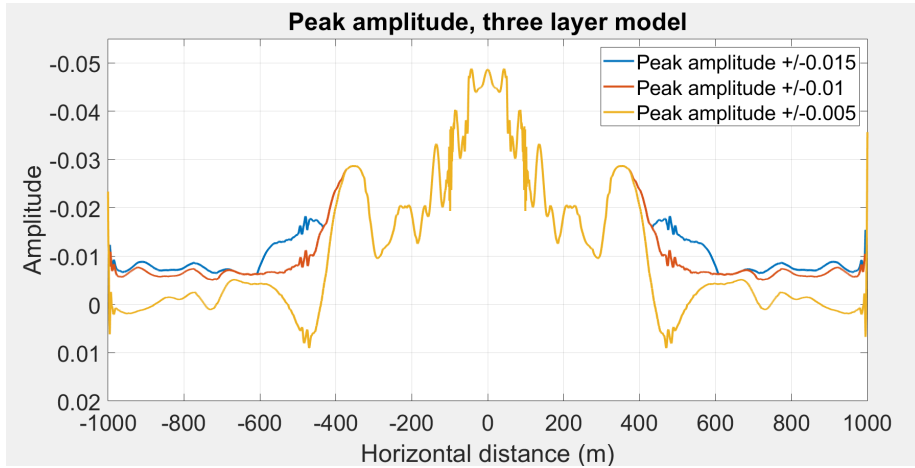


Figure 51: Plot of the peak amplitude of the three layer model plotted against offset for the different time windows. Overall trend shows a decreasing amplitude with offset.

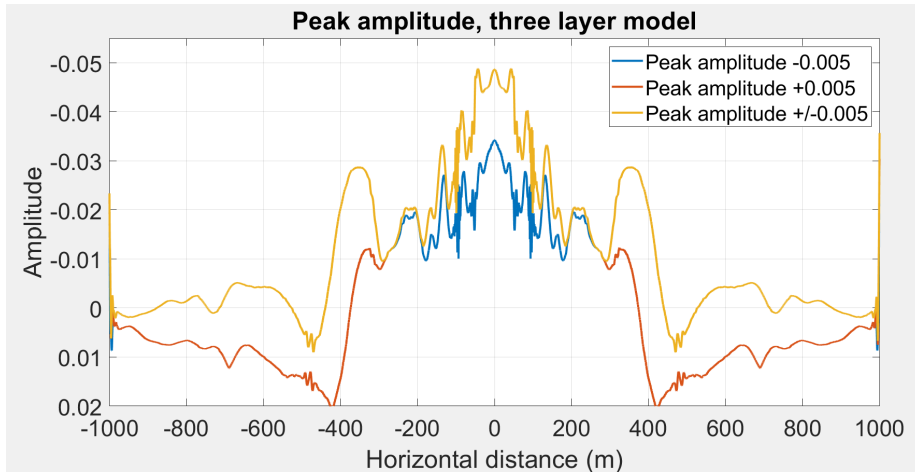


Figure 52: Plot of the peak amplitude of the three layer model plotted against offset for the different search windows. Overall trend shows a decreasing amplitude with offset.

5.5.4 Simulation of DAS data and correction for limited broadside sensitivity: three-layer model

The peak amplitude is plotted against offset, which can be viewed in figures 51 and 52. These plots show that the peak amplitude for the three layer model does not decrease as smoothly with offset as the two layer model. Which can be explained by the fact that the three layer model has more interference with different waves and needed more filtering, which all has effect on the amplitude of the P-wave reflection. Also for smaller offsets, the amplitude deviates from linear decreasing in amplitude with increasing offset: the amplitude variation with offset exhibits discontinuities.

For the selected peak amplitude, the correction factor $\cos^2(\theta)/\sin(\theta)$ is used to simulate DAS data, and calculate the response that the DAS fibre would approximately measure. amplitude that the DAS fibre would measure. The results can be viewed in figures 53 (different time windows) and 54 (different search windows). These plots show a smaller amplitude at smaller offsets, almost equal to zero, which is expected for DAS data. What should be noticed is that the amplitude for DAS is one order of magnitude smaller than the amplitude from the geophones. So it shows that the overall amplitude is quite small, but especially for smaller offsets the amplitude is close to zero. Since the peak amplitude is not selected correctly everywhere the simulated DAS data may deviate from the correct value too.

The last step is the use of the reversed correction factor $\sin(\theta)/\cos^2(\theta)$, to check if this factor can be used to correct for limited broadside sensitivity in DAS data. With this step the simulated DAS data is corrected for limited broadside sensitivity and is transferred as if it was measure by geophones (vertical component of the amplitude). The result in figure 55 and 56 shows the exact result as in figure 51 and 52, which means the factor can be used to correct for limited broadside sensitivity in DAS data. To make these plots more realistic, noise should be added to the data and the data should be stacked.

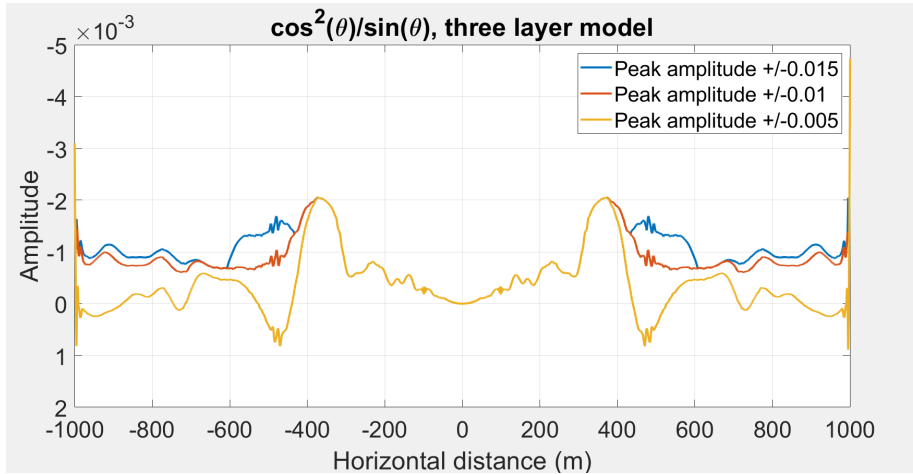


Figure 53: Plot of the peak amplitude of the three layer model times $\cos^2(\theta)/\sin(\theta)$ versus offset, done for different time windows. With this step DAS data is simulated.

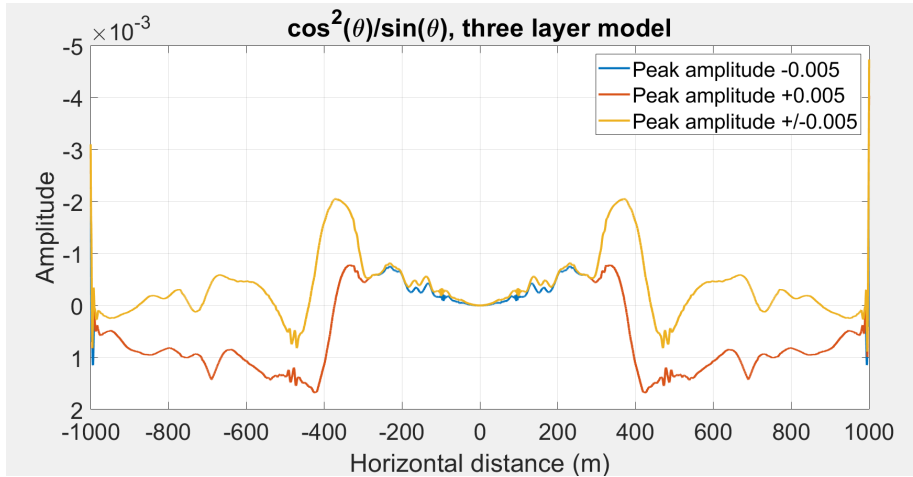


Figure 54: Plot of the peak amplitude of the three layer model times $\cos^2(\theta)/\sin(\theta)$ versus offset, done for different search windows. With this step DAS data is simulated.

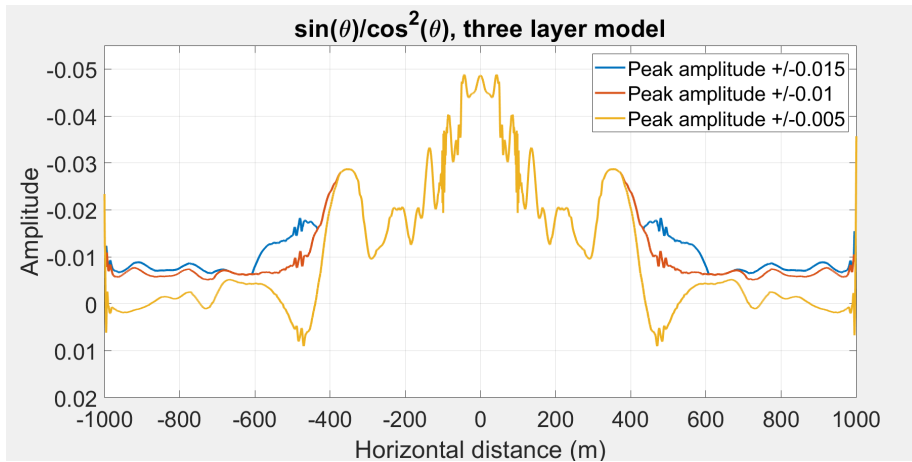


Figure 55: Plot of the simulated DAS data of the three layer model times $\sin(\theta)/\cos^2(\theta)$ versus offset, done for different time windows. In this plot is shown how simulated DAS reaction data can be corrected for the limited broadside sensitivity, such as if vertical geophones were recorded.

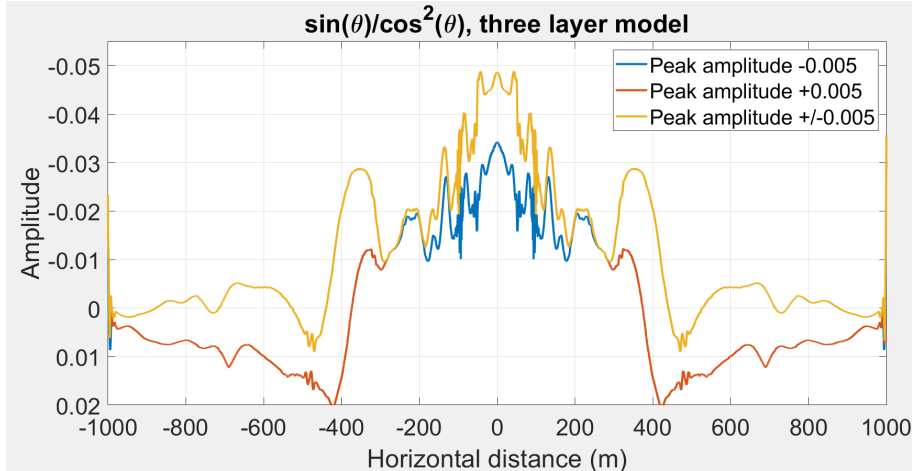


Figure 56: Plot of the simulated DAS data of the three layer model times $\sin(\theta)/\cos^2(\theta)$ versus offset, done for different search windows. In this plot is shown how simulated DAS reaction data can be corrected for the limited broadside sensitivity, such as if vertical geophones were recorded.

5.6 Suggestion for conversion of particle velocity to strain

As is suggested in the workflow (figure 6) one of the last steps is to transfer the particle velocity data to strain data. It is not straightforward how this conversion works, but it is an important part in understanding DAS data. It is beyond the scope of this thesis to do the translation of the data, but some suggestions from the literature are discussed here. The following descriptions are entirely based on publications that are here referred to. Three brief descriptions are provided here.

Jreij et al. (2017) compared surface horizontal DAS data to geophones. To make a proper comparison, the conversion of particle velocity to strain was made, with the use of the following equations.

$$\frac{d}{dt} \left(\frac{du}{dz} \right) = \frac{d}{dz} \left(\frac{du}{dt} \right) = \dot{\epsilon} \quad (16)$$

$$u = c \int_0^t \dot{\epsilon} dt \quad (17)$$

$$\frac{-c}{\cos(\alpha)} \frac{du}{dx} = \frac{du}{dt} \quad (18)$$

For the DAS cable, the distance along the cable is taken to be x and the recording time is t , which gives the displacement along the fibre to be $u(x, t)$. Which gives equation 16 as an estimate of the fibre strain rate ($\dot{\epsilon}$). Knowing the strain rate Jreij et al. (2017) stated that the conversion from strain rate to displacement takes an integration with respect to time together with a multiplication by the propagation speed (c), stated in equation 17. With this equation, the comparison between a geophone measurement and a DAS fibre can be made, which provides an apparent phase difference. Another relationship is established between strain and displacement which depends on the angle (α), the angle between the direction of propagation of waves and fibres and the phase velocity (c) of the waves (equation 18).

Assumed is that every wave arrives at a constant angle and that the phase velocity is equal to the particle velocity within the fibre.

Another suggestion for the translation from particle velocity to strain was made in Jousset et al. (2018). The phase difference measured in the DAS-system is determined by the relative travel time and the relative distance. The gauge length (dX) is the physical distance over which the phase difference is measured. The measured phase changes are directly related to the distance changes in the gauge length and therefore the strain rate in the direction of the fibre can be recorded. $u(x, t)$ represents the dynamic replacement of the fibre the DAS observation at axial location x and time t , is a measure of the strain rate at the

distance from the recorded location and given in equation 19.

$$\text{DAS}(x, t) = \left[u \left(x + \frac{dx}{2}, t \right) - u \left(x - \frac{dx}{2}, t \right) \right] - \left[u \left(x + \frac{dx}{2}, t - dt \right) - u \left(x - \frac{dx}{2}, t - dt \right) \right] \quad (19)$$

DAS data can provide an estimate of the fibre strain rate (equation 20) or of the spatial derivative of particle velocity (equation 21). Integration equation 20 with respect to time, local strain can be determined along the fibre. And if the local strain is integrated again with respect to space the relative displacement can be determined along the fibre.

$$\frac{\partial}{\partial t} \left(\frac{\partial u}{\partial x} \right) \quad (20)$$

$$\frac{\partial}{\partial x} \left(\frac{\partial u}{\partial t} \right) \quad (21)$$

A different approach is evaluated in Correa et al. (2017) to convert DAS data to particle velocity which is measured by geophones. Another advantage from converting DAS data to particle velocity is that existing processing steps used for particle velocity can also be applied to the DAS data after the conversion to particle velocity. It is stated that strain can be approximated with equation 22. Where u is the displacement along the fibre, G is the gauge length, L is the pulse width and $w(l)$ is the function that defines the laser pulse shape. The approach used to convert strain rate to particle velocity is to integrate the data along the cable length. In the earlier examples a time integration was used, using the local propagation velocity of seismic waves, which requires knowledge of the seismic velocities. In Correa et al. (2017) the conversion to particle velocity is derived from equation 22, where a plane wave $Ae^{-i(\omega t - kx)}$ describes the displacement u . A is the maximum amplitude, ω angular velocity, t time, k is the wave number and x is the distance. The DAS response is stated in equation 23 and the response of the geophone in equation 24. So converting the strain rate to particle velocity is the ratio of equation 23 and equation 24, which results in equation 25. Equation 25 can be seen as a filter to process the strain data. Suggested is to add a small parameter to regularise the filter and avoid divisions by zero (26).

$$\frac{d}{dt} \int_L (u(z - G/2 + l, t) - u(z + G/2 + l, t)) w(l) dl \quad (22)$$

$$A_z e^{-i(\omega t - k_z z)} \frac{\omega}{k_z} (e^{ik_z L/2} - e^{-ik_z L/2}) (e^{ik_z G/2} - e^{-ik_z G/2}) \quad (23)$$

$$-i_z e^{-i(\omega t - k_z z)} \quad (24)$$

$$\frac{ik_z}{4 \sin(k_z L/2) \sin(k_z G/2)} \quad (25)$$

$$-\frac{1}{ik_z LG} \quad (26)$$

6 Discussion

In this chapter the results from the previous chapters are discussed. First the method and programs used are discussed: SPECSEM and the two-point ray tracing. Then the results from the slope filter and the correction factor for the limited broadside sensitivity are discussed, and last suggestions for further research are done.

6.1 SPECSEM wave propagation and the model building

SPECSEM is an excellent program to model DAS configurations, although SPECSEM has the limitation that you can not directly compute strain. During the process of building the model some difficulties came across that could use some more research, like certain parameters or the use of different sources in an elastic or acoustic model.

The runs and model building were all done in SPECSEM2D, but modelling wave propagation in a 2D environment is a simplification, since a wave in reality doesn't travel in 2D in the subsurface. In the SPECSEM manual (Komatitsch and Vilotte, 2018) is stated that the sources used are line sources, which means that the spreading from the source is cylindrical spreading. Further simulations would be better to model in 3D, where a point source is used and spherical spreading is computed. Another option would be to correct from the cylindrical spreading to spherical spreading for the SPECSEM2D runs. For the understanding of SPECSEM it is preferred to start modelling with the SPECSEM2D version first before modelling in SPECSEM3D. Eventually for the two-layer and three-layer model SPECSEM2D was sufficient enough to model the surface seismic DAS configuration and research the limited broadside sensitivity.

6.2 Two point ray tracing

The CREWES toolbox was an useful tool for the ray tracing. Just by defining the velocity model and the source- and receivers coordinates, the ray tracing can determine the arrival time and horizontal slowness. The horizontal slowness is a fundamental parameter for determining incidence angle θ and $\cos^2(\theta)/\sin(\theta)$. Without this toolbox it would be hard to determine the incidence angle, which is needed for the correction factor and reversed correction factor. A small drawback of the ray tracing tool is the limitation that only positive offsets can be computed. Which is solved by swapping the travel time and horizontal slowness to the negative offset to also get the negative values for model used, with offsets ranging from $x=-1000$ m to $x=+1000$ m. Another drawback is that only horizontal reflectors can be implemented. For a more realistic model a different tool could be used, or CREWES can be used as a starting tool.

6.3 Surface waves

Filtering out the surface waves was done with the help of Seismic Unix. It turned out that filtering out the surface waves is not as straightforward as it seems. Aliasing occurs when the slope filter is applied, but by extending the slope filter, too much information (other waves besides only the surface waves) is taken out. The surface waves propagate through a shallow layer with a low velocity and the removal of waves is never perfect. The risk with removal of waves is that other waves can be affected as well. Nevertheless after filtering out the surface waves, it was managed to get a clearer view of the P-wave reflection at 200 m depth.

For proper sampling (and removal) of the surface waves, the suggestion is made that a receiver spacing of 0.5 m is preferred over 1 m for the considered model properties, due to aliasing occurring with a receiver spacing of 1 m. It turns out that a receiver spacing of 0.5 m results in a better sampling of the traces and more precise filters can be designed to filter out the surface waves since the filter has a smaller slope value and therefore the filter values can be chosen more precise.

One question that arises is, what causes the aliasing in the shot panels after applying the slope filter? One suggestion is that the aliasing is caused by applying the slope filter and instead it might be better to apply an fk-filter. The fk-filter is applied in the frequency, wavenumber domain, which would prevent from aliasing to happen. But for the shot panels in this thesis the slope filter seemed adequate enough, since the interest was with the P-wave reflections at 200 m depth. One of the important equations for spatial aliasing is $\Delta x \leq \frac{V_{min}}{2 \cdot f_{max}}$, which is also discussed in Vermeer (1990). This relation states, that the spatial distance should be equal or smaller than the minimum velocity divided by two times the maximum frequency. Where two times the maximum frequency represents two data points per wave length, should be enough to sample the wave. Calculating this for the three layer model is done in equation 27. Which suggests that for a receiver spacing below 2.75 m no aliasing should occur. But the shot panels do show aliasing after the filter is applied, especially for the three layer model this seems inevitable. One explanation could be that the aliasing criteria is the minimum amount of data points needed to reconstruct wavefronts in the shot panels. But when detailed information of the phase changes are researched, more data points per wavelength are preferred for sampling the wavelength correct. Therefore the unprocessed shot panel doesn't show aliasing, but when the slope filter is applied, aliasing occurs in the panel. Which makes it harder to later pick the right peak amplitudes.

$$\begin{aligned} \Delta x &\leq \frac{V_{min}}{2 \cdot f_{max}} \\ \Delta x &\leq \frac{440}{2 \cdot 80} \\ \Delta x &\leq 2.75m \end{aligned} \tag{27}$$

Furthermore there was also a second filter applied to the three-layer shot panel. This was just a small filter, to filter out the direct wave from the top layer. The difference after the second filter is only small compared to the shot panel before the second filter. But looking at the P-wave reflection at 200 m depth, this reflection does become more clearer after the second filter. So the result might not be big from the second filter, but it does help in getting a clear P-wave reflection.

6.4 Limited broadside sensitivity

By filtering out the surface waves the P-wave reflection at 200 m shows up quite consistent across the panel. For this reflection the peak amplitude for each trace is selected. Two different tests were done to check how the peak amplitude can be selected best. For the smaller offsets ($x=-500,+500$ m) in the two layer model this results in clear decreasing amplitude with offset like expected. For the larger offsets for the two-layer model the picked amplitudes did not align with the reflection, which can be explained by the P-wave reflection being transformed in a refraction for further offsets. For the three layer model the amplitude variation with offset exhibits discontinuities, this happens for smaller as well as larger offsets: the overall trend is still a decreasing amplitude with offset. The non-linear trend could be explained by that the phase of the wave is also changing along the offset, which makes it not as straightforward as picking the peak amplitude to select the reflection, because for some traces the peak amplitude isn't that clear anymore. Another explanation could be that there is still some energy left of the surface waves that interacts with the reflection, or maybe too much surface wave energy is filtered out, so the amplitude of the reflection is also filtered out. To be able to better pick the peak amplitude of the reflection, a more advance picker should be designed or a different method to select the reflection should be chosen.

Applying the $\cos^2(\theta)/\sin(\theta)$ factor to simulate what the DAS fibre would measure for these models, is giving the outcome as expected; with a small amplitude for the small offsets due to the waves arriving with large angle. Applying the reversed factor $\sin(\theta)/\cos^2(\theta)$, is transferring the DAS amplitude as if it was measured by geophone (Vertical component from the simulated DAS data). This step shows the same response as the peak amplitude selected from the panels, as the correction factor is regular for all angles and therefore can be converted for the complete offset range. This suggests that for these models the correction factor can be used to simulate DAS data and the reversed correction factor can be used for DAS data to correct for the limited broadside sensitivity.

The two layer model gave a nice clear outcome of the peak amplitude that was closer to what was expected than the three layer model. This might have to do with that the three layer model includes more waves that all interact with each other. Therefore more filtering is needed to get a good P-wave reflection. It can be stated that adding a small weathering layer to the model complicates the

model, by introducing strong surface multiples. But the two layer does show a clear plot for the peak amplitudes. With one downside that the amplitude picker worked only for the offsets between $x=-500,+500$ m, but for this model the broadside waves entered the fibre for the smaller offsets. So the two-layer model does shows nicely how the peak amplitudes can be picked and be used to simulate the DAS data and then correct for the limited broadside sensitivity. The two-layer model also shows a much clearer result, with linear plots for the peak amplitude, DAS simulation and correction for the limited broadside sensitivity compared to the three-layer model.

Something that could be improved is the peak amplitude picker: across the panel not for the correct peak amplitude was picker for each trace. Improving this picker might also improve the results of simulation of the DAS data and correction for DAS data. Furthermore a correction for cylindrical spreading could be added to get a more realistic simulation of the DAS data.

Another suggestion for further research would be to add noise to the simulated DAS data and then stack the DAS data, in order to get a more realistic amplitude plot. Further suggestions are to model in SPEC-FEM3D or to correct for the cylindrical spreading that SPEC-FEM2D uses. A better amplitude picker could be designed and the fk-filter could be used instead of the slope filter. The next important step is to transfer particle velocity to strain, with the suggestions from literature here in mind, to simulate realistic synthetic DAS data. Then other parameters as the gauge length and signal to noise ratio should be researched. This in order to be able to compare the synthetic DAS data to synthetic particle velocity and real DAS data.

7 Conclusion

With the main question in mind: *Can reflection information from Distributed Acoustic Sensing be improved for broadside P-waves, in a surface seismic configuration?* the following can be stated.

This thesis shows how SPEC-FEM can be used to simulate particle velocity data, from which is calculated what the DAS fibre would measure, which is done successfully. Although for further research it is suggested to model with SPEC-FEM3D. From the modelled shot panel data, the traces were plotted and surface waves were filtered out. From the filtering it can be stated that for the configurations used in this thesis a receiver spacing of 0.5 m is better to prevent from spatial aliasing of surface waves while filtering. Or to use an fk-filter instead of a slope filter. It was also suggested that for the three layer model it was best to design a second filter in order to filter out the direct wave too. After the filter is applied the P-wave reflection at a depth of 200 m appears quite clear across the panel.

Parallel to filtering out the surface waves, the ray-tracing tool from CREWES was used. Which turned out to be a useful tool to simulate the ray connecting source and receiver with the according models. The limitation of this tool is that there can only be vertical velocity variations and only positive offsets.

With the P-wave reflection appearing in the panel, the peak amplitude is selected with an amplitude picker. This selected peak amplitude is then corrected with the $\cos^2(\theta)/\sin(\theta)$ factor in order to simulate DAS data. The peak amplitude picker doesn't work optimal, and doesn't always pick the correct peak amplitude; for further research this would need more attention. But applying the correction factor gives the results that is expected from DAS data with a small peak amplitude value for smaller offsets due to P-waves entering the fibre with a large angle. Using the reversed correction factor, the DAS data can be corrected for this limited broadside sensitivity and amplitudes appear as if they were measured by geophones. But it also turns out that adding more reflections to the model, the model gets more complicated rather quickly and therefore it will get harder to select the correct peak amplitude.

So the reflection information can be improved for DAS data by correctly filtering out the surface wave to get a clear reflection. The correction factor can be used to simulate what the DAS fibre would measure and the reversed correction factor can successfully be used to correct for the limited broadside sensitivity and compute the amplitudes as if they were measured by geophones. Especially for the two-layer model for offsets between $x=-250,+250$ m the DAS fibre measurements are equal to geophone data (or even better in future models, due to higher spatial sampling).

This thesis presents a method to correct for the broadside sensitivity of DAS,

which helps in increasing the applicability of DAS for many applications.

8 Acknowledgements

I would like to thank my supervisors Arie Verdel and Bob Paap from TNO for supervising me on a weekly basis and the opportunity to write my thesis at TNO, and Hanneke Paulssen as my second supervisor from the Utrecht University. Further I would like to thank Vincent Vandeweijer for helping me with Seismic Unix.

References

- Cohen, J. K. and Stockwell, J. J. W. *CWP/SU: Seismic Unix, a free package for seismic research and processing*.
- Correa, J., Egorov, A., Tertyshnikov, K., Bona, A., Pevzner, R., Dean, T., Freifeld, B., and Marshall, S. (2017). Analysis of signal to noise and directivity characteristics of das vsp at near and far offsets—a co2crc otway project data example. *The Leading Edge*, 36(12):994a1–994a7.
- Daley, T., Miller, D., Dodds, K., Cook, P., and Freifeld, B. (2016). Field testing of modular borehole monitoring with simultaneous distributed acoustic sensing and geophone vertical seismic profiles at citronelle, alabama. *Geophysical Prospecting*, 64(5):1318–1334.
- Jousset, P., Reinsch, T., Ryberg, T., Blanck, H., Clarke, A., Aghayev, R., Hersir, G. P., Hennings, J., Weber, M., and Krawczyk, C. M. (2018). Dynamic strain determination using fibre-optic cables allows imaging of seismological and structural features. *Nature communications*, 9(1):2509.
- Jreij, S., Trainor-Guitton, W., and Miller, D. (2017). Field data comparison of 3d horizontal distributed acoustic sensing and geophones. In *SEG Technical Program Expanded Abstracts 2017*, pages 1–6. Society of Exploration Geophysicists.
- Komatitsch, D. and Tromp, J. (1999). Introduction to the spectral element method for three-dimensional seismic wave propagation. *Geophysical journal international*, 139(3):806–822.
- Komatitsch, D. and Vilotte, J.-P. (1998). The spectral element method: an efficient tool to simulate the seismic response of 2d and 3d geological structures. *Bulletin of the seismological society of America*, 88(2):368–392.
- Komatitsch, D. and Vilotte, J.-P. (2018). *Specfem2d user manual*.
- Kuvshinov, B. (2016). Interaction of helically wound fibre-optic cables with plane seismic waves. *Geophysical Prospecting*, 64(3):671–688.
- Lumens, P. G. E. (2014). Fibre-optic sensing for application in oil and gas wells.
- Margrave, G. F. (2000). New seismic modelling facilities in matlab. *CREWES Research Report*, 12.
- Mateeva, A., Lopez, J., Potters, H., Mestayer, J., Cox, B., Kiyashchenko, D., Wills, P., Grandi, S., Hornman, K., Kuvshinov, B., et al. (2014). Distributed acoustic sensing for reservoir monitoring with vertical seismic profiling. *Geophysical Prospecting*, 62(4):679–692.
- Tromp, J., Komatitsch, D., and Liu, Q. (2008). Spectral-element and adjoint methods in seismology. *Communications in Computational Physics*, 3(1):1–32.

Vermeer, G. J. (1990). *Seismic wavefield sampling*. Society of Exploration Geophysicists and Shell Research BV.

Wang, H. F., Zeng, X., Miller, D. E., Fratta, D., Feigl, K. L., Thurber, C. H., and Mellors, R. J. (2018). Ground motion response to an ml 4.3 earthquake using co-located distributed acoustic sensing and seismometer arrays. *Geophysical Journal International*, 213(3):2020–2036.

9 Appendix A: Validation tests

9.1 Testing Parameters

In order to construct a model that represents DAS-measurements, first validation tests with different parameters are done within SPEC-FEM to fully understand how it operates. Boundary conditions and initial conditions are checked and explained below. The first runs are done for an acoustic model in a homogeneous medium with only acoustic wave propagation with a source in the middle (source is an acoustic pressure pulse), and 161 receivers are located 1 m below the surface from $x=120$ m to $x=280$ m with 1 m spacing in between (see figure 57). The receivers are located 1m below the free surface, because for a DAS configuration burying the fibre one meter seems realistic for surface seismics applications. The medium is 400 m by 400 m and the V_p is 1850 m/s. First a few basic runs were done, with only changing the wave velocity or changing the density. Increasing the velocity gave a faster wave propagation as expected. Increasing or decreasing the density does not change the wave propagation in a homogeneous medium. The bottom, right and left side of the medium are absorbing boundary layers, which means that the waves will continue to propagate. The top side of the medium is not an absorbing boundary layer but acts as a free surface; important is that the pressure at this free surface is zero. The receivers or source can't be placed exactly at the free surface in a acoustic medium, since the pressure is zero there.

SPEC-FEM can produce different output data. For this thesis the interest is in pressure, displacement and velocity. In figures 58 and 59 snapshots of the previous described run can be seen for pressure and displacement. It can be seen that pressure in figure 58 shows an isotropic propagation. For the vertical displacement it can be seen in figure 59 that the wavefield has opposite polarity while propagating to the top of the medium in comparison with the bottom of the medium. This difference can be explained because pressure is a scalar which will act isotropic and displacement is a vector.

When the wave propagates through the medium it will reflect at the free surface, a reflection of the wave will then propagate back into the medium. Pressure is a scalar property and has the same value in each direction. Since pressure is zero at the free surface, pressure will change in polarity when it reflects at this surface. This change in polarity is visible in the snapshots in figure 60 and figure 61. It can be seen that polarity changes for pressure in figure 60 after reflection and the polarity stays the same for displacement (figure 61), as expected since pressure is zero at the free surface and displacement is not.

To go from displacement to velocity and to acceleration a separate function in MATLAB is written. The ASCII input files contain two columns; the first column is time and the second column is the amplitude of displacement. In the MATLAB function the velocity is calculated by taking the derivative of the second column of the ASCII files, through a do loop. For the acceleration the

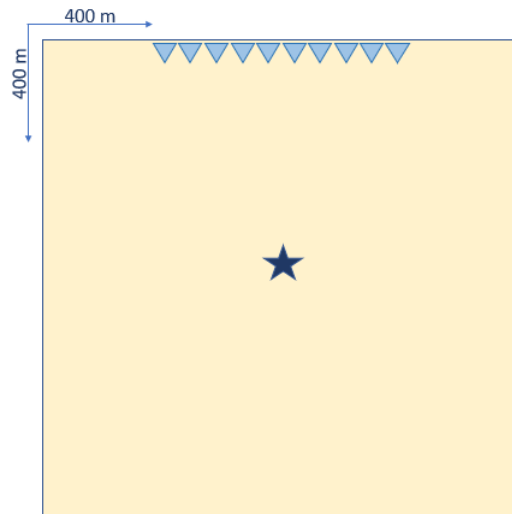


Figure 57: Configuration of the model for the first tests, model is 400 m by 400 m; receivers are located 1 m below the free surface and the source is located in the middle of the model

derivative is taken for the second time to calculate the acceleration, through a do loop again. For the validation tests of displacement will be used, since it's a simpler output.

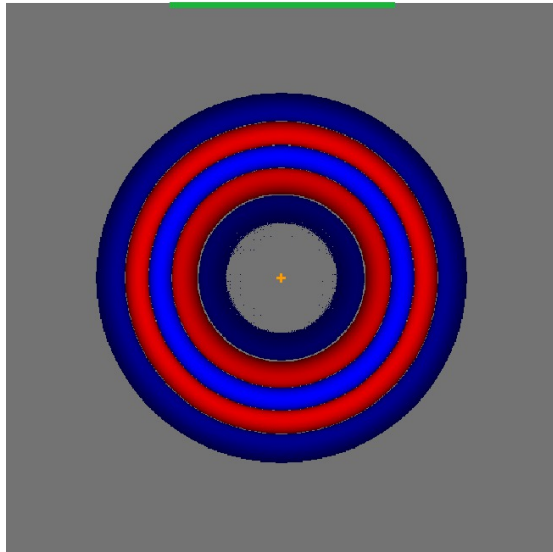


Figure 58: Snapshot at $t=0.008$ sec of wave propagation produced by SPEC-FEM, homogeneous acoustic medium, pressure

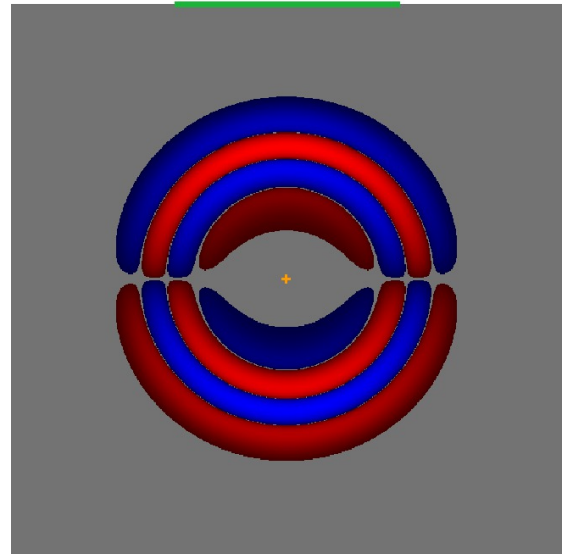


Figure 59: Snapshot at $t=0.008$ sec of wave propagation produced by SPEC-FEM, homogeneous acoustic medium, vertical component of displacement

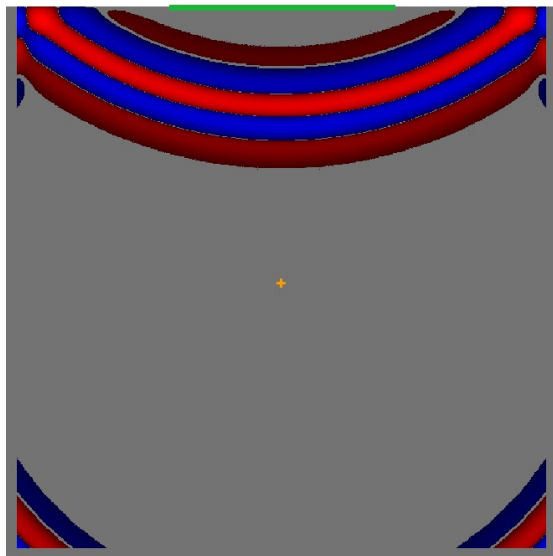


Figure 60: Snapshot at $t=0.0016$ sec of wave propagation produced by SPEC-FEM, homogeneous acoustic medium, pressure. Snapshot is after reflection at the surface.

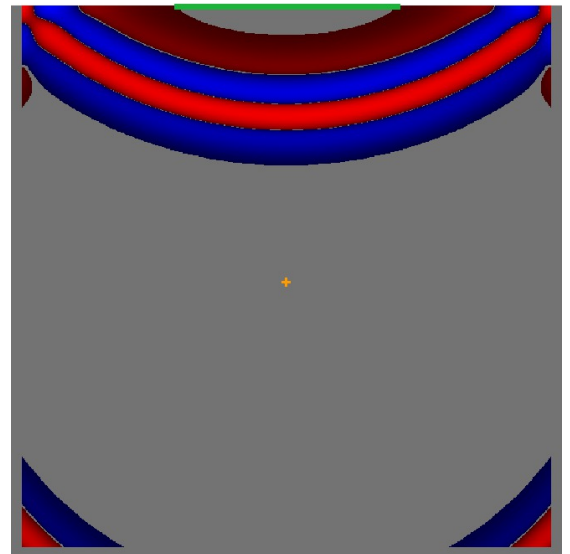


Figure 61: Snapshot at $t=0.0016$ sec of wave propagation produced by SPEC-FEM, homogeneous acoustic medium, vertical component of displacement. Snapshot is after reflection at the free surface.

9.2 Influence of free surface

To check the effect of the free surface for different burial depths of the receiver line, three scenarios are compared. In the three scenarios the receivers and source are located at the same height but the burial depth of the source and receivers are varied: the height of the free surface increases. In the first scenario the receivers are only 1 meter below the surface (which is the minimum, since the receivers can not be placed at the free surface), for the second scenario the receivers are placed 10 meters below the surface and for the third scenario the receivers are placed 100 m below the surface.

First, the wave propagation for pressure is constructed with SPEC-FEM. The output files of SPEC-FEM contain snapshots of the wave propagation. Furthermore, the amplitude of the pressure for each trace versus the time can be plotted. The (x,t) shot panels are plotted with the use of scripts in MATLAB. Below, the pressure is plotted for all the traces (figure 62) and for the three mentioned scenarios in one plot. To compare the difference between the scenarios there is a zoomed figure with just three traces (figure 63). From this plot, the following can be stated. The red line corresponds to the receiver 100 m below the surface and shows that the wave travels twice past the receiver line: before reflection and after reflection at the free surface, and it shows a polarity change relative to each other as expected. For the other two scenarios the pressure wave reflects at the free surface too, but is not separately visible. Because the travel time between the up going and reflected wave is shorter they interfere with each other. The pressure that is plotted is a result of interference between the up going wave and the reflected wave and a polarity change. For the blue line, where the free surface is 10 m above the receiver line, this results in the largest amplitude compared to the other two situations, so the interference increases the amplitude of wave propagation. For the black line, the scenario where the free surface is just 1 m above the receiver line, this results in a smaller amplitude than the other two scenarios. So a difference in amplitude between the three different scenarios are visible, which can be explained by the way the waves interfere with each other.

The three scenarios that were used for pressure were also tested for displacement, velocity and acceleration. The displacement for the z-component can be viewed in figure 64 for all traces and the three scenarios, and for only three traces and a zoom in to make a better comparison (figure 65). From the output files the same can be done for the x-component of displacement. Unlike for pressure the displacement doesn't have to be zero at the free surface, so polarity reversal doesn't apply here at the free surface. Which is true when you look at the displacement component where the receiver line is 100 meter below the surface. The propagating wave shows the same polarity as the reflected wave, but the amplitude is smaller at the reflected wave. For the other two scenarios where the receiver line is one and ten meter below the surface the up going wave interferes with the reflected wave, which results in interference and no polarity

change. In this plot the scenario where the free surface is one meter above the receiver line, shows the biggest amplitude. Due to the interference the amplitude increases. The same happens for the scenario where the receiver line is 10 meter below the free surface, but the amplitude increases less.

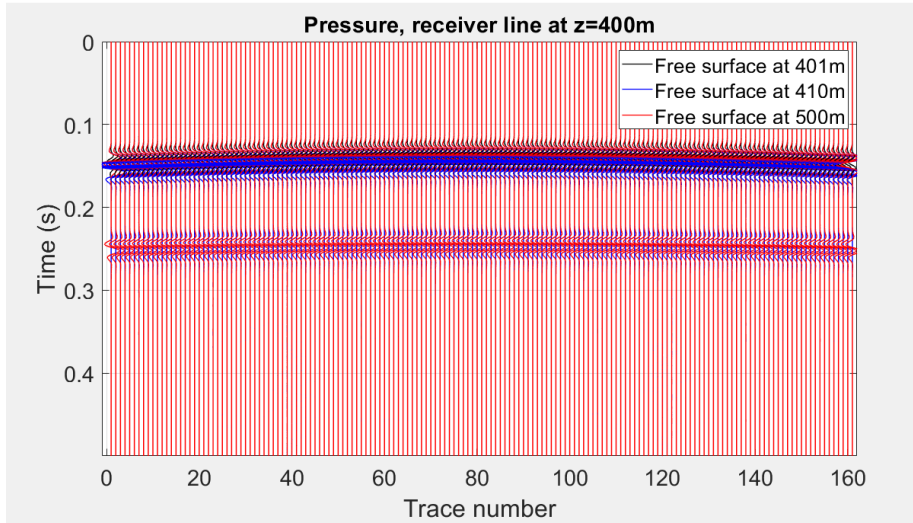


Figure 62: Panel of different burial depth of the receiver line for pressure and all traces are plotted: free surface at 401 m means receiver line 1 m below the free surface, receiver line at 410 m means receiver line 10 m below the free surface and free surface at 500 m means receiver line 100 m below the free surface.

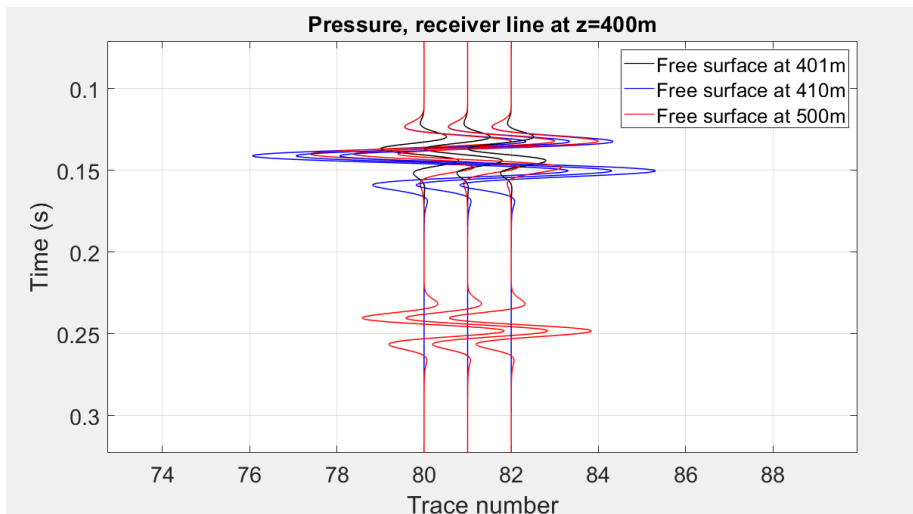


Figure 63: Panel of different burial depth of the receiver line for pressure and three traces are plotted: free surface at 401 m means receiver line 1 m below the free surface, receiver line at 410 m means receiver line 10 m below the free surface and free surface at 500 m means receiver line 100 m below the free surface.

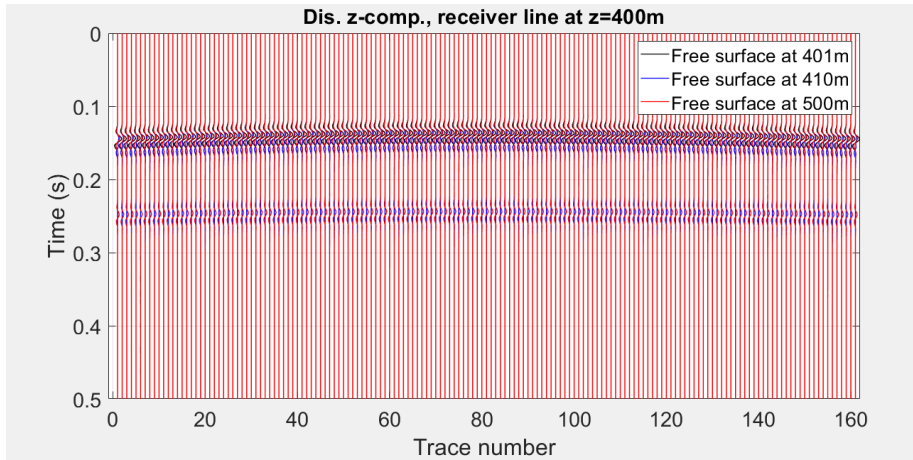


Figure 64: Panel of different burial depth of the receiver line for displacement and all traces are plotted: free surface at 401 m means receiver line 1 m below the free surface, receiver line at 410 m means receiver line 10 m below the free surface and free surface at 500 m means receiver line 100 m below the free surface.

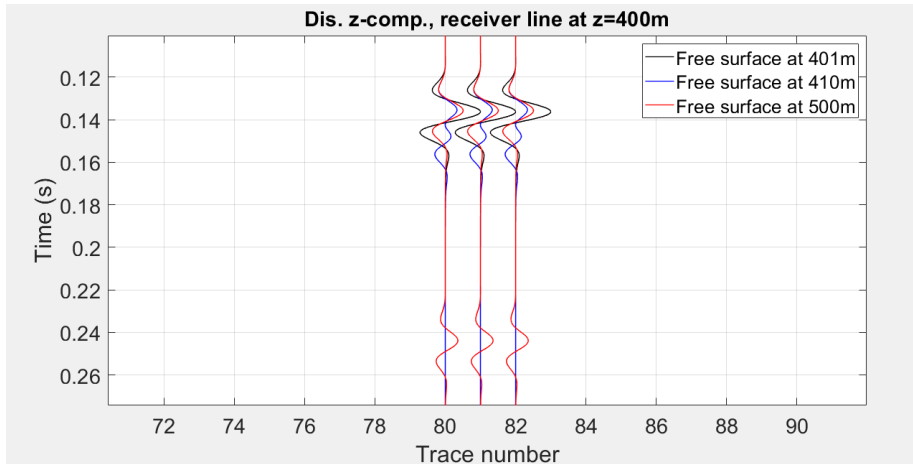


Figure 65: Panel of different burial depth of the receiver line for displacement and three traces are plotted: free surface at 401 m means receiver line 1 m below the free surface, receiver line at 410 m means receiver line 10 m below the free surface and free surface at 500 m means receiver line 100 m below the free surface.

9.3 From an acoustic medium to an elastic medium and testing different sources

After testing the free surface, elasticity has been brought into the model. To go from acoustic wave propagation to elastic wave propagation for the same model, which means that the model doesn't only contain a P-wave velocity (further referred to as V_p) but also contains an S-wave velocity (further referred to as V_s). There is first a run done for a source at a depth of 200 m and the receivers at a depth of 400 m, 1 m below the free surface (this model has still the configuration of figure 57). The V_p velocity is 1800 m/s and V_s is 1088 m/s. Something that needs to be kept in mind is that for the different media different sources are used. So the question arises to which end the different media are comparable. The sources available in SPECFEM are an acoustic pressure, elastic force and a moment tensor. For the acoustic medium only the acoustic pressure can be used as a source and for the elastic medium there can be chosen between an elastic force and moment tensor. In the following examples there is only made use of an isotropic tensor for the moment tensor, so we have only non zero values of the diagonals. The moment tensor seems to show a reversed polarity in the output of SPECFEM and therefore there has been chosen to use a negative moment tensor, stated in equation 28.

$$\text{Momenttensor} = \begin{bmatrix} -1 & 0 \\ 0 & -1 \end{bmatrix} \quad (28)$$

For an elastic model, pressure can be computed and for an acoustic model displacement can be computed with SPECFEM. It needs to be kept in mind that computing displacement in an acoustic model, is calculated from the pressure output and computing pressure in an elastic model, is calculated from displacement. Therefore from now on only displacement is computed and compared in the acoustic model and elastic model, knowing that for the acoustic model this is calculated from the pressure.

First the snapshots of the three different sources are shown; the geometry of the medium with the source in the middle and the receivers one meter below the free surface is the same for all three sources. Displayed is the displacement in the z-direction. The response of the acoustic model is displayed in figure 66, the elastic model with the moment tensor is shown in figure 67 and for the elastic model, the response of the elastic force (point force in the vertical direction) is shown in figure 68. Comparing these snapshots it can be seen that the acoustic pressure and the moment tensor source show the same pattern in propagation and thus can be compared to each other when comparing the acoustic medium with the elastic medium. On the other hand the elastic force shows a different propagation pattern than the other two forces, which can be explained by that its point source expresses a vertical force to the bottom of the medium, while the other two sources are both isotropic sources.

Besides the snapshots, shot panels are compared for both the models in figure 69 for all the traces, and in figure 70 for three traces and zoomed in. From the panels, it can be seen that the elastic force source response differs too much from the other two sources to make a fair comparison. Therefore in figure 71 only the acoustic pressure and moment tensor are compared to each other for the trace plot (offset versus time), and in figure 72 three traces are plotted and are zoomed in. From this last plot it can be stated that the acoustic pressure in an acoustic medium propagates comparable to an isotropic moment tensor in an elastic medium.

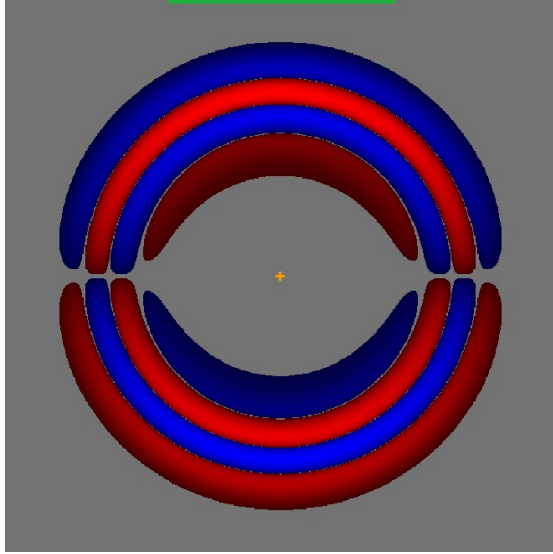


Figure 66: Snapshot at $t=1000$ msec for an acoustic medium, the source is located in the middle and produces an acoustic pressure pulse. Displacement in z -direction.

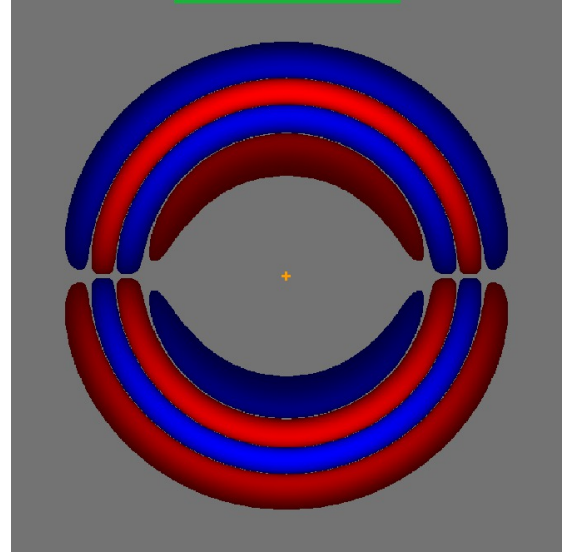


Figure 67: Snapshot at $t=1000$ msec for an elastic medium, the source is located in the middle and is an isotropic seismic moment tensor. Displacement in z -direction.

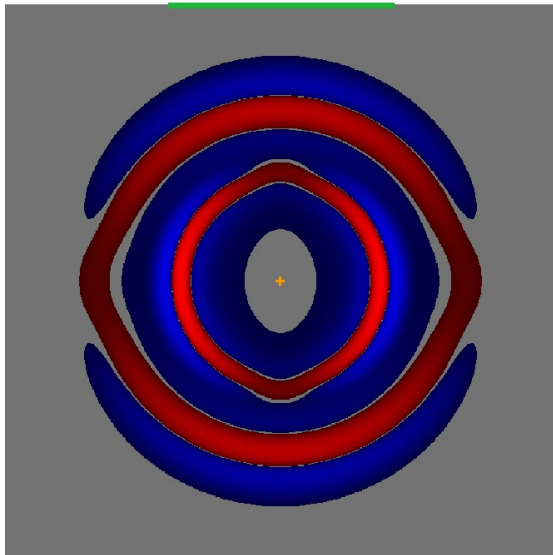


Figure 68: Snapshot at $t=1000$ msec for an elastic medium, the source is located in the middle and is an elastic force, vertically pointing downwards. Displacement in z -direction.

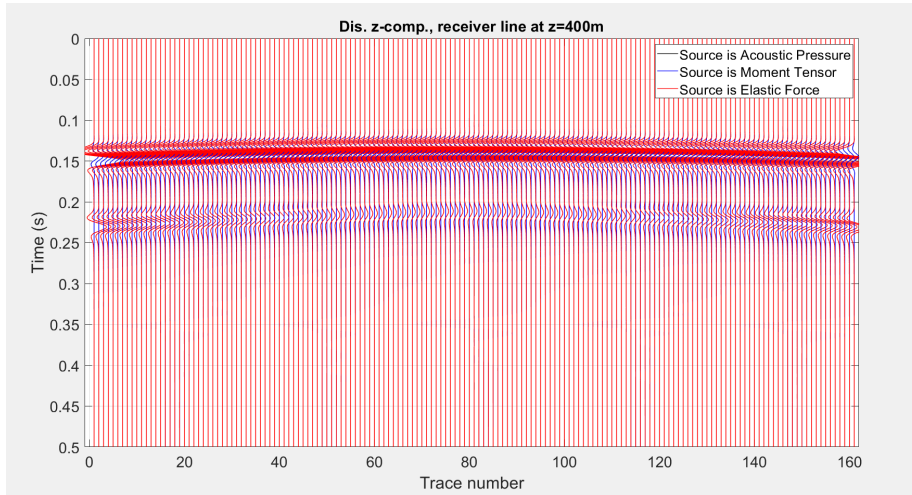


Figure 69: Shot panel response for the three sources, acoustic pressure, elastic force and moment tensor, all traces plotted. Receiver line is at 400 m, which means the receiver line is buried at 1 m depth.

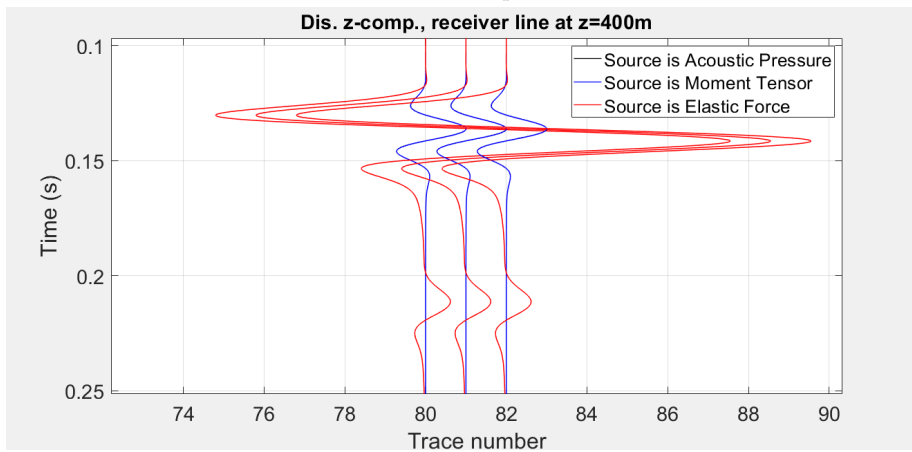


Figure 70: Detail of the shot panel response for the three sources, acoustic pressure, elastic force and moment tensor, three traces plotted. Receiver line is at 400 m, which means the receiver line is buried at 1 m depth.

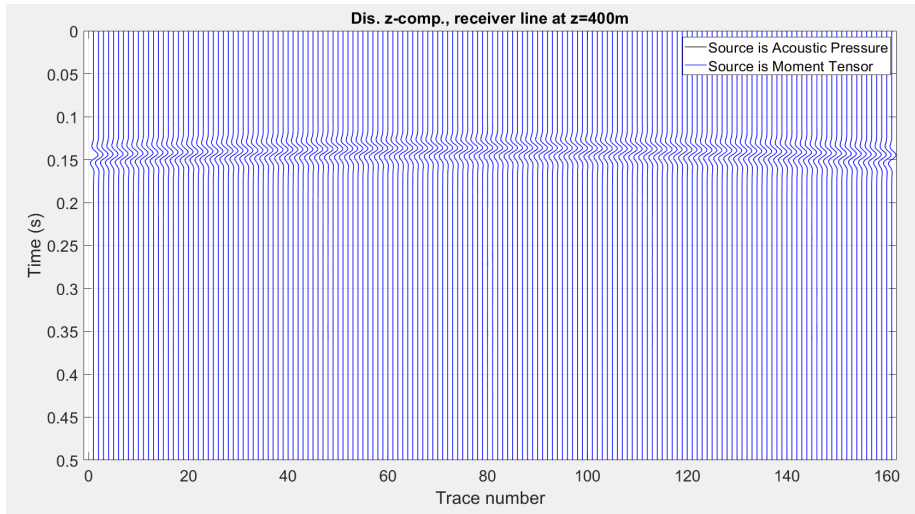


Figure 71: Shot panel response for two sources: acoustic pressure and the moment tensor, all traces plotted. Receiver line is at 400 m, which means the receiver line is buried at 1 m depth.

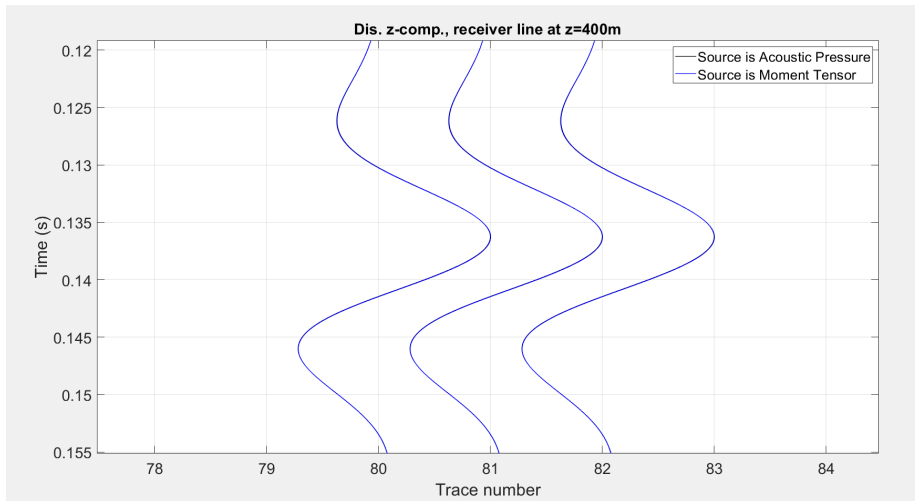


Figure 72: Detail of shot panel responses for two sources: acoustic pressure and the moment tensor, three traces plotted. Receiver line is at 400 m, which means the receiver line is buried at 1 m depth.

9.3.1 Elastic case: comparison of elastic force response and moment tensor response, source at 200 m depth.

Going from the acoustic model to the elastic model there are two types of sources that can be used in SPEC-FEM, an elastic force and a moment tensor. These two different sources are compared to each other, where the receivers lay 1 m below the free surface and the source is buried at 200 m, (the other parameters are kept the same for the two different sources). In figure 73, all traces are plotted and in figure 74 just three traces are plotted and is zoomed in. As was stated before it is hard to make a comparison between an elastic force which represents a vertical force directed downward in the medium, to the isotropic moment tensor. When looking at figure 74 the two sources both show an amplitude in different polarity and the elastic force shows a much larger amplitude compared to the moment tensor.

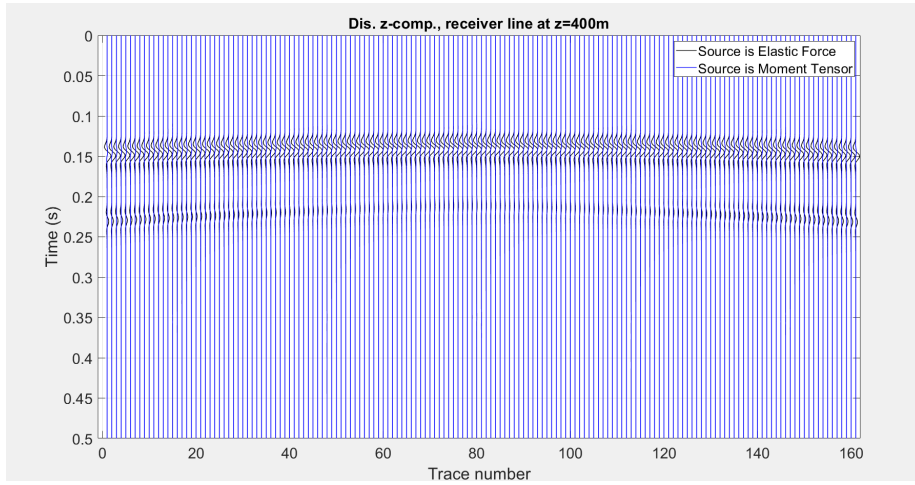


Figure 73: Shot panel response when source is located in the middle, for an elastic force and moment tensor and all traces. Receiver line is at 400 m, which means the receiver line is buried at 1 m depth.

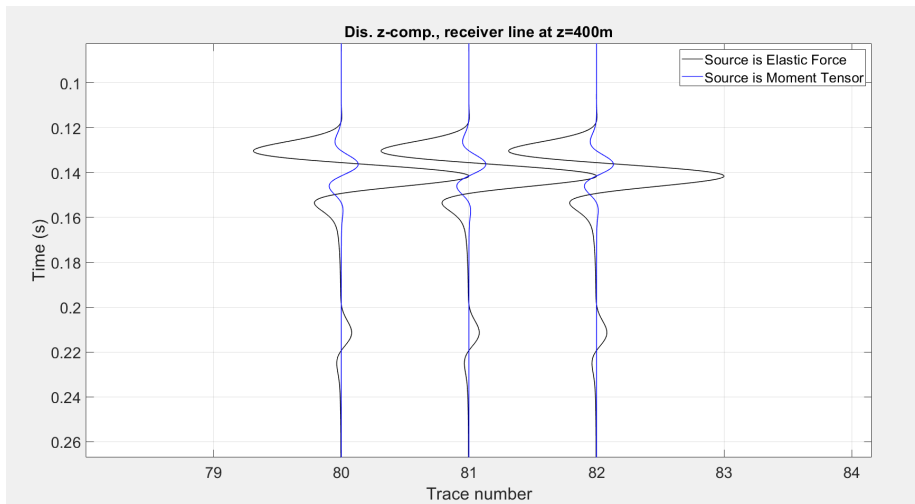


Figure 74: Detail of shot panel response when source is located in the middle, for an elastic force and moment tensor for three traces. Receiver line is at 400 m, which means the receiver line is buried at 1 m depth.

9.3.2 Elastic case: source at and 1 m below the surface

After testing the different sources, the source is now moved to the surface, since a source located at the surface is part of the surface seismic configuration, which will be used later on (figure 75). A different construction where the source is located at the free surface and the receivers are buried for one meter is tested next. First, the two different sources at the free surface for an elastic model are compared, the elastic force and the (negative) moment tensor. Since pressure can not be tested with a source at the free surface, because the pressure is zero there, only the displacement is compared. First, the snapshots are compared: in figure 76, a snapshot of the elastic force is shown and in figure 77 a snapshot of the negative moment tensor is shown. One question that arises is how the moment tensor at the surface is actually produced, but this could be constructed with the moment tensor just acting in one direction and set zero to the other directions (example of moment tensor is shown in equation 29). Comparing the two snapshots, they show a different propagation pattern for displacement and they show a different polarity. For the DAS configuration the source that will be used is an elastic force and therefore the modelling is continued with an elastic medium and an elastic force pointing vertically downwards.

$$Momenttensor = \begin{bmatrix} 0 & 0 \\ 0 & -1 \end{bmatrix} \quad (29)$$

For DAS data, the construction that is most convenient for the interpretation of the SPECFEM results, is the one where the source is located at 1 m below the surface acting as a vertical (or horizontal) elastic force as the receivers also lay 1 m below the surface. First, the comparison is being made for the wave propagation between the elastic force source at the surface and elastic force source 1 m below the surface. Looking at figure 78, for all the traces and figure 79 for four traces, it can be stated that a small difference arises between the source at the surface and the source one meter below the surface, but the elastic force source 1 m below the surface can easily be used for further testing. As these small differences are not affecting the interpretation of the shot panels.

Further tests were made for different receiver spacings. DAS has the advantage to produce signals corresponding with a very small receiver spacing and therefore high spatial resolution. Several tests are made with a receiver spacing of 10 m, 1 m and 0.5 m. All receiver spacings give the same wave propagation result and therefore a small receiver spacing can be implemented in SPECFEM.

All the panels and snapshots were shown for the vertical component of displacement, while geophone data in seismic surveys measure particle velocity in the subsurface. Displacement is the simplest form for wave propagation and therefore used for these validation tests, but now the step from displacement to (particle) velocity is made because for further models particle velocity is used. In figure 80 for all traces and in figure 81 for only five traces the panels are

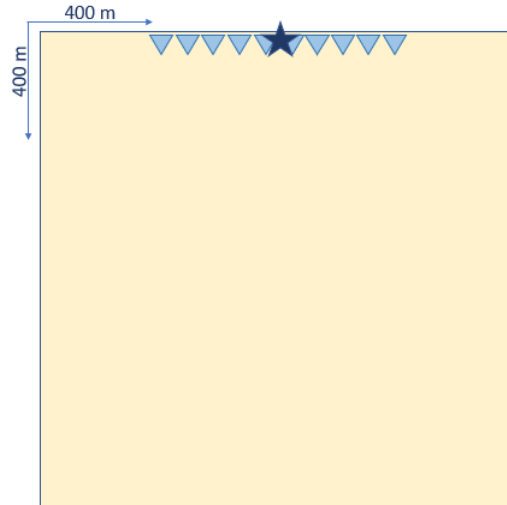


Figure 75: Configuration of the model where the source is moved to 1 m below the free surface. Other parameters stay the same

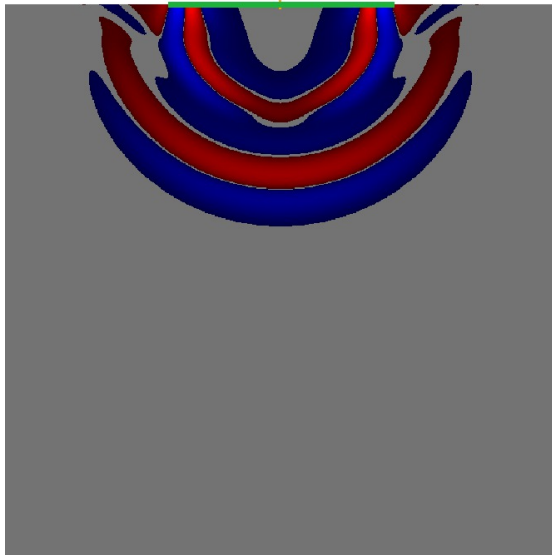


Figure 76: Snapshot in an elastic medium at $t=1000$ msec when the source is located at the surface, for an elastic force. Displacement in z -direction.

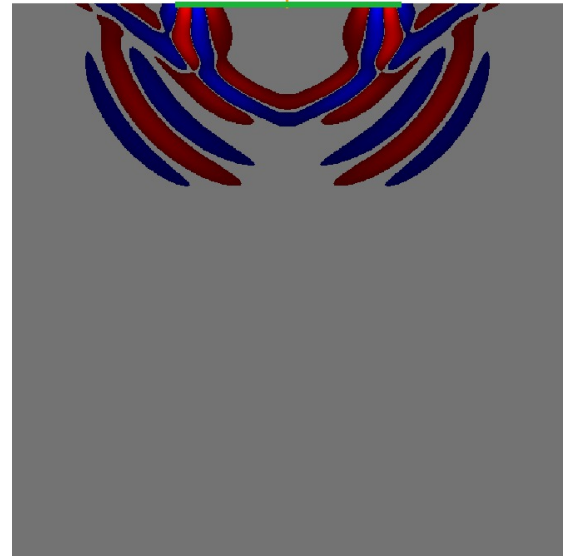


Figure 77: Snapshot in an elastic medium at $t=1000$ msec when the source is located at the surface, for an isotropic moment tensor. Displacement in z -direction.

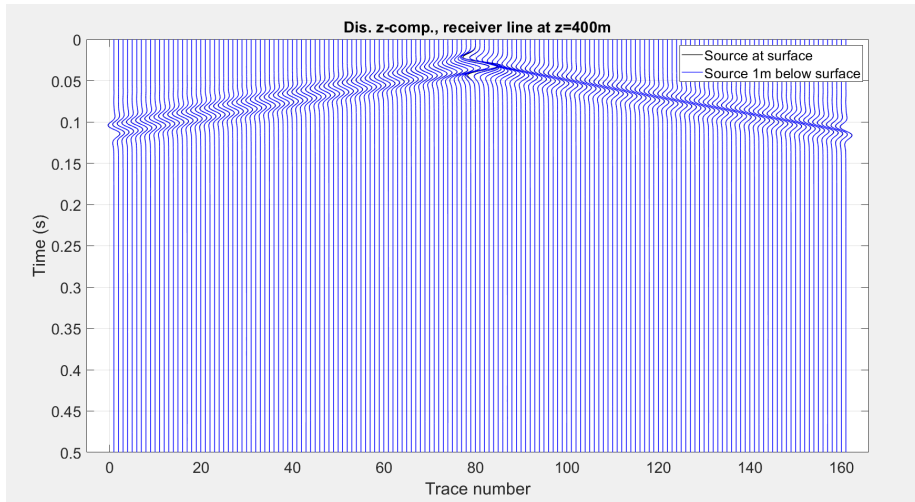


Figure 78: Shot panel response for the source located at the surface and the source located 1m below the surface (elastic force). Receiver line is at 400 m, which means the receiver line is buried at 1 m depth (Same depth as the source).

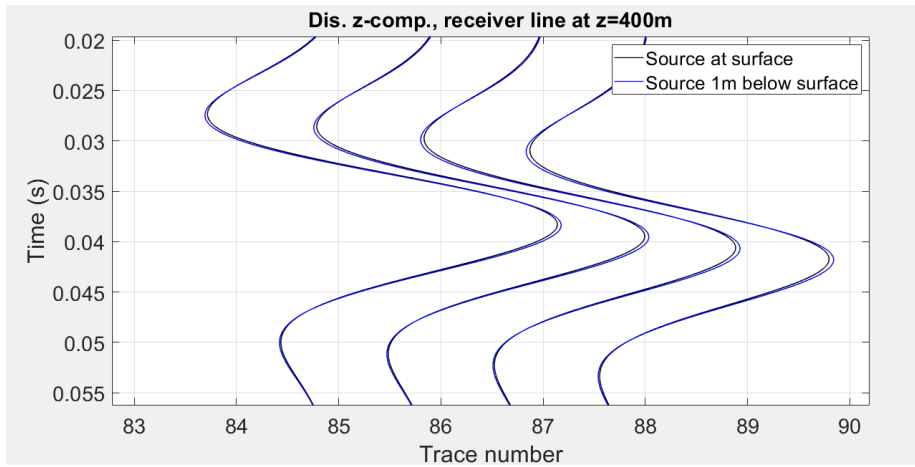


Figure 79: Detail of shot panel response for the source located at the surface and the source located 1m below the surface (elastic force) for four traces. Receiver line is at 400 m, which means the receiver line is buried at 1 m depth (Same depth as the source).

plotted to compare displacement to velocity. As already has been explained, velocity is obtained from displacement with a MATLAB script. The difference can be seen when looking at figure 81.

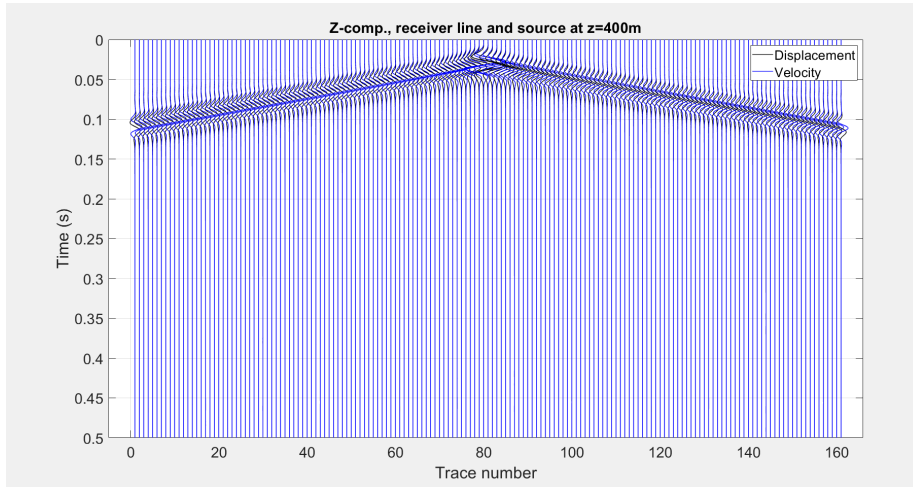


Figure 80: Shot panel response for the source located 1m below the surface for displacement and velocity for all traces. The direct wave clearly shows up with linear move-out. Receiver line is at 400 m, which means the receiver line is buried at 1 m depth (Same depth as the source).

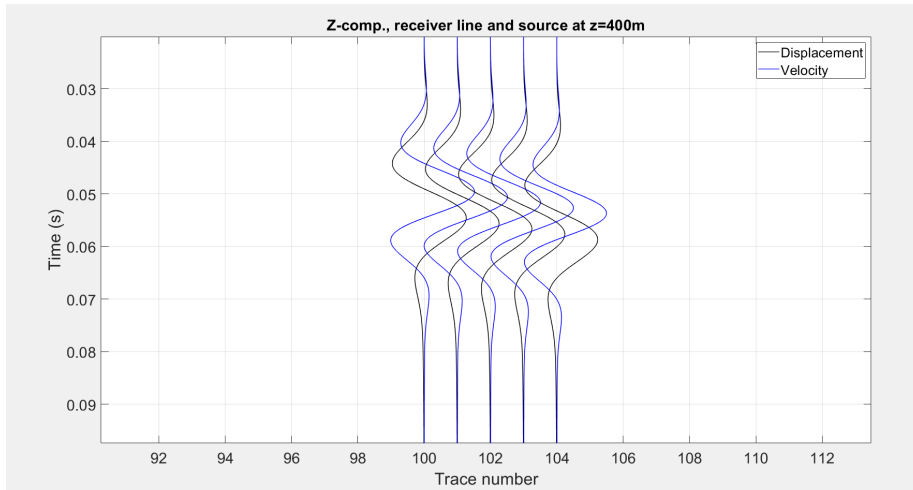


Figure 81: Detail of shot panel response for the source located 1 m below the surface for displacement and velocity for 5 traces: in the centre of the receiver spread (close to the surface). Receiver line is at 400 m, which means the receiver line is buried at 1 m depth (Same depth as the source).

9.4 Building the model

With all the validation tests in mind, the construction of the model can be started. The model which is used to continue, is 400 m by 400 m, the source is located 1 m below the free surface and in the middle of the medium and described by an elastic force. The receiver-line is also located 1 m below the free surface, consisting of 161 receivers and ranges from $x=120$ to $x=280$ with 1 m spacing in between. $V_p=1850$ m/s and $V_s=1088$ m/s. The geometry of the model can be viewed in figure 75.

For this model will first be looked at the arrival time of the waves. The arrival time of the direct waves can be determined with $t = \sqrt{x^2}/V_p$. In order to check if the arrival time fits with amplitude of the traces, the expected arrival time is plotted on top of the panels. Something that needs to be kept in mind is that the arrival time of the traces are shifted with $t=-0.03$. This shift of $t=-0.03$ happens in SPECFEM to prevent negative arrival times, so the arrival time in the shot panel needs to be adjusted for the same shift. As can be seen in figure 82 and figure 83, the expected arrival (calculated from $(t = \sqrt{x^2}/V_p)$ aligns quite well with the direct P-wave arrival in the panels. What also can be seen is, the slower but much stronger surface waves that are clearly visible in the panel.

Having this checked for the simple model, the next step will be to build in a reflector. This is done by changing the V_p and V_s halfway the medium, so at depth of 200 m. To make a clear transition the top layer will have a V_p of 2000 m/s and a V_s of 1176 m/s, the bottom layer will have a V_p of 4000 m/s and a V_s of 2353 m/s. So the velocity will be doubled and a clear transition between the top and bottom layer will arise. A V_p of 2000 m/s might not be a realistic value for a top layer beneath the free surface, but in a later model a weathering layer will be added too. This is done for the same model as earlier, from which the geometry can be viewed in figure 84. A snapshot of using this model can be viewed in figure 85. From this snapshot it can be seen that part of the wave reflect at the 200 m, due to the velocity increase. And part of the wave travels further down the model.

To create a larger offset-range in the model, the model is increased from $x=400$ m to $x=1000$ m. Because the source is still located in the middle, the x-axis runs from -500 to +500, the receiver spacing is still 1 m but the receiver array now extends all along the x-axis. The geometry of the model can be seen in figure 86 and a snapshot of the wave propagation can be seen in figure 87. With this offset-range, the reflection can be fully captured and is visible in the panels.

For this model panels of particle velocity in the x-direction and z-direction are plotted, again with the expected arrival times. The equations of the theoretical arrival times are stated in equation (6)- (11). The theoretical arrival times will be plotted for the direct P-wave, direct S-wave and the reflected P-wave and S-wave according to the equations that can be viewed below. V_{p1} and V_{s1} are the velocities of the top layer, z_1 is the length of the top layer and x the length

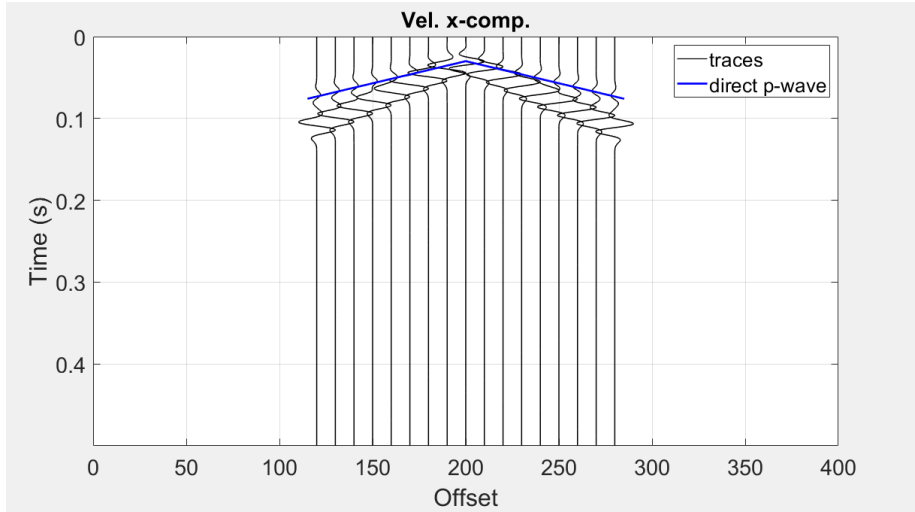


Figure 82: Plot of the computed particle velocity panel along the x-direction with source and receivers located 1 m below the surface in a homogeneous medium, as well as the theoretical arrival time. Plotted is every tenth trace, scaled to maximum of each trace and $sc=10$.

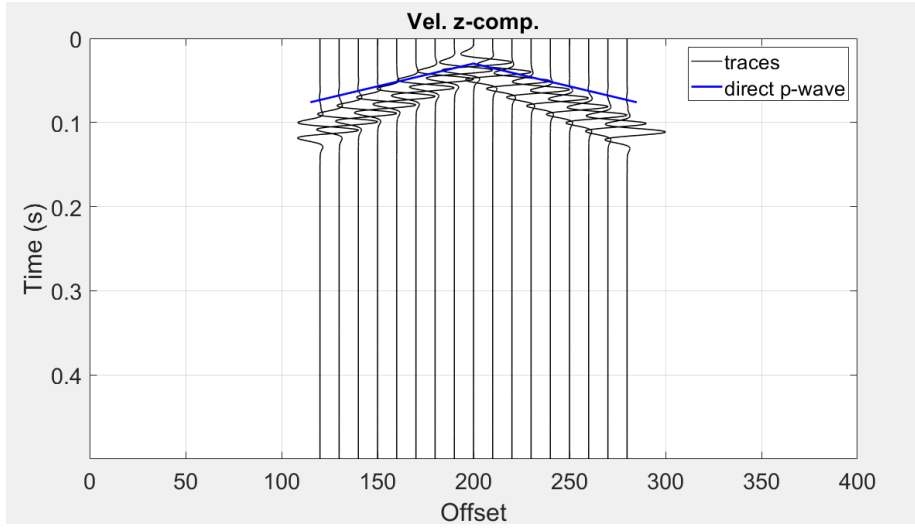


Figure 83: Plot of the computed particle velocity panel along the z-direction with source and receivers located 1 m below the surface in a homogeneous medium, as well as the theoretical arrival time. Plotted is every tenth trace, scaled to maximum of each trace and $sc=10$.

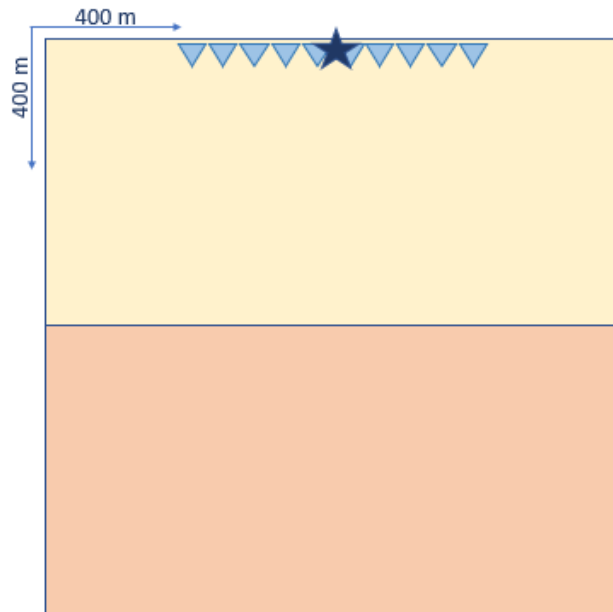


Figure 84: Geometry of the model in which a single reflector is built in. V_p is 2000 m/s and V_s is 1176 m/s in the top layer and V_p is 4000 m/s and V_s is 2353 m/s in the bottom layer.

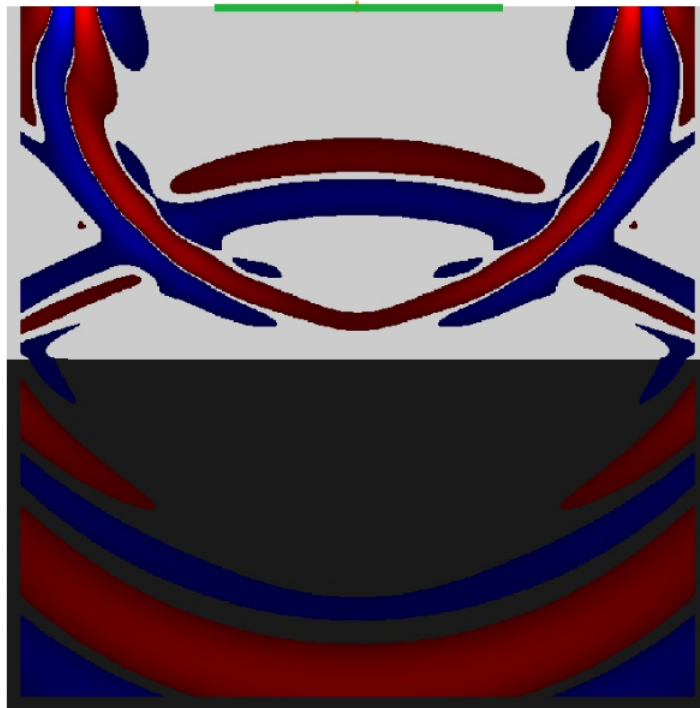


Figure 85: Snapshot at $t=3600$ msec of the model with the single reflector from figure 84.

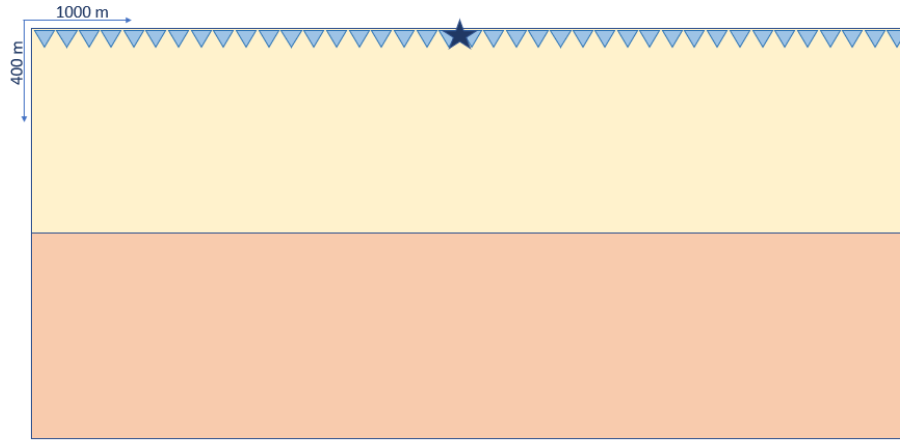


Figure 86: Geometry of the model where one reflector is built in at a depth of 200 m

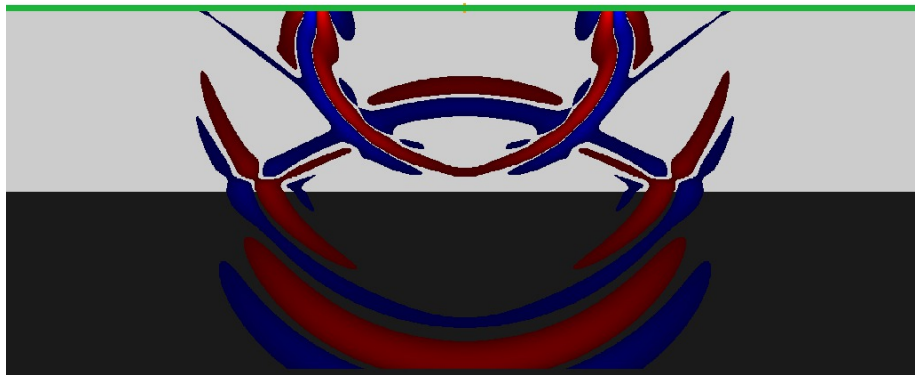


Figure 87: Snap shot at $t=3600$ msec, for the model with a reflection at 200 m and where the x-axis is extended from -500 m to 500 m.

of the x-axis. The panels for particle velocity in the x-direction and z-direction can be viewed in figure 88 and figure 89.

The next step in building the model is increasing offset of the model one more time from $x=-500,+500$ m to $x=-1000,+1000$ m. further a second shallower reflector will be built in at $x=20$ m with a V_p of 750 m/s and a V_s of 441 m/s in the shallowest layer, which will act as the weathering layer. At a later stage, the receiver spacing will be halved to 0.5 m between each receiver. In figure 90, the geometry of the model can be viewed and in figure 91 a snapshot using the model can be viewed with the two reflectors at 20 m and 200 m. Furthermore, the panels are shown in figure 92 for the particle velocity component in the x-direction and in figure 93 for the velocity component in the z-direction.

When expanding the model the time step and the amount of steps should be altered too. The SPECFEM manual dedicates a section about how to choose the correct time step (Komatitsch and Vilotte, 2018), which depends on the size of the model, the amount of elements which results in nodal spacing and the velocity used, in order to capture to propagating waves accordingly. For this model the offset is doubled, so in order to capture all the waves, the time step should be big enough. Therefore, the amount of time steps is doubled for offsets from $-1000,+1000$; the size of the time step stays the same. When the offset was increased from $x=400$ m to $x=-500,+500$ m the time step was halved and the amount of time steps was doubled, so the total time span stays the same.

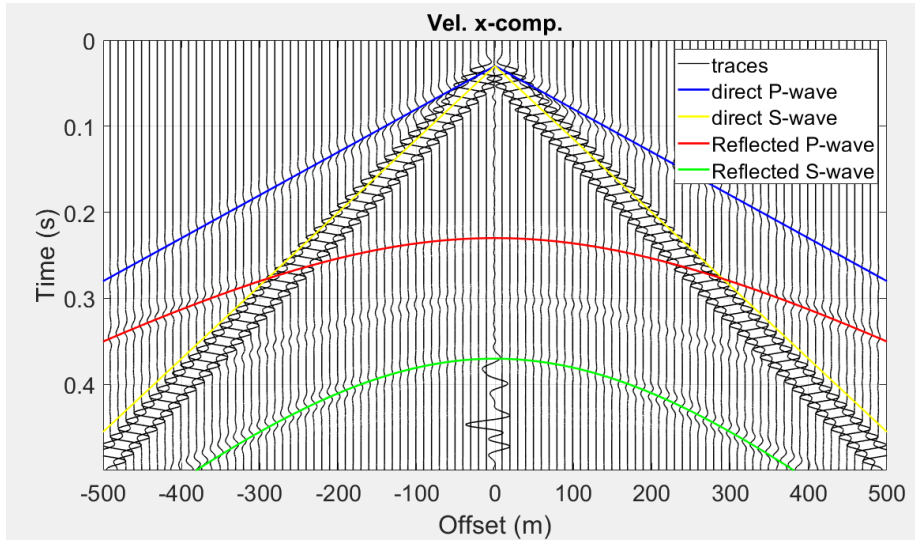


Figure 88: Panel for particle velocity in the x-direction, with one reflector the medium at $z=200$ m, two layer model. Traces are scaled to the maximum of each trace and every 10 traces one trace is plotted and $sc=20$. On top of the traces the expected arrival times are plotted for the direct P- wave and S-wave and reflected P-wave and S-wave.

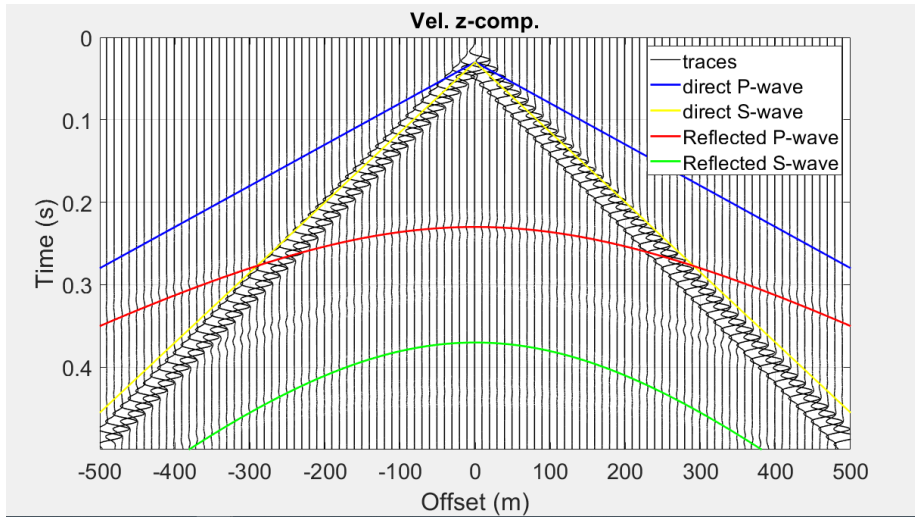


Figure 89: Panel for particle velocity in the z-direction, with one reflector the medium at $z=200$ m, two layer model. Traces are scaled to the maximum of each trace and every 10 traces one trace is plotted and $sc=20$. On top of the traces the expected arrival times are plotted for the direct P- wave and S-wave and reflected P-wave and S-wave.

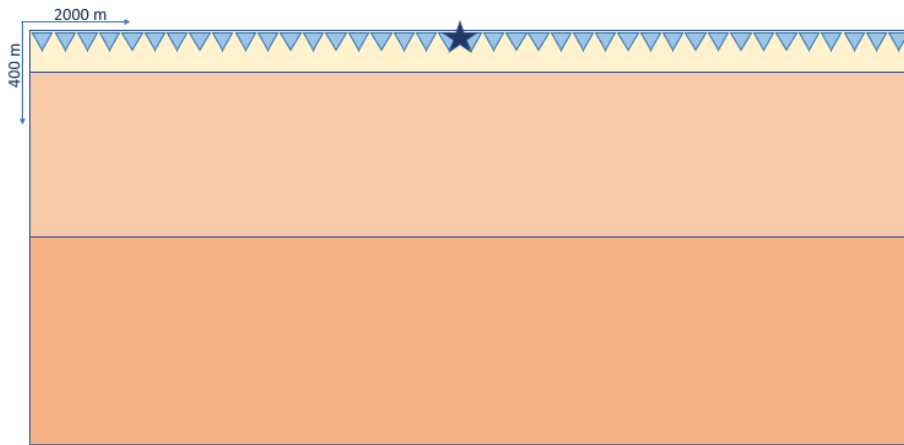


Figure 90: Geometry of the model in which a shallow reflector is built-in at a depth of 20 m; to create a weathering layer

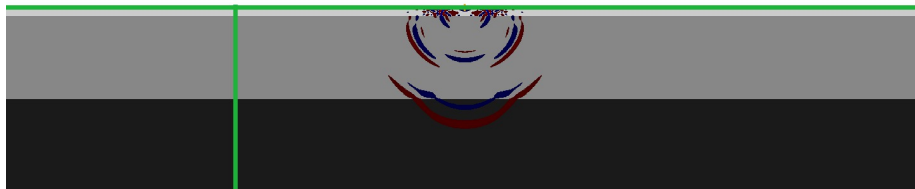


Figure 91: Snapshot of the model with two reflectors at $t=3200$ msec.

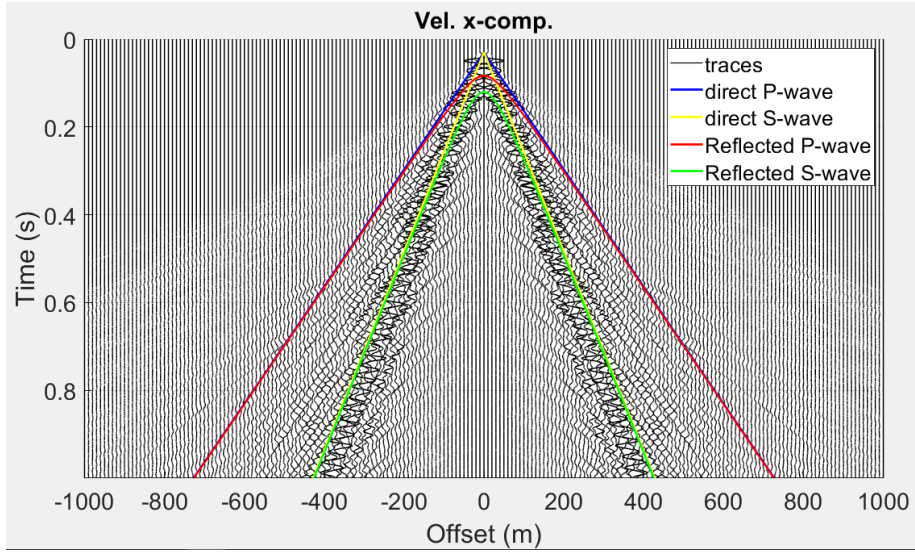


Figure 92: Plot of the panel for all traces for the particle velocity in the x-direction with a second reflector at $z=20$ m, three layer model. Plotted is one trace every 20 traces and $sc=50$ and panel scaling.

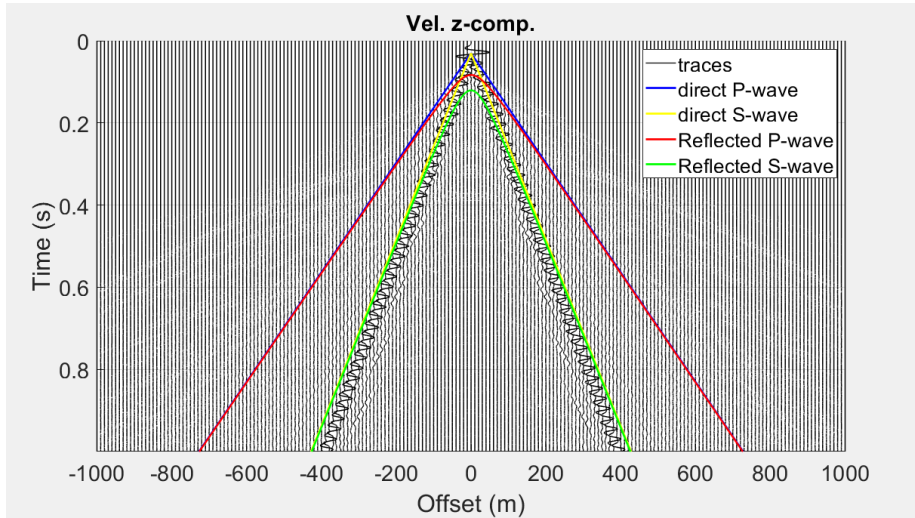


Figure 93: Plot of the panel for all traces for the velocity in the z-direction with a second reflector at $z=20$ m, three layer model. Plotted is one trace every 20 traces and $sc=50$ and panel scaling.

10 Appendix B: Explanation of the codes used.

In figure 94 is the workflow shown for the programs and scripts used in this thesis. Displayed is the input and output for each step including the programs and codes used. The script steps are numbered and explained more in detail here below, all the scripts can be found on the TNO server '\\tsn.tno.nl \Data \sv \sv-065072 \Geophysics \Stagair_Kari_Ann'. Some scripts are written separately for the two-layer model and three-layer model, but the scripts are taking the same steps.

(1) The runs in SPECFEM are done by filling in the input files, Par-file, source-file, station-file and the interfaces-file. By doing this the model is constructed and SPECFEM is simulating the wave propagation through this model. An example of the input files and output from SPECFEM can be found in 'Input-files_SPECFEM' at '\\tsn.tno.nl \Data \sv \sv-065072 \Geophysics \Stagair_Kari_Ann'.

(2) The output from SPECFEM can be plotted as shot panels in MATLAB. First are the .sem* files, which is the output from SPECFEM ordered for the x-direction and z-direction. With a different script the shot panels are then plotted for each trace through a do loop. Before the plotting a low pass filter is applied, at 80 Hz (everything above 80 Hz is filtered out). The name of the script is 'mergingdata_distance.m' and 'plottingdata_distance.m' and can be found at '\\tsn.tno.nl \Data \sv \sv-065072 \Geophysics \Stagair_Kari_Ann'.

(3) With the use of the MATLAB toolbox *segymat-1.6* the shot panels can be transferred to .sgy files. This is done with the following statement: *WriteSegy(filename_x,M1_disx,'dt',dt,'revision',1)*.

(4) With this step the slope filter is applied to the shot panels in Seismic Unix. An example script of filtering out the surface waves can be found in *testscript_seismicunix_slopefilter.sh* at '\\tsn.tno.nl \Data \sv \sv-065072 \Geophysics \Stagair_Kari_Ann'. First the .sgy files are transferred to .su files. In seismic unix the panels are plotted and filters are applied. After the filtering the .su files are transferred back again to the .sgy files, which is done by declaring the header, the number of samples and time steps.

(5) Two point ray tracing is from the MATLAB toolbox CREWES. For a given velocity model and declared parameters, the rays are traced for the given model. An example of the two-point ray tracing is named 'ray_tracing_test.m' and can be found at '\\tsn.tno.nl \Data \sv \sv-065072 \Geophysics \Stagair_Kari_Ann'.

(6) The ray tracing gives the horizontal slowness and arrival time of the rays as output. With these parameters the incidence angle θ is calculated, which is used to calculate the correction factor and reversed correction factor. Which can be viewed in the script named 'plot_filtered_velocity_phasepick.m', which is located at '\\tsn.tno.nl \Data \sv \sv-065072 \Geophysics \Stagair_Kari_Ann'.

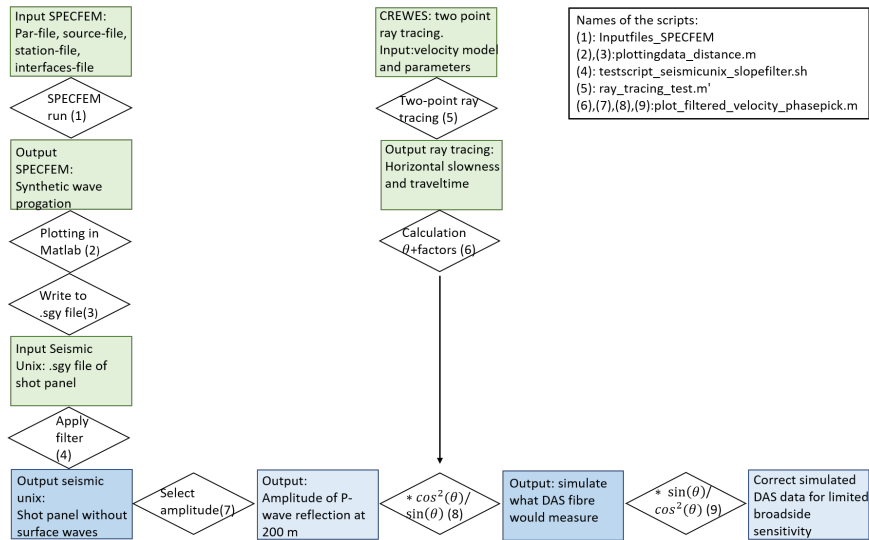


Figure 94: Workflow of the scripts used in this thesis. Indicated with input, scripts and output.

(7) The next step is selecting the peak amplitudes of the P-wave reflection. Here for an amplitude picker is designed, from which an example can be found in the scripts named 'plot_filtered_velocity_phasepick.m' or 'minimal_amplitude_test' located at '\\tsn.tno.nl \Data \sv \sv-065072 \Geophysics \Stagair_Kari_Ann'.

(8) Next the correction factor is applied to the peak amplitude, which can be found in 'plot_filtered_velocity_phasepick.m' located at '\\tsn.tno.nl \Data \sv \sv-065072 \Geophysics \Stagair_Kari_Ann'.

(9) Last step is to apply the reversed correction factor to the simulated DAS data, this is done in 'plot_filtered_velocity_phasepick.m' located at '\\tsn.tno.nl \Data \sv \sv-065072 \Geophysics \Stagair_Kari_Ann'.

11 Appendix C: Explanation $\cos^2(\theta)$

In this section is explained how the projection of strain tensor E on vector t is constructed. First the projection of the strain tensor on the vector t is computed, which gives a vector (equation 30). Then this vector is again projected on the vector t , which gives a scalar (equation 31).

$$\begin{bmatrix} e_{11} & e_{12} & e_{13} \\ e_{21} & e_{22} & e_{23} \\ e_{31} & e_{32} & e_{33} \end{bmatrix} \cdot \begin{bmatrix} t_1 \\ t_2 \\ t_3 \end{bmatrix} = \begin{bmatrix} e_{11}t_1 + e_{12}t_2 + e_{13}t_3 \\ e_{21}t_1 + e_{22}t_2 + e_{23}t_3 \\ e_{31}t_1 + e_{32}t_2 + e_{33}t_3 \end{bmatrix} \quad (30)$$

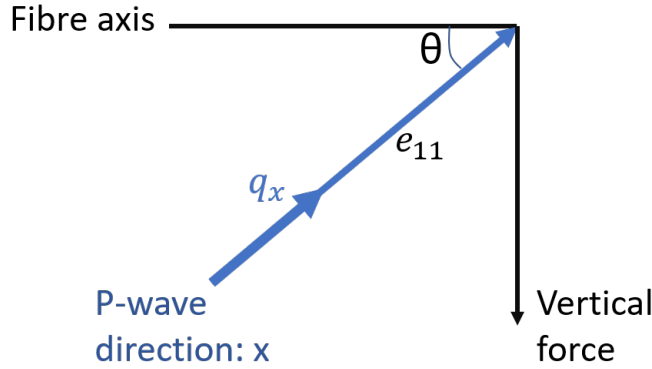


Figure 95: Schematic lay of for the parameterization of vector t , indicated is the fibre, vertical force, angle θ and q_x .

$$\begin{bmatrix} e_{11}t_1 + e_{12}t_2 + e_{13}t_3 \\ e_{21}t_1 + e_{22}t_2 + e_{23}t_3 \\ e_{31}t_1 + e_{32}t_2 + e_{33}t_3 \end{bmatrix} \cdot \begin{bmatrix} t_1 \\ t_2 \\ t_3 \end{bmatrix} \quad (31)$$

$$= e_{11}t_1^2 + 2e_{12}t_1t_2 + 2e_{13}t_1t_3 + e_{22}t_2^2 + 2e_{23}t_2t_3 + e_{33}t_3^2$$

Vector t is an unit vector, and depending on the orientation of the fibre and the angles used in the orientation, values for t can be determined. For the models in this thesis only the first component of the strain tensor e_{11} is non zero, the other 8 components are zero. Looking at the configuration of the model, displayed in figure 95. The unit vector t is given in equation 32.

For a straight fibre the angle between the force acting vertically downward and the fibre is 90 degrees. e_{11} is projection of strain tensor E (first tensor element) along the fibre axis. This projection is shown in equation 32, which gives the result of equation 33 and shows where the $\cos^2(\theta)$ factor comes from.

Earlier in the thesis in figure 4 is shown how $\cos^2(\theta)$ is translated to $\cos^2(\theta)/\sin(\theta)$ for a surface seismics configuration. Because for this thesis the interest is

in the vertical component of the P-waves. Therefore the correction factor $\cos^2(\theta)/\sin(\theta)$ is computed to simulate what the DAS fibre would measure and then the reversed correction factor $\sin(\theta)/\cos^2(\theta)$ is used to correct for the broadside waves, and thus translate the horizontal component of the DAS amplitude to the vertical component of the geophone.

$$e_{11} = \begin{bmatrix} e_{11} & e_{12} & e_{13} \\ e_{21} & e_{22} & e_{23} \\ e_{31} & e_{32} & e_{33} \end{bmatrix} \begin{bmatrix} \cos(\theta) \\ \sin(\theta) \\ 0 \end{bmatrix} \quad (32)$$

$$E \cdot q = e_{11}q_1^2 = \cos^2(\theta) \quad (33)$$